NUMERICAL SIMULATION AND MODELING OF A TURBOCHARGER COMPRESSOR AND TURBINE TO IMPROVE AERODYNAMICS AND ACOUSTICS PERFORMANCE

By

Mekuannint M. Messele

A DISSERTATION

Submitted to
Michigan State University
in partial fulfillment of the requirements
for the degree of

Mechanical Engineering – Doctor of Philosophy

2021

ABSTRACT

NUMERICAL SIMULATION AND MODELING OF A TURBOCHARGER COMPRESSOR AND TURBINE TO IMPROVE AERODYNAMICS AND ACOUSTICS PERFORMANCE

By

Mekuannint M. Messele

Downsizing modern automotive engines poses a challenge to turbocharger designs. Turbocharger compressors are required to provide a wide operating range with high-efficiency levels. The compressors are equipped with either passive or active casing treatments (ACTs) to achieve this goal. On the turbine side, the ever-increasing EGR flow into the engine demands an efficient scroll design that addresses both the performance and packaging limits.

The present study conducts numerical aerodynamic and acoustic performance investigation of a turbocharger compressor equipped with a dual-slot active casing treatment (ACT) to widen the compressor's low and high flow rate operating limits independently. The first slot (surge-slot), positioned between the leading edge of the main and splitter blades, improves the surge margin of the compressor. Similar to the widely applied self-recirculating casing treatment, the surge slot removes stagnant fluid from the boundary-layer region of the inducer and delivers it to the impeller inlet when the compressor operates near the surge limit. The second slot (choke-slot), positioned downstream of the aerodynamic throat, increases the choke margin of the compressor. A new combination of loss models is proposed to predict the compressor performance, providing satisfactory results. A novel methodology is developed to estimate the full compressor map from CFD results by incorporating Greitzer's surge model. The compressor performance analysis revealed that the choke-slot closed configuration resulted in an isentropic efficiency penalty at higher compressor speeds. The efficiency penalty is addressed by optimizing the choke slot thickness to reduce the mass flow recirculating in the channel.

On the other hand, the casing treatment provides an additional path for the unsteady compressor flow, increasing the noise level of the compressor. In this work, acoustic analogies are used to study the noise generated by different compressor casing treatment configurations. The transient aeroacoustic simulations are completed for both a choke-slot closed design near surge and a choke-slot open design near the maximum efficiency point. The simulation results revealed that the broadband and blade passing frequency (BPF) noise levels in the inlet and exit pipes decreased as the probe points moved away from the impeller.

Further, the double inlet turbine performance is assessed numerically at even and uneven turbine inlet flows for three cases representing different engine operating conditions ranging from low load to full load. The CFD setup in this study is validated by using nine experimental data points with equal admissions at the two volute inlets. A significant amount of performance drop is observed when the turbine operates at uneven turbine inlet flow cases. The performance drop is more pronounced when the turbine operating point moves from low to high loads. Additionally,an energy audit of the turbine assembly is completed by estimating the local entropy production rate at eleven sub-regions. In all flow cases, the tip region losses dominate the impeller losses at even and uneven flows. The volute flow is affected sharply by the mass flow imbalance across the turbine inlets, most notably at high engine loads.

In the last section of this work, the impact of volute design geometric parameters on the aerodynamic performance of the turbine with nozzle blades is explored by using a three-dimensional computational fluid dynamics method. The volute tongue angle, tongue clearance, and volute shape are assessed in detail to determine how they impact the turbine's isentropic efficiency and the pressure loss coefficient of the volute. The numerical results show that the optimal tongue angle is approximately 15° for single-scroll volutes. The study results also indicate that higher tongue clearance improves turbine performance as it enhances flow development. Finally, symmetrical cross-sectional shapes boosted the turbine's aerodynamic performance in single-scroll turbines by uniformly distributing the volute exit flow from the hub to the shroud.

ACKNOWLEDGEMENTS

First and foremost, I want to express my sincere gratitude to my supervisor, Dr. Abraham Engeda, for his invaluable advice, continuous support, and patience during my Ph.D. study. I would also like to thank Dr. Wei Liao, Dr. Norbert Mueller, and Dr. Neil Wright for agreeing to participate in my guidance committee and for their helpful suggestions and comments to improve this work.

I want to thank my internship supervisors Leon Hu and Eric Kurtz at Ford Motor Company research and innovation center, for the support and opportunities I was given to further my research.

I am thankful for the support and engaging conversations from the turbomachinery lab group, including Jinbo Chen, Ahmed Helmy, Javad Hosseinpour, Raul Quispe-Abad, Tasha Williams, and Casey Palanca.

Last but not least, I want to thank my parents, my sister Yemisrach Mesfin, Dr. Solomon Getahu and his family, Saliem Haile, Shiferaw Damte, Hiruy Dagnew, and other friends for always being there for me. I could not have completed this dissertation without their continuous encouragement and support.

TABLE OF CONTENTS

LIST OF TABLES

LIST OF FIGURES

CHAPTER 1

INTRODUCTION

New tight exhaust gas emission standards [1, 2] has increased the need to downsize an engine. Downsizing has additional advantages in minimizing the friction between the cylinder and pistons improving the fuel mileage MPG (miles per gallon) of the engine [3]. Engine downsizing can be achieved by decreasing the swept volume of the engine thereby, increasing the density of the air intake to the engine keeping maximum power from the engine . Out of many vehicle air boosting system options, the two extensively used devices are belt driven superchargers and turbochargers as they provide a reasonably efficient and inexpensive solution [1].

Superchargers are engine-driven air pumps that provide a compressed air above atmospheric pressure in doing so they improve the volumetric efficiency and air-fuel mixture of the engine. Since the engine drives superchargers, the power gain from the use of them is counterbalanced by a power used to drive them. On the other hand, turbochargers use the otherwise wasted exhaust gas energy from the engine to drive the turbine which is connected to the centrifugal compressor by a co-axial shaft.

Turbochargers are vital components of modern engines. They typically can be found in trucks, buses, ships, rails, and industrial power sets. Coupled with inter-coolers they function similar to the superchargers to increase air density with additional improvement on the resistance to detonation. Figure 1.1 shows a typical diesel engine system with a turbocharger.

The turbocharger compressor driven by the turbine helps raise the airflow pressure before the flow is admitted to the engine. The compressed air that leaves the compressor volute is guided to the engine through exit pipes. Installation of an intercooler before the engine inlet helps further increase the air density, assisting in the faster burn rate of the fuel in the engine combustion chambers.

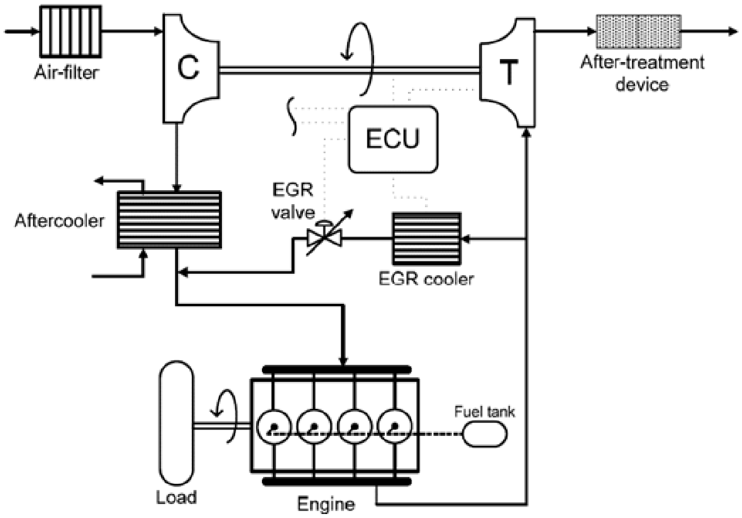

Figure 1.1: Schematic arrangement of the current state of the art turbocharged diesel engine [4]

1.1 The Turbocharger Compressor

Centrifugal compressors in turbochargers deliver pressured air to internal combustion engine cylinders. A pressure differential between the inlet pipe and the compressor inducer causes fluid to flow axially into the compressor impeller. Compressor rotors, driven by turbocharger turbines, exert a force on the flow and increase its kinetic energy and pressure. The medium flow path is changed from axial to radial direction when it passes through the impeller channels. Euler's turbomachinery equation governs the transfer of energy between the rotor and the flow medium. A single stage centrifugal compressor configuration is displayed in Figure 1.2.

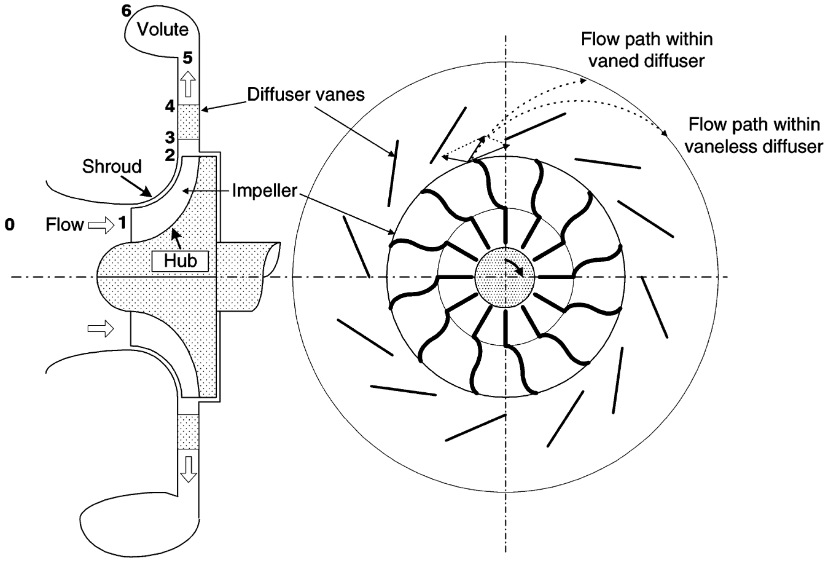

Figure 1.2: Single stage centrifugal compressor with vaned diffuser [5]

Approximately 40% of the total input work will be carried out by the flow leaving the impeller outlet into the diffuser inlet [6]. A further pressure boost occurs as the flow travels through the vanless or vaned diffusers by converting some of its' kinetic energy. Finally, the volute collects the flow from the diffuser outlet and guides it into the engine cylinder through exit ducts. The volute also converts some of the kinetic energy of the flow into static pressure.

The isentropic efficiency and pressure ratio values evaluate the compressor performance as the flow medium passes between the compressor inlet and exit. The isentropic efficiency is calculated by dividing the adiabatic compression work by the amount of work required to attain a given pressure ratio. Figure 1.3 shows the h-s diagram of a centrifugal compressor stage with inlet, impeller, diffuser, and volute components marked.

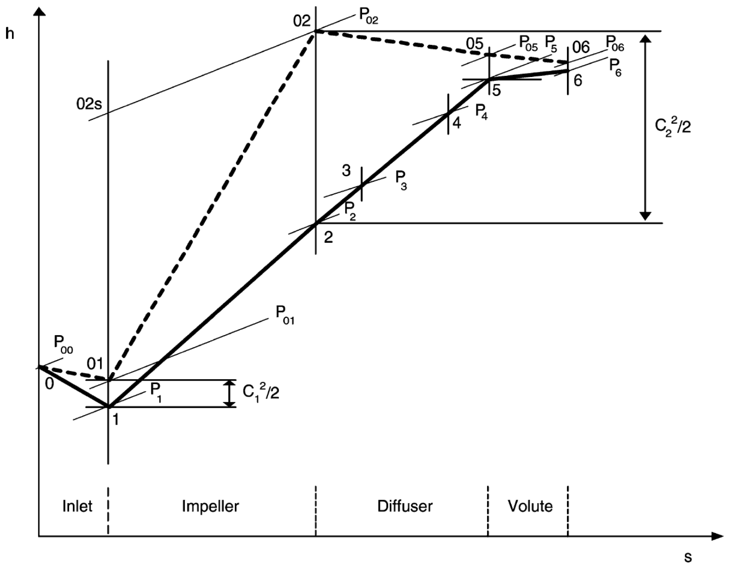

Figure 1.3: An h-s diagram for Single stage centrifugal compressor with vaned diffuser [5]

There are two types of losses in centrifugal compressors: internal losses and external losses. The internal losses refer to all losses that occur in the compressor's internal passage from the compressor inlet to the outlet. These losses include incidence, blade loading, skin friction, clearance, mixing, vanless/vaned diffuser losses. External losses (parasitic losses) account for disk friction, recirculation, and leakage losses. The various losses are estimated using several empirical correlations, as summarized in Aungier [7] and Oh et al. [8]. The compressor stage total-to-total pressure ratio can be calculated as:

$$\Pi = \left[\left(\frac{\Delta h_{Euler} - \sum \Delta h_{int}}{C_p T_{01}} \right) + 1 \right]^{\frac{\gamma}{\gamma - 1}} \tag{1.1}$$

where Δh_{Euler} is the change in enthalpy governed by the Euler equation and $\sum \Delta h_{int}$ represents the summation of all internal losses. The total isentropic efficiency of the compressor stage is calculated considering both the external and internal losses as:

$$\eta = \frac{\Delta h_{Euler} - \sum \Delta h_{int}}{\Delta h_{Euler} + \sum \Delta h_{ext}} \tag{1.2}$$

where $\sum \Delta h_{ext}$ represents the summation of all external losses.

1.1.1 Surge and Choke Limits

The operational range of a turbocharger compressor is bounded by the surge and choke limits. The surge limit occurs due to an increased incidence angle of the flow at reduced mass flow rates causing a partial or total flow separation. The flow separation from the blades induces a stalled region in the impeller flow channel blocking the portion of the flow cross-section area.

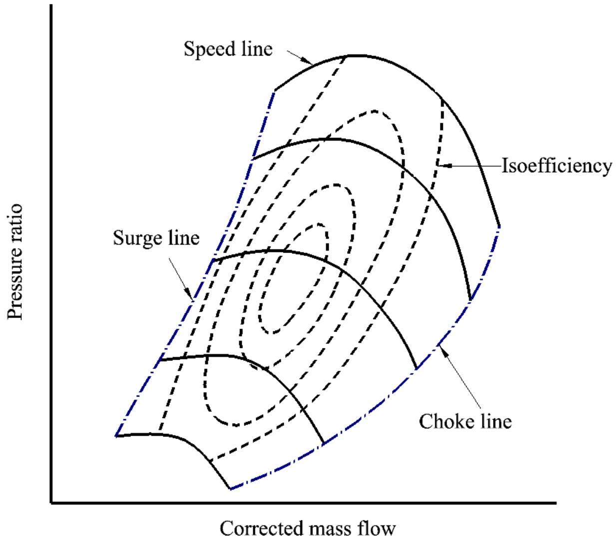

Figure 1.4: Typical Compressor performance map

When a stall occurs in one channel, it passes to the next channel creating unsteady mass flow fluctuations known as rotating stall. Rotating stall increases the vibration and noise level of the flow and may lead to stage instability. When a compressor operates at a constant speed with further reduction of mass flow rate, several components of the compressor stall. At this point, the stable operation of the compressor is not possible because of an active flow reversal. This phenomenon is known as stage stall. When the stage stall grows into a periodic and self-excited mode, a system instability known as the surge is induced. The flow in compressor operating in surge oscillates between positive and negative mass flow rate values leading to a complete breakdown of the compressor operation. The blades in surge are exposed to severe periodic forces which could damage the impeller blades and the whole compressor installation if immediate corrective actions are not taken. Surge limit from experimental investigation or compressor model is placed on a

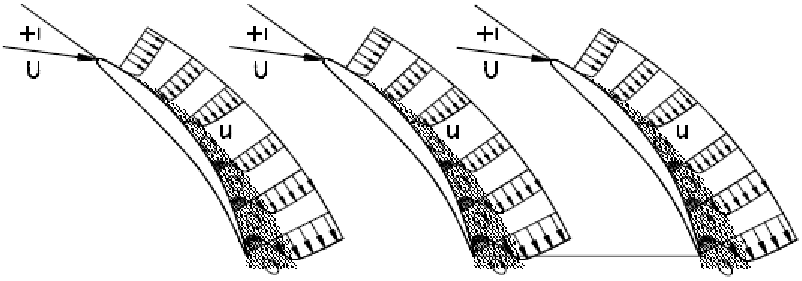

Figure 1.5: Boundary Layer Separation, the inception of stall cells [9]

compressor map by the compressor designer to avoid the compressor operate in a surge.

Up to now, there are no standardized criteria to define the surge point of a compressor at a specified speed line. Different authors have proposed different criteria to restrict the surge point on a characteristics curve. Fisher [10], proposed a criterion that limits surge point up to the positive slope of the characteristics the compressor so that instabilities can be avoided. Based on his experience of testing of a wide range of compressors, Fisher proposed the first sign of instability in the system corresponds to a peak-to-peak fluctuation in the compressor inlet static pressure of 8% of the mean inlet pressure [10].

The existence of surge can also be established from a local slope of the total-to-static pressure ratio vs. mass flow rate compressor diagram at constant speed operation [11]. At mid to higher flow rates, the slope of the diagram is negative ($dPR/d\dot{m} < 0$) with no instability observed in the compressor operation. At lower flow rates the compressor operation becomes unstable, and the slope becomes positive. The operating point where the slope is zero ($dPR/d\dot{m} = 0$) differentiates the stable and unstable operation regions of the compressor map [12].

When the flow velocity at some cross-section of the centrifugal compressor reaches to the speed of sound, choking occurs. At choke point, the flow attains sonic speed, and a further increase of the mass flow rate is not achievable for a given rotational speed of the impeller. Choking occurs at the narrowest area of the compressor, that is at the throat of the impeller inducer or the entry to a vaneless diffuser or the throat of a vaned diffuser [12]. The choke point for a given speed line is defined at 60% efficiency, and the accurate choke flow is a little to the right of this flow [10].

Choke line represents the locus of choke points at different compressor operating speeds.

Throughout the years, several techniques are developed by different researches to widen a centrifugal compressor map width without significant efficiency and pressure ratio penalties. Variable inlet guide vane [13, 14, 15], variable vaned diffuser [16, 17], and ported shroud [10, 18] are some of the commonly used techniques. While variable compressor geometry options can enhance the compressor map width efficiently, they have a drawback of cost and durability due to the elaborate design of the system. Variable inlet guide vanes (VIGV) are also suspect to reduced efficiency values at lower and higher mass flow rates because of increased throttling losses.

1.1.2 Shroud Casing Treatment

Passive ported shroud (PS) which is also termed as Map Width Enhancement (MWE) slot is the most extensively used, effective and inexpensive casing treatment in turbochargers. PS introduced by Fisher [10], has a cavity that provides a secondary fluid flow path from the inlet pipe to the compressor inlet in addition to the main through flow. This cavity connects the compressor inlet pipe to shroud area near to the leading edge of the compressor by a circumferential slot with supporting ribs used to keep the cavity intact. The ported shroud extends the compressor surge and choke limits by balancing pressure between the inducer and the compressor shroud near the inlet. This ported shroud is open in all on and off design operating conditions which results in efficiency and pressure ratios losses. At surge operation, a negative pressure gradient between the inducer and the slot forces a re-circulation of the flow into the inducer stabilizing the flow at a lower mass flow rate. At choke, a positive pressure gradient between the inducer and the slot ensures a flow through the ported shroud increasing the choke limit of the compressor. Figure 1.6 shows a compressor ported shroud operating at surge and choke.

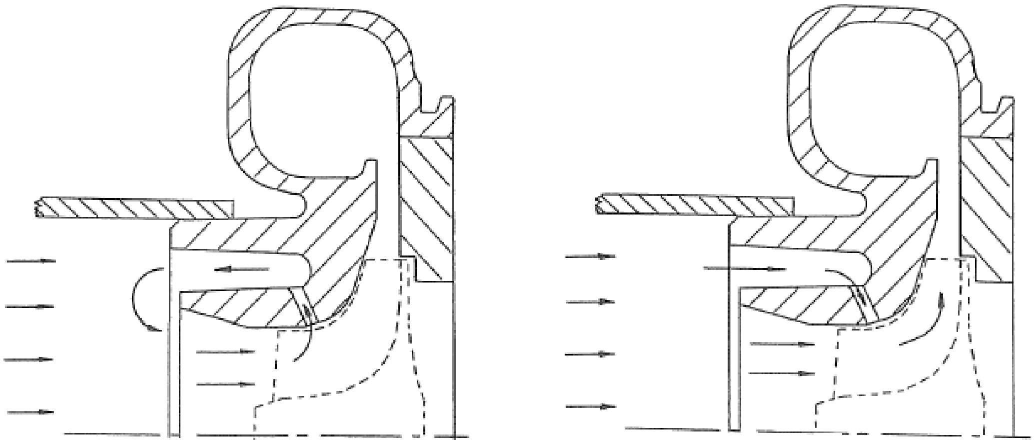
(a) (b)

Figure 1.6: Ported shroud operating at surge (A) and operating at choke (B)[2]

For transonic compressors impeller with splitter blades, the conventional single slot PS proposed by Fisher [10] may not be useful in extending the choke capacity due to aerodynamic and geometric blockages at the throat of the blade passage [19]. Shroud static pressure distribution for a compressor operating near choke shows that downstream of the leading edge (LE) of the splitter blades, a pressure gradient is observed which can be exploited to improve the choke capacity of the compressor by inducing mass flow of the air through the ported shroud. However, positioning the slot downstream of the LE of the splitter blades is not an ideal solution as it leads to efficiency loss at near surge operation of the compressor.

Active casing treatment (ACT) also known as double port casing treatment is proposed by different researchers [20, 21] to extend the compressor map using two ports with significant efficiency penalty. The first slot of the ACT, known as the surge slot, is open at all operating conditions. The surge slot is used to extend the surge margin of the compressor and is similar in design to the conventional casing treatment proposed by Fisher [6]. The second slot, known as the choke slot, opens when the mass flow rate of the flow is greater or equal to a preset value for a given rotational speed of the impeller. The function of the choke slot is to connect the inlet pipe with the area of the impeller just downstream of the splitter blade LE. The ACT design ensures the choke and surge limits improved independently with minimized efficiency and pressure ratio trade-offs.

The surge and choke controls in action are demonstrated in Figure 1.7.

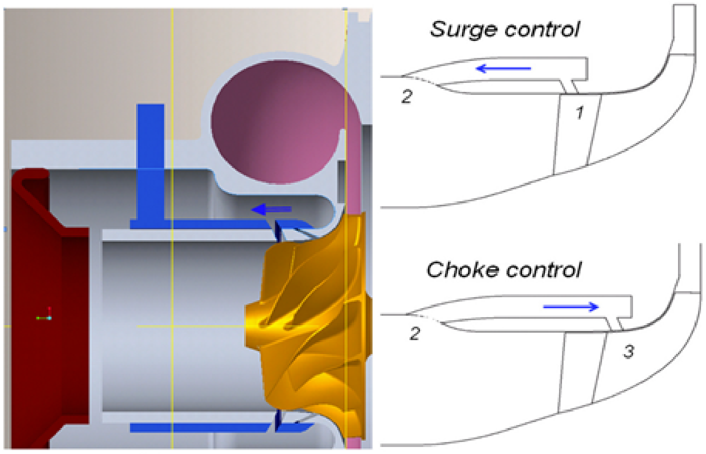

Figure 1.7: Active Casing Treatment System in Surge and Choke Operation [20]

Despite the advantages of casing treatments to widen the operating range, they are susceptible to high-frequency noise due to unsteady flow in the additional fluid paths of the shroud slots, thereby contributing to poor sound quality and decreasing the driver's comfort level.

1.1.3 Compressor Noise

Many researchers inrecent years have studied noise created by centrifugal compressors; Evans and Ward concluded the broadband 'whoosh' noise (also known as surge noise) in automotive turbochargers operating near full load acceleration is due to the turbulence generated when the compressor operates within or close to the marginal surge line [22]. Teng and Homco suggested that the surge noise can be reduced by improving the surge margin using a negative pre-whirl at the compressor inlet [23].

Raitor and Neise have studied sound generation mechanisms in centrifugal compressors to identify tonal noise at blade passing frequencies, buzz-saw noise, and blade tip clearance noise as the primary sources [24]. Despite many studies about centrifugal compressor flow acoustics, the effects of the casting treatment on the turbocharger acoustics is not is investigated extensively except experimental works by Dehner et.al. [21].

1.2 Turbocharger Turbines

The turbine stage of a turbocharger is connected to the engine by an exhaust manifold. The exhaust gases from each cylinder are gathered in a bank based on an engine firing order and then admitted towards the turbine stage inlet. Highly pressurized exhaust gases exert force on the turbine's impeller blades, causing the turbine to rotate. Euler's turbomachinery equation governs the transfer of energy between exhaust gases and turbine blades. Turbocharger turbine drives turbocharger compressor as coaxial shaft links the two components.

An engine exhaust manifold is connected to the radial turbine, illustrated in Figure 1.8, by a flange at its volute (station 1). Upon leaving the volute, the exhaust gas moves to the stator (2), which may or may not possess stator blades. The flow is then admitted to the turbine impeller inlet (station 4) radially. The flow expands inside the turbine rotor, transferring its energy to the rotor blades before leaving axially at the rotor exit (station 5).

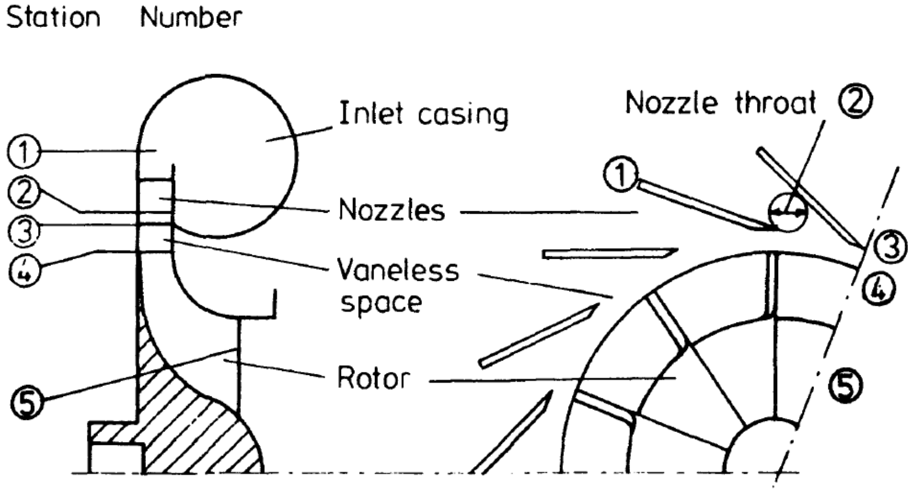

Figure 1.8: Radial turbine components [12]

Volutes in turbocharger radial turbines take engine exhaust flow, accelerate and distribute it around the circumference of the rotor/nozzle. In doing so the static pressure of the flow is reduced. An efficient volute is expected to distribute the flow uniformly, with less distortion of the flow angle.

For smaller automotive engines, the single-entry turbine is the most common option. Twin-scroll and double-entry volutes deliver lower efficiency values than the single entry turbine as their performance is reduced by the added dividing walls and multiple volute tongues.

Turbocharger turbines for engines with more than six cylinders are equipped with multiple-entry volutes to preserve exhaust gas pulses from engine exhaust pipes. The two common types of multiple-entry volutes are the twin-scroll and dual-entry volutes. In twin-scroll volutes, a fully circumferential dividing wall splits the flow into two separate flows. The flow from each scroll feeds the turbine inlet after a brief flow mixing at the volute outlet.

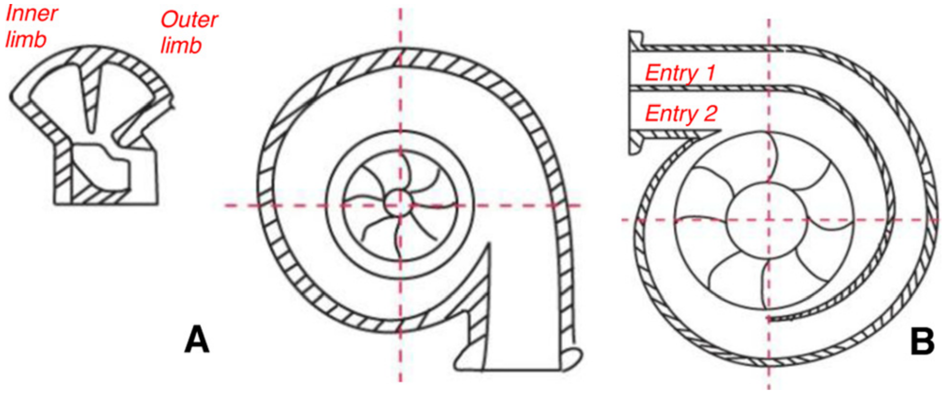

Figure 1.9: Turbocharger turbine with: (a) twin-scroll, and (b) double-inlet volute configurations [25]

Performance-wise, the double-entry turbines deliver a higher peak efficiency value than the twin-scroll turbine at equal admissions. On the contrary, in unequal-admission cases, the twin-scroll turbines efficiency is higher than the double-entry turbines. The efficiency deterioration of double-entry turbines at unequal admissions is correlated with the reduced effective turbine inlet circumferential area at unequal admission flow cases [26].

The twin-scroll volutes are further divided into symmetrical and asymmetrical volutes. In symmetrical volutes, the scroll dimensions at each azimuth angle are equal, while in asymmetrical volutes, one of the two scrolls has a larger size than the other.

The asymmetric twin-scroll turbines are usually employed at multiple-cylinder engines, which demand a higher EGR rate. The exhaust from the engine cylinders is grouped based on the engine firing order. An EGR line connected to one group of the exhaust manifolds boosts the engine inlet

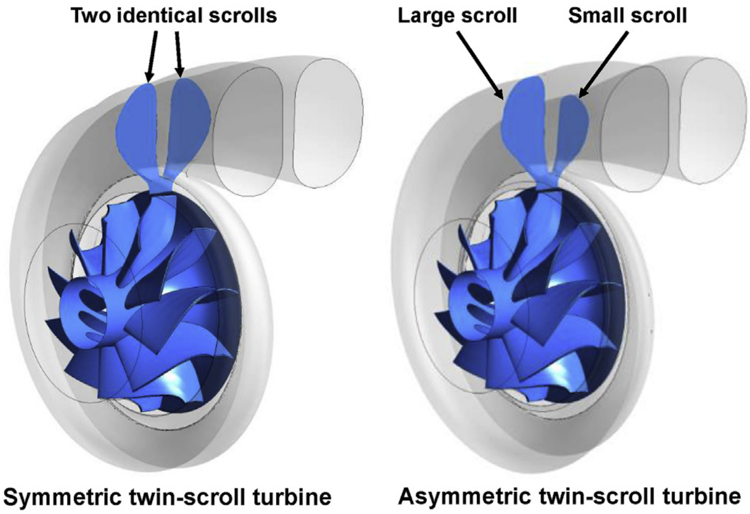

Figure 1.10: Symmetric and asymmetric twin-scroll configurations [27]

pressure. The exhaust manifold linked with the EGR line is fitted with a smaller scroll (also known as EGR scroll) at the turbine inlet to increase the back-pressure. The larger scroll (also known as Lambda scroll) usually has a lower back pressure as it is not linked with the EGR circuit [27, 26]. Figure 1.11 shows an engine fitted with asymmetric twin-scroll.

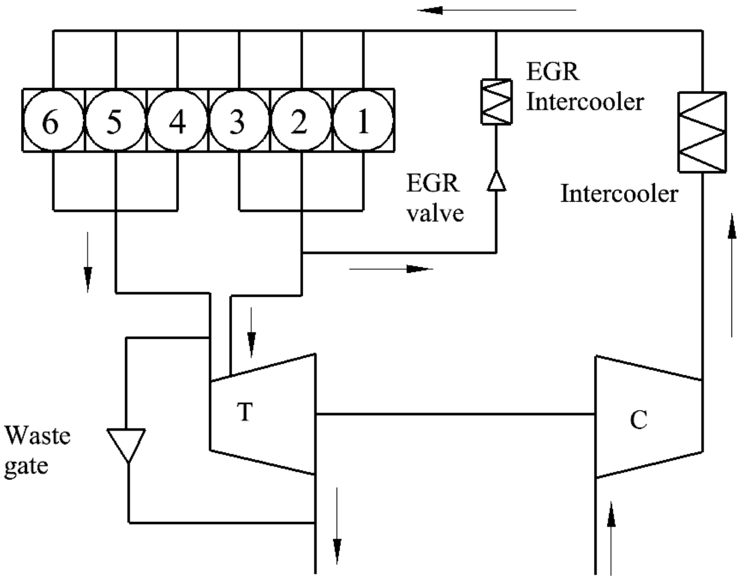

Figure 1.11: A schematic of a 6-cylinder asymmetric twin-scroll turbocharged diesel engine adapted from Zhu [27]

1.3 Motivation

The effect of different casing treatment designs on the turbocharger compressor surge to choke range and the aeroacoustics performance can be studied extensively using purely experimental and advanced CFD investigation. These studies tend to become expensive and inefficient as the number of design combinations increase. Thus, in-depth knowledge and understanding of the flow mechanism in casing treatments are beneficial in choosing the most critical design parameters to enhance the surge to choke margin and decrease undesirable compressor noise.

Finding the entropy sources in turbocharger turbines with double-entry scrolls at equal and unequal mass flow across the two entrances of the volute provides valuable insight into the potential advantage of the double-entry scroll over single-scroll and twin-scroll volutes. Finding the locality of the losses also assists the turbine performance optimization.

This dissertation investigates the aero-acoustics performance of a turbocharger compressor with active casing treatment at near surge and best efficiency points using Detached Eddy Simulation (DES) numerical simulation. Casing treatment geometry optimization will be accomplished based on an in-depth understanding of the flow mechanism in the casting treatment ports and compressor system parts. The dissertation also studies the effect of active casing treatment geometry on compressor performance. The turbocharger's active casing treatment geometry will be optimized to find the best design of the choke slot geometry that delivers an improved pressure ratio and isentropic efficiency values at lower mass flows.

The dissertation also assesses the performance of a dual-entry turbine to identify potential loss sources in the turbine assembly. Next, a single and twin-scroll design methodology will be presented to find the critical volute design parameters. Increased EGR flow into the Engine forces an increased uneven flow across the two turbine inlets of a twin-scroll turbine. Designing asymmetric twin scrolls with uneven flow across the turbine inlets requires a particular methodology.

1.4 Outline of the Thesis

The remainder of this work is presented in seven chapters. Chapters 2 and 3 present the theoretical background for the numerical analysis of the compressor and turbine performance. In chapter 2, different acoustics terms and sound analogies are discussed. The acoustics analogies defined in this chapter are used in Chapter 5 to investigate the aeroacoustic performance of the compressor. Chapter 3 details the governing equations of the computational methods used in this work. This chapter also presents the turbulence model used for the study in more depth, with an additional explanation for the setting of time and spatial discretization.

In Chapter 4, the compressor one and three-dimensional study is discussed. A unique compressor loss model is presented and compared with experimental data. This chapter also discusses the development of compressor maps based on CFD results. The final section of this chapter examines the effect of the casing treatment on the overall turbocharger compressor performance.

Chapter 5 details the turbocharger compressor aeroacoustics study based on steady-state and transient-state CFD schemes. The aeroacoustics analogies defined in Chapter 2 are used to predict the noise sources from the different compressor parts and surfaces. The pressure spectra of the compressor noise at two compressor operating points are also presented in this chapter, with an accurate prediction of the blade passing frequency and broadband noises. The noise directiveness is also predicted by placing monitor points strategically inside the compressor inlet and exit pipes.

Chapters 6 and 7 present the investigation on the casing of the turbocharger turbine. The performance of the double-entry turbine is studied thoroughly in Chapter 6 by estimating the entropy generated from each turbine component. This chapter reveals which turbine parts are more responsible for the turbine performance degradation at higher uneven flow across the two turbine inlets. In Chapter 7, a single-scroll and twin-scroll volute design methodology and optimization works are presented. The single-scroll and twin-scroll turbine performance is compared with the double-entry turbine, at even and uneven flow admissions. Finally, Chapter 8 concludes the dissertation with a summary of the important results and future works.

CHAPTER 2

AERODYNAMICS GENERATED NOISE

Sound is a wave detectable by human ear propagating in elastic medium. It is a result of pressure perturbation by a vibrating surface or a turbulent fluid flow. Humans can hear sounds with frequencies ranging between 20 Hz and 20 kHz. Sound in dry air at 20 °C propagates with speed of 343 m/s limiting the wavelengths of interest between 17 m and 17 mm. Because of the logarithmic response nature of human's ear, sounds at very low and very high frequencies are less critical for acoustic study. Thus, the frequency of interest in acoustic simulation ranges from 1-3 kHz [28].

Sound contains a wide range of power levels that are measured using the decibel scales. Sound Power Level (PWL), Sound Pressure Level (SPL), and sound intensity level are used to measure sound strength. The Sound Power Level (PWL) is given in decibel (dB) by,

$$PWL = 10\log_{10}\left(\frac{sound\ power}{reference\ power}\right) \tag{2.1}$$

The reference power is internationally agreed to be equal to 10^{-12} W. The Sound Pressure Level (SPL) is given by,

$$SPL = 20\log_{10}\left(\frac{p'_{rms}}{p_{ref}}\right) \tag{2.2}$$

where p'_{rms} is the root mean square acoustic pressure fluctuations p', and $p_{ref} = 2x10^{-5}Pa$ in an air medium. This reference pressure corresponds to the threshold of hearing at $1kHz$ for a typical human ear [29]. The time-averaged rate of energy transmitted by a sound wave propagating in a fluid is known as the sound intensity. The sound intensity level is defined by,

$$IL = 10\log_{10}\left(\frac{I}{10^{-12}\ W/m^2}\right) \tag{2.3}$$

2.1 Acoustic Analogies

Acoustic propagation involves small pressure perturbations traveling long distances. Disregarding the effects of viscosity and small perturbation products, the continuity and momentum equations are combined to give the linear acoustic wave equation. The acoustical wave equation describes the propagation of sound in a stationary medium. The addition of sound source terms to the wave equation gives [30],

$$\left(\frac{\partial^2}{\partial t^2} - C^2\Delta^2\right)(\rho - \rho_0) = Q\,(X, t) \tag{2.4}$$

In Eq.(2.4), Q represent the sound source and X is its space position. The acoustic source term Q is equal to the density generated due to mass and momentum creation. Far from a sound source, the value of Q is zero. The solution of Eq.(2.4) can be found using free space Green's function [30],

$$(\rho - \rho_0)\,(X, t) = \frac{1}{4\pi C_\infty^2}\int \frac{Q\,(y, t - |X - y|/C_\infty)}{|X - y|}dy \tag{2.5}$$

In Eq.(2.5), y is the location of the observer. Since the sound travels a distance of $r = |X - y|$ with a speed of sound C_∞, Eq.(2.5) is solved at a lagging time of $t^* = t - r/C_\infty$. When the sound source with a strength of $q(t)$ is concentrated at the origin, Eq.(2.5) will have a solution of form,

$$(\rho - \rho_0)\,(X, t) = \frac{1}{4\pi C_\infty^2}\frac{q\,(t - r/C_\infty)}{r} \tag{2.6}$$

The function $Q(X, t) = q(t)\delta(X)$ is called monopole source strength density. This sound source represents an injection of mass by a small pipe opening or the collapse of cavitation bubbles in a liquid [31]. The propagation of sound from monopole source is uniform and spreads equally in all directions.

When two equal and opposite monopole sound sources are positioned close together, a dipole sound source is formed. This sound source occurs due to unsteady external forces. They can be considered as a superposition of two out of phase monopole sound sources. When a pair of equal and opposite dipoles are positioned together a quadrupole is obtained. It represents a sound source from turbulent flow.

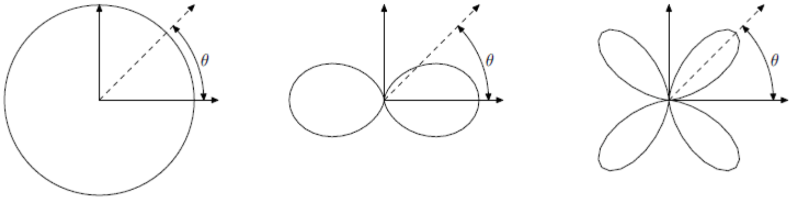

Figure 2.1: Monopole, dipole, and quadrupole source directivities [32]

2.1.1 Lighthill's Analogy

Lighthill analogy gives a correlation of sound generation by turbulent flow. The equation is derived from continuity and momentum equations without considering mass generation and external force application. The Lighthill's wave equation is given by,

$$\frac{\partial^2 \rho'}{\partial t^2} - C_\infty^2 \frac{\partial^2 \rho'}{\partial x_i^2} = \frac{\partial^2 T_{ij}}{\partial x_i \partial x_j} \tag{2.7}$$

where $\rho' = \rho - \rho_0$ is density perturbation relative to the surrounding medium, C_∞ is the ambient speed of sound outside the flow and T_{ij} is the Lighthill stress tensor given as:

$$T_{ij} = \rho v_i v_j + p_{ij} - (\rho - \rho_0) C_\infty^2 \delta_{ij} \tag{2.8}$$

Lighthill's equation is a hyperbolic partial differential equation. The left-hand side of the equation describes a wave propagating at a speed of sound, C_∞, in a medium at rest. The right-hand side of the equations describes the acoustic source term due to shear, unsteady convection, and non-linear effects. In Eq.(2.7), the static flow velocity is assumed to be zero as all convective velocity parts of the flow are included in Lighthill's stress tensor term. The source term also includes all viscous stress and entropy fluctuations, which means outside the source region the fluid encounters no losses due to viscosity or thermal conductivity. For this reason, it can be concluded in Lighthill's analogy the sound propagates in an ideal fluid outside of the sound source. In the absence of solid boundaries, the free field Green's function gives a solution for Lighthill's wave equation as [33],

$$\rho' = \rho - \rho_0 = \frac{1}{4\pi C_\infty^2} \frac{\partial^2}{\partial x_i \partial x_j} \int_V \frac{T_{ij}\left(y, t - |X - y|/C_\infty\right)}{|X - Y|} dy \tag{2.9}$$

In Eq.(2.9), all derivatives and values are taken at a retarded time, $t^* = t - |X - Y|/C_\infty$. Lighthill's equation is used to predict the sound from flows where the effect of solid boundaries can be neglected [34]. Solid surface interaction plays a direct role in the sound generation process in reflection and diffraction of the sound field from volume distribution of quadrupoles. Besides, solid surface boundaries might act as dipole or monopole sound sources.

2.1.2 Proudman Analogy

Using Lighthill's theorem, Proudman [35] derived an approximate correlation to predict the sound power from a statistically homogeneous isotropic turbulent flow as:

$$P = \alpha \rho_o \frac{u^3}{l} \frac{u^5}{c_o^5} \tag{2.10}$$

where α is constant, ρ_o is the density, u is the root mean square of the velocity derived from the turbulent kinetic energy, l is the integral length scale, and c_o is the far field speed of sound.

2.1.3 Curle's Analogy

An extension of Lighthill's analogy that considers solid boundaries in arbitrary motion is developed by Ffowcs Williams and Hawkings (FWH) [36]. Curle [33] gives the solution to the Lighthill equation using free-space Green's function when rigid and stationary solid bounders are present in the flow. The Curle's equation can be considered as a specific form of FWH as given by:

$$\rho'(X,t) = \frac{1}{4\pi C_\infty^2} \frac{\partial^2}{\partial x_i \partial x_j} \int_V \frac{T_{ij}}{|X-Y|} d^3y + \frac{1}{4\pi C_\infty^2} \frac{\partial}{\partial x_i} \int_S \left[\frac{p' n_i}{|X-Y|} \right] d^2y \tag{2.11}$$

The first part of the Curle's equation in Eq.(2.11) estimates the sound generated from a quadrupole source whereas the second part gives an estimation from a dipole source.

2.2 Computational Aeroacoustics

Direct (also known as hybrid) computational methods can be used to estimate flow generated noise numerically. In this method, the sound is resolved together with its fluid dynamics source field by solving the Navier-Stokes equations of compressible flow. Advanced turbulence models, such as direct numerical simulation (DNS), large-eddy simulation (LES), and detached eddy simulations (DES) are preferred to unsteady Reynolds-averaged Navier-Stokes (URANS) as they can solve most of the flow scales.

In indirect/hybrid computation approach of CAA, sound computation is done in separate post-processing of the flow solution. Integral or numerical solutions of the acoustic analogy equations of the computed source field data are then used to compute far-field sound. Indirect/hybrid approaches are based on the principle that sound generating unsteady flow is not affected by the sound waves as pressure perturbation responsible for generating sound have relatively insignificant value.

2.3 Turbocharger Noise

The primary aerodynamic noise generating mechanisms in turbo-compressors are buzz-saw noise tonal noise at blade passing frequencies and blade tip clearance noise [37]. Buzz-Saw Noise occurs near the leading edge of the rotor blades at supersonic flow condition. A combination of shock and expansion wave create a pressure signature that resembles a circular buzz-saw [38]. Due to the rotor manufacturing irregularities, the buzz-saw pressure distributions are not circumferentially identical. The blade produces buzz-saw noise, a monopole type source, with its contribution felt as harmonics of the rotor shaft frequency.

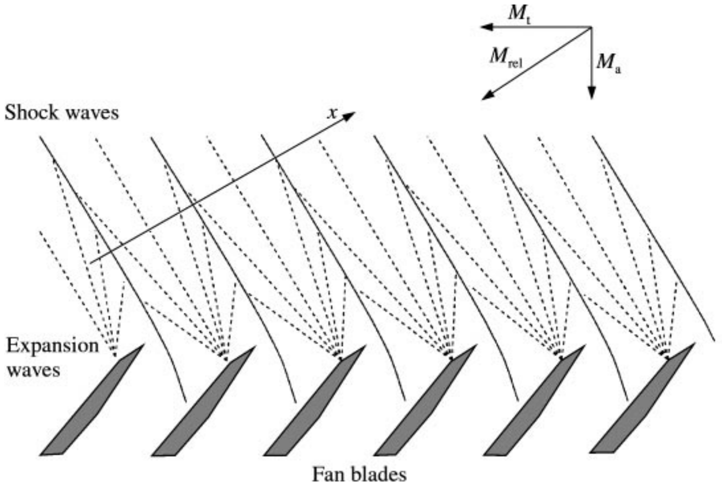

Figure 2.2: Shock-wave generation by a supersonic fan [38]

Inflow disturbances and rotor-stator interactions create a fluctuating pressure source, a dipole source, of noise. This acoustic signal consists of harmonics of the blade passing frequency (BPF) defined as the product of the rotor shaft frequency fn and the number of main rotor blades. The secondary flow through the gap between the compressor casing and the impeller blades induced a narrow-band noise termed as “tip clearance noise” (TCN). The effect of TCN is pronounced at mass flow rates less than the design flow rate [24].

CHAPTER 3

NUMERICAL MODELING

3.1 Governing Equations

The Navier-stokes equations of fluid dynamics are the foundations of aeroacoustics. The governing equations for conservation of mass, momentum, and energy for a compressible fluid in a tensor form are given by:

$$\frac{\partial \rho}{\partial t} + \frac{\partial \rho v_i}{\partial x_i} = 0 \tag{3.1}$$

$$\frac{\partial \rho v_i}{\partial t} + \frac{\partial \rho v_i v_j}{\partial x_j} = -\frac{\partial p}{\partial x_i} + \frac{\partial \sigma_{ij}}{\partial x_j} + f_i \tag{3.2}$$

$$\frac{\partial}{\partial t}\left[\rho\left(e + \frac{v_i^2}{2}\right)\right] + \frac{\partial}{\partial x_i}\left[\rho v_i\left(e + \frac{v_i^2}{2}\right)\right] = -\frac{\partial\left(p v_i\right)}{\partial x_i} + \frac{\partial\left(\sigma_{ij} v_j\right)}{\partial x_i} - \frac{\partial q_i}{\partial x_i} + \rho f_i v_i \tag{3.3}$$

with ρ being the density, t is time, x is the coordinate axis, subscripts i, j, k are the direction indices, v is the velocity, p is the pressure, σ_{ij} is the viscous stress tensor, e is the internal energy, q_i is the heat flux, f_i represents the external body forces.

The above Eq.(3.1,3.2,3.3) are non-linear systems of partial differential equations which are solved numerically. The equation of state relates pressure, density, and temperature.

$$p = \rho R T \tag{3.4}$$

where R is the gas constant, T is the temperature. Internal energy in Eq.(3.4) can be computed as a product of specific heat ratio at constant volume (c_v) and temperature.

$$e = c_v T \tag{3.5}$$

The viscous stress tensor terms in Eq.(3.2) gives a linear stress-strain relationship and is given by,

$$\sigma_{ij} = 2\mu\left(S_{ij} - \frac{1}{3} S_{kk}\delta_{ij}\right) \tag{3.6}$$

where μ is the dynamic viscosity and S_{ij} is the rate of strain tensor given by,

$$S_{ij} = \frac{1}{2}\left(\frac{u_i}{x_j} + \frac{u_j}{x_i}\right) \tag{3.7}$$

The heat flux is assumed in Eq.(3.3) is computed by Fourier's law as,

$$q_j = -k\frac{\partial T}{\partial x_j} \tag{3.8}$$

where k, the thermal conductivity of the fluid is temperature dependent.

3.2 Turbulence

Turbulent flows are chaotic and random. Statistical methods are used to find properties of turbulent flows as an entirely deterministic solution is impossible for most fluid flow cases. The highly diffusive nature of turbulence flow causes rapid mixing and increased rates of momentum, heat and mass transfer. The viscous shear stresses in turbulent flows lead to the conversion of kinetic energy into heat. Thus, turbulent flows are dissipative. Turbulent flow occurs at high Reynolds numbers where inertia terms dominate the viscous terms in the momentum equations. On the other hand, laminar flows are deterministic and highly ordered. Reynolds number quantifies the transition from laminar to turbulent flow.

$$Re = \frac{UL}{\nu} \tag{3.9}$$

For a particular flow regime, depending on the value of the Reynolds number flow is categorized to be laminar or turbulent.

3.2.1 Turbulence modeling

Direct numerical simulations (DNS) solves the fully unsteady Navier-Stokes equations on a sufficiently fine grid using a small-time step so that all length and time scales of the turbulent flow are fully resolved. DNS has an advantage of delivering an accurate transient behavior of the flow. Despite its advantages, the intensive computational cost needed for DNS has up to date limited the suitability of the simulation to any applications of engineering interest. Its use is limited for simple flows with low Reynolds number to provide an insight of turbulence modeling. This has led to turbulent models where some or all part of the turbulent eddies of flow are modeled.

3.2.1.1 Reynolds-averaged Navier-Stokes (RANS)

Reynolds-averaged Navier-Stokes (RANS) equations give time-averaged properties of the flow without resolving the details of turbulent fluctuations. The effects of turbulence on the mean flow are considered from Reynolds stress terms. Different turbulent models with additional transport equations are used to solve the Reynolds stress terms with empirical constants and additional information about the mean flow.

The solution variables in RANS are decomposed into the mean and fluctuating components. For the velocity this decomposition is given as:

$$u_i = \overline{u}_i + u'_i \tag{3.10}$$

where $\overline{u_i}$ and u'_i are the mean and fluctuating velocity components. Substituting this form of expressions into the Navier-Stokes equations gives a momentum equation of the form:

$$\frac{\partial}{\partial t}(\rho u_i) + \frac{\partial}{\partial x_j}(\rho u_i u_j) = -\frac{\partial p}{\partial x_i} + \frac{\partial}{\partial x_j}\left[\mu\left(\frac{\partial u_i}{\partial x_j} + \frac{\partial u_j}{\partial x_i} - \frac{2}{3}\sigma_{ij}\frac{u_i}{x_j}\right)\right] + \frac{\partial}{\partial x_j}\left(-\rho\overline{u'_i u'_j}\right) \tag{3.11}$$

The additional Reynolds Stress terms in Eq.(3.11),$-\rho\overline{u'_i u'_j}$, represent the effects of turbulence, and they must be modeled to have a solution of the Navier-Stokes equation. The most widely used turbulent models, $k-\epsilon$, $k-\omega$ and Spalart-Allmaras models use the Boussinesq hypothesis to relate the Reynolds stresses to the mean velocity gradients as given by:

$$-\rho\overline{u'_i u'_j} = \mu_t\left(\frac{\partial u_i}{\partial x_j} + \frac{\partial u_j}{\partial x_i}\right) - \frac{2}{3}\left(\rho k + \mu_t\frac{\partial u_j}{\partial x_i}\right)\delta_{ij} \tag{3.12}$$

where μ_t is the turbulent viscosity and k is the turbulence kinetic energy. The Boussinesq hypothesis assumes the turbulent viscosity of an isotropic scalar quantity which is not valid in the entire flow regime [39].

3.2.1.2 Large Eddy Simulation (LES)

LES uses a spatial filtering operation to separate the larger energy carrying eddies from, the smaller eddies. The motivation for LES is that the smaller scale eddies are relatively universal and isotropic and easy to model while the large-scale eddies are challenging to model as they are problem-dependent [40]. LES uses a filtering function on Navier-Stokes equations over the mesh grid with a specific cutoff width. The unsteady flow is resolved for all length scales greater than the cutoff width [41]. Turbulence scales small than a simple Eddy Viscosity model models the filter. The filtered Navier-Stokes equations for incompressible flow is given by [39]

$$\frac{\partial}{\partial t}\left(\rho \overline{u}_i\right) + \frac{\partial}{\partial x_j}\left(\rho \overline{u}_i\, \overline{u}_j\right) = \frac{\partial}{\partial x_j}\left(\mu \frac{\partial \overline{u}_i}{\partial x_j}\right) - \frac{\partial \overline{p}}{\partial x_i} - \frac{\partial \tau_{ij}}{\partial x_j} \tag{3.13}$$

where τ_{ij} is the subgrid-scale stress defined by

$$\tau_{ij} = \rho \overline{u_i u_j} - \rho \overline{u}_i\, \overline{u}_j \tag{3.14}$$

The eddy viscosity models are used to model the subgrid-scale stresses from the filtered equation

$$\tau_{ij} - \frac{1}{3}\tau_{kk}\delta_{ij} = -2\mu_t \overline{S}_{ij} \tag{3.15}$$

where μ_t is the subgrid-scale turbulent viscosity, and $\overline{S}_{ij}$is the strain tensor rate of the resolved scale defined by:

$$\overline{S_{ij}} = \frac{1}{2}\left(\frac{\partial \overline{u}_i}{\partial x_j} + \frac{\partial \overline{u}_j}{\partial x_i}\right) \tag{3.16}$$

Smagorinsky model define the turbulent viscosity, $\mu_t$in equation Eq.(3.15) [40]:

$$\mu_t = \rho\left(C_s \Delta\right)^2 \overline{S} \tag{3.17}$$

where Δ is a measure of the grid spacing of the numerical mesh, $\overline{S}$ is the strain rate scalar, and C_s is a constant. Due to relatively coarser mesh than DNS, LES is not capable of accurately resolving smallest scales. The importance of LES arises from the need to model the dissipation of the smallest resolved scales. Figure 3.1 shows the range of LES resolved and modeled turbulence scales.

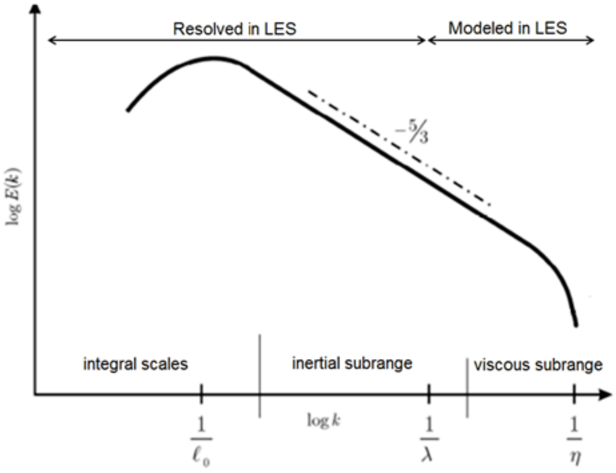

Figure 3.1: Turbulence energy spectrum

The eddy viscosity is calibrated to predict the correct amount of dissipation at the LES grid limit by,

$$\epsilon_{LES} = \nu_t \frac{\partial \overline{u}_i}{\partial x_j} frac\partial\overline{u}_i\partial x_j \tag{3.18}$$

where ν_t is the turbulent kinematic viscosity

Applying LES to wall-bounded flows demands higher resolution grid in all three directions as the turbulent length scale of the larger eddies become very small. The Kolmogorov limit gives the smallest turbulent scales near to the wall. The viscous sublayer near to the wall, where turbulence is damped and does not to be resolved, gets thinner as the flow Reynolds number increases. For most engineering applications where the flow Reynolds number is moderately higher, LES becomes computationally expensive [40].

3.2.1.3 Detached Eddy Simulation (DES)

Detached Eddy Simulation (DES) is a hybrid modeling approach that uses RANS simulation for part of the flow near to the wall and LES for part of flow far enough from the wall. A relatively coarser mesh is used for larger eddies which are resolved using LES and RANS is used for all wall-bounded flows.

Based on the grid resolution provided, DES switches between RANS and LES using a criterion that considers a multiplication of a DES constant with the maximum edge length of the local computational mesh cell. The Menter's $k - \omega - SST$ [42] turbulence model is modified to define a length scale for DES as given by [43]:

$$\tilde{l} = min\left(l_{k-\omega}, C_{DES}\Delta\right) \tag{3.19}$$

where $C_{DES}\Delta$ is the DES filter length. C_{DES} is a constant with a value of 0.61. $l_{k-\omega}$ is the length scale of RANS $k - \omega - SST$ model defined as:

$$l_{k-\omega} = \frac{k^{1/2}}{\beta * \omega} \tag{3.20}$$

where k is the turbulent kinetic energy, $\beta*$ is model constant, and ω is specific dissipation rate. The modified dissipative term in k-transport equation becomes,

$$D_{DES} = \frac{\rho k^{3/2}}{\tilde{l}} \tag{3.21}$$

Spatial refinement creates an ambiguity on the model to differentiate between LES and RANS regions of the mesh. Delayed Detached Eddy Simulation (DDES) is used to address this issue by using a delay factor. Improved Delayed Detached Eddy Simulation (IDDES) improves DDES to include Wall model LES (WMLES) models allowing RANS to be used in a wall distance much smaller than the boundary layer thickness [44].

CHAPTER 4

COMPRESSOR PERFORMANCE ANALYSIS

The compressor impeller is responsible for the increase in stagnation enthalpy of the flow. The specific energy change across the impeller can be calculated from the inlet and outlet velocity triangles using Euler's turbomachinery equation. For turbocharger compressor without any pre-whirl vanes, the ideal enthalpy transfer to the flow is given by:

$$\Delta h_{0,i} = U_2 C_{u2} \tag{4.1}$$

In actual flows, the impeller flow at the exit deviates from the blade direction. A slip factor, σ, reduces the tangential component of the absolute velocity at the impeller exit. Slip factor refers to the ratio between the actual (C_{u2}) and theoretical ($C_{u2,th}$) tangential components of the absolute velocity of the impeller exit. The slip factor is defined as:

$$\sigma = C_{u2}/C_{u2,th} \tag{4.2}$$

The theoretical tangential component of the absolute velocity at the impeller exit can be estimated from the velocity triangle at the impeller exit as:

$$C_{u2,th} = U_2 - C_{m2}\cot(\beta_{2b}) = U_2 - \frac{\dot{m}}{\rho_{02}A_2}\cot(\beta_{2b}) \tag{4.3}$$

The ideal rise in enthalpy of the actual flow can be estimated by plugging Eq.(4.3) in to Eq.(4.2) as:

$$\Delta h_{0,i} = \sigma U_2^2 \left(1 - \frac{\dot{m}}{\rho_{02}A_2U_2}\cot(\beta_{2b})\right) \tag{4.4}$$

The ideal change in enthalpy of the flow across the impeller is a function of the mass flow rate, rotational speed, and the impeller back sweep blade angle. The change in enthalpy decreases as the flow rate increases for impellers with back sweep angle.

In the open literature, there are many correlations for slip factor. One of the widely used correlations is developed by Wiesner [45] as given by:

$$\sigma = 1 - \frac{\sqrt{\sin\beta_2}}{Z_b^0.7} \tag{4.5}$$

Aungier [46] presented a corrected form of the slip factor by Wiesner. In Aungier's correlation, the Wiesner's slip factor holds up to a certain limiting radius ratio, ϵ_{LIM}. If the radius ratio, ϵ, is greater than ϵ_{LIM}, the slip factor is given by:

$$\sigma_{COR} = \sigma \left[1 - \left(\frac{\epsilon - \epsilon_{LIM}}{1 - \epsilon_{LIM}} \right)^{\sqrt{\beta_2/10}} \right] \tag{4.6}$$

where σ is the Wiesner slip factor defined in Eq.(4.5) and ϵ is the impeller meanline radius ratio (r_1/r_2) and ϵ_{LIM} is the limiting radius ratio given by:

$$\epsilon_{LIM} = \frac{\sigma - \sigma^*}{1 - \sigma^*} \tag{4.7}$$

In Eq.(4.7) σ^* is given by:

$$\sigma^* = \sin\left(19^0 + 0.2\beta_2\right) \tag{4.8}$$

Qiu et al. [47] presented an alternative slip factor correlation based on the shape factor F as:

$$\sigma = 1 - \frac{F\pi\cos(\beta_{2b})\sin(\gamma_2)}{Z_2} - \frac{Fs_2\phi_2}{4\cos(\beta_{2b})}\left(\frac{d\beta}{dm}\right) + \frac{Fs_2\phi_2\sin(\beta_{2b})}{4\rho_2 b_2}\left(\frac{d\rho b}{dm}\right) \tag{4.9}$$

where γ_2 is the meridional inclination angle at the impeller exit, Z_2 is the number of blades at the impeller exit, $d\beta/dm$ is the blade turning rate, ρ is density, and F is the shape factor defined as:

$$F = 1 - 2\sin\left(\frac{\pi}{Z_2}\right)\sin\left(\frac{\pi}{Z_2} + \beta_{2b}\right)\cos(\beta_{2b})sin(\gamma_2) - \frac{t_2}{s_2\cos\beta_{2b}} \tag{4.10}$$

Numerous researchers have presented multiple loss models for the compressor impeller and diffuser flow depending on experimental results. The contribution of each loss in determining the compressor efficiency and pressure ratio values are discussed using Eckart B centrifugal compressor data. The different losses models used in this study are listed below.

4.1 Compressor Stage Losses

The impeller loss models are classified as internal losses and external losses. The internal losses include the incidence, blade loading, skin friction, mixing, clearance, and choke losses, while the external losses consist of disk friction loss, recirculation loss, and leakage loss.

4.1.1 Incidence Loss

The incidence loss estimates the loss due to a relative flow angle deviation from the design blade angle at the impeller entrance. Galvas [48] offers a correlation for the enthalpy lost to incidence, assuming the relative velocity component normal to the optimum incidence angle is lost.

$$\Delta h_{inc} = \frac{(W_1 \sin(|\beta_{1b} - \beta_1|))^2}{2} \tag{4.11}$$

where W_1 is the flow relative velocity and β_{1b} and β_1 are the blade and flow angles from the tangential direction. Conard et al. [49] proposed another correlation for incidence loss:

$$\Delta h_{inc} = f_{inc}\frac{W_{\theta 1}^2}{2} \tag{4.12}$$

where f_{inc} is a factor ranging from 0.5 to 0.7 and $W_{\theta 1}$ is the kinetic energy lost as the flow angle deviates from β_{1b} to β_1. For a flow with no pre-whirl $W_{\theta 1}$ is given by:

$$W_{\theta 1} = U_1 - \frac{\cot(\beta_{1b})\,\dot{m}}{\rho_1 A_1} \tag{4.13}$$

Aungier [46] formulated an alternative incidence loss model given by:

$$\Delta h_{inc} = 0.4\left(W_1 - \frac{C_{m1}}{\sin(\beta_1)}\right)^2 \tag{4.14}$$

Eq.(4.14) is computed at the hub, mean, and shroud radius. The final value of the incidence loss is estimated using a weighted average of the three values, with the value at the mean radius weighing ten times more than those at the hub and the shroud radius.

4.1.2 Blade Loading Loss

The blade loading loss represents the losses associated with the boundary layer growth in the impeller flow channel. Coppage et al. [50] presented a correlation to estimate the blade loading loss:

$$\Delta h_{bl} = 0.05 D_f^2 u_2^2 \tag{4.15}$$

where the D_f the diffusion factor is given by:

$$D_f = 1 - \frac{W_2}{W_{s1}} + \frac{0.75 * \Delta h_{Euler} W_2}{\left[\frac{Z}{\pi}\left(1 - \frac{d_{s1}}{d_2}\right) + 2\frac{d_{s1}}{d_2}\right]} \tag{4.16}$$

where Δh_{Euler} is the ideal change in enthalpy calculated by the Euler equation:

$$\Delta h_{Euler} = u_2 c_{2u} - u_1 c_{1u} \tag{4.17}$$

Aungier [46] proposed an alternative method of calculating blade loss.

$$\Delta h_{bl} = \frac{\Delta W^2}{48} \tag{4.18}$$

where the average blade velocity difference between the suction and the pressure surface, ΔW, is calculated as:

$$\Delta W = \frac{2\pi d_2 u_2 I_B}{z L_B} \tag{4.19}$$

In Eq.(4.19), I_B is the blade work input coefficient, z is the impeller effective number of blades, and L_B is the blade mean camberline length.

4.1.3 The Skin Friction Loss

Skin friction loss considers losses due to shear stresses in the boundary layers of the impeller channel surfaces. Jansen [51] presented a skin friction loss model based on a similar method of calculating the total pressure drop for straight pipes.

$$\Delta h_{sf} = 2C_f \frac{L_B}{D_H} \overline{W}^2 \tag{4.20}$$

where L_B is the flow length defined as:

$$L_B = \frac{\pi}{8}\left[d_2 - \frac{d_{s1} + d_{h1}}{2} - b_2 + 2L_z\right]\left(\frac{2}{\frac{\sin(\beta_{s1}) + \sin(\beta_{h1})}{2} + \sin(\beta 2)}\right) \tag{4.21}$$

In Eq.(4.20), d_H is the average hydraulic diameter of a blade passage and is defined as:

$$\frac{d_H}{d_2} = \frac{\sin(\beta_2)}{\left[\frac{Z}{\pi} + \frac{d_2 \sin(\beta_2)}{b_2}\right]} + \frac{\frac{1}{2}\left(\frac{d_{s1}}{d_2} + \frac{d_{h1}}{d_2}\right)\left(\frac{\sin(\beta_{s1}) + \sin(\beta_{h1})}{2}\right)}{\frac{Z}{\pi} + \left(\frac{d_{s1} + d_{h1}}{d_{s1} - d_{h1}}\right)\left(\frac{\sin(\beta_{s1}) + \sin(\beta_{h1})}{2}\right)} \tag{4.22}$$

Jansen [51] defined the average velocity of the flow, $\overline{W}$, as:

$$\overline{W} = \frac{2W_2 + W_{s1} + W_{h1}}{4} \tag{4.23}$$

Aungier [46] provided another correlation for the average flow velocity as:

$$\overline{W}^2 = \frac{W_1^2 + W_2^2}{2} \tag{4.24}$$

The skin friction coefficient in Eq.(4.20) depends on the surface finish of the flow channel surfaces and the flow Reynold's number. Numerous correlations have been proposed in the open literature for the skin friction coefficient. Haaland's [52] formula explicitly estimates the skin friction coefficient as a function of Reynolds number and the surface finish roughness value as:

$$\frac{1}{\sqrt{f}} = -1.8\left[\left(\frac{e/d_H}{3.7}\right)^{1.11} + \frac{6.9}{Re}\right] \tag{4.25}$$

4.1.4 The Mixing Loss

The mixing loss considers the loss due to the mixing of the jet and wake flows from the impeller exit into the vaneless diffuser channel. Johnston and Dean [53] presented the mixing loss model as:

$$\Delta h_{mix} = \frac{1}{1 + \cot^2_{\alpha_2}}\left[\frac{1 - \epsilon_{wake} - b^*}{1 - \epsilon_{wake}}\right]^2 \frac{C_2^2}{2} \tag{4.26}$$

where ϵ_{wake} is the fraction of blade-to-blade space occupied by the wake whereas b^* is the ratio of diffuser inlet depth to impeller tip. The ϵ_{wake} can be estimated using a two zone model as outlined in Oh et al. [54] and Japikse [55].

Aungier [7] derived a different equation to determine mixing loss by calculating the velocity at which separation occurs as:

$$\Delta h_{mix} = \left(C_{m,wake} - C_{m,mix}\right)^2 \tag{4.27}$$

The flow meridional velocities of the wake before and after mixing are given as:

$$\begin{aligned} C_{m,wake} &= \sqrt{W_{SEP}^2 - W_U^2} \\ C_{m,mix} &= C_{m2}A_2/(\pi d_2 b_2) \end{aligned} \tag{4.28}$$

The flow separation velocity is used to evaluate the wake size, which is evaluated from the equivalent diffusion factor, D_{eq}.

$$\begin{aligned} W_{SEP} &= W_2;\ D_{eq} \leq 2 \\ W_{SEP} &= W_2 D_{eq}/2; \quad D_{eq} > 2 \end{aligned} \tag{4.29}$$

The equivalent diffusion factor is calculated from the ratio maximum relative velocity to the relative velocity at the exit.

$$\begin{aligned} W_{max} &= (W_1 + W_2 + \Delta W)/2 \\ D_{eq} &= W_{max}/W_2 \end{aligned} \tag{4.30}$$

4.1.5 The Clearance Loss

The leakage loss results from the flow leaking through the tip clearance gap between the rotating impeller and the stationary compressor housing due to the pressure difference between the suction side and the pressure side of the compressor blades. Jansen [51] provides a correlation for the clearance loss as:

$$\Delta h_{cl} = 0.6 \left(\frac{s}{b_2}\right) C_{\theta 2} \left\{ \frac{4\pi}{b_2 Z} \left[\frac{r_{s1}^2 - r_{h1}^2}{(r_2 - r_{s1})(1 + \rho_2/\rho_1)} \right] C_{\theta 2} C_{m1} \right\}^{1/2} \tag{4.31}$$

In Eq.(4.31) s is the tip clearance gap.

Aungier [7] presented an alternative method to estimate the clearance loss by calculating the mass flow rate through the clearance gap.

$$\dot{m}_{CL} = \rho_2 Z s L U_{CL} \tag{4.32}$$

The leakage flow velocity across the clearance gap, U_{CL}, is calculated as:

$$U_{CL} = 0.816\sqrt{2\Delta p_{CL}/\rho_2} \tag{4.33}$$

In Eq.(4.33), p_{CL} represents the average pressure difference across the gap and it is estimated from the angular momentum change through the impeller:

$$p_{CL} = \frac{\dot{m}(r_2 C_{U2} - r_1 C_{U1})}{\bar{r}\bar{b}L} \tag{4.34}$$

The average radius and width of the blade in Eq.(4.34) is given by:

$$\begin{aligned} \overline{r} &= (r_1 + r_2)/2 \\ \overline{b} &= (b_1 + b_2)/2 \end{aligned} \tag{4.35}$$

The Aungier clearance loss model becomes:

$$\Delta h_{cl} = 2\dot{m}_{CL}\Delta p_{CL}/\dot{m}\rho_1 \tag{4.36}$$

4.1.6 The Disc Friction Loss

The disc friction loss results from the secondary flow between the back of the impeller and the stationary compressor housing. Daily and Nece [56] estimated the disc friction loss as:

$$\Delta h_{df} = c_{df}\frac{\overline{\rho} r_2^2 u_2^3}{4\dot{m}} \tag{4.37}$$

where $\overline{\rho}$ is the average density given as:

$$\overline{\rho} = \frac{\rho_1 + \rho_2}{2} \tag{4.38}$$

The friction constant, c_{df}, is calculated based on the Reynold's number as:

$$\begin{aligned} c_{df} &= 2.67 Re_{df}^{-0.5}, \quad Re_{df} < 3 \times 10^5 \\ c_{df} &= 0.0622 Re_{df}^{-0.2}, \quad Re_{df} \geq \times 10^5 \end{aligned} \tag{4.39}$$

The Reynold's number in Eq.(4.39) is calculated from the impeller tip values.

$$Re_{df} = \frac{u_2 r_2}{\nu_2} \tag{4.40}$$

Galvas [48] presented another correlation for the disk friction loss as:

$$\Delta h_{df} = 0.01356\frac{\rho_2}{\dot{m}Re^{0.2}}u_2^3 D_2^2 \tag{4.41}$$

4.1.7 The Recirculation Loss

The recirculation loss considers the lost useful energy due to the low momentum wakes at the impeller exit forcing a backflow into the impeller. Coppage et al. [50] presents the following correlation for the recirculation loss as:

$$\Delta h_{rc} = 0.02 D_f^2 \cot(\alpha_2) \tag{4.42}$$

where D_f is diffusion factor defined in Eq.(4.16). Aungier [46] provides an alternative correlation to estimate the recirculation loss based on the equivalent diffusion factor:

$$\Delta h_{rc} = (D_{eq}/2 - 1)[w_{u2}/c_{m2} - 2\cot(\beta_2)]u_2^2 \tag{4.43}$$

In Eq.(4.43) the diffusion factor, D_{eq}, is calculated by Eq.(4.30).

Oh et al. [8] stated that the recirculation loss from experimental tests fall between the loss estimated by using Coppage et al. [50] and Aungier [46] methods. They proposed a new correlation for the recirculation loss as:

$$\Delta h_{rc} = 8 \times 10^{-5} \sinh\left(3.5\alpha_2^3\right) D_f^2 u_2^2 \tag{4.44}$$

The diffusion factor, D_f, in Eq.(4.44) is calculated by Eq.(4.16)

4.1.8 The Choke Loss

At higher mass flow rates, the pressure ratio of the flow drops rapidly when the Mach number at the impeller throat approaches one. Aungier [7] formulated the choking loss model as:

$$\begin{aligned} \Delta h_{ch} &= 0, \quad x \leq 0 \\ \Delta h_{ch} &= w_1^2(0.05x + x^7)/2, \quad x > 0 \end{aligned} \tag{4.45}$$

where x in Eq.(4.45) is calculated as:

$$x = 11 - 10 C_r A_{th}/A^* \tag{4.46}$$

In Eq.(4.46), A_{th} and A^* represent the throat and the flow critical areas respectively. C_r represents the contraction ratio defined as:

$$C_r = \sqrt{A_1 \sin(\beta_1)/A_{th}} \tag{4.47}$$

4.1.9 The Vaneless Diffuser Loss

The skin friction loss in the diffuser is considered in the efficiency and pressure ratio estimations as part of the internal losses. Aungier [7] developed a diffuser flow model that uses upstream flow conditions estimated from the impeller model and the diffuser geometry definition. The model uses finite difference formulation of the continuity, conservation of angular momentum and conservation of linear momentum equations and estimate the temperature, pressure, and velocity values at the diffuser exit. The conservation equations are:

$$2\pi r \rho b C_m (1 - B) = \dot{m} \tag{4.48}$$

$$b C_m \frac{d(rC_u)}{dm} = -rCC_u C_f \tag{4.49}$$

$$\frac{1}{\rho}\frac{dp}{dm} = \frac{C_u^2}{r} - C_m \frac{dc_m}{dm} - \frac{CC_m c_f}{b} - \frac{dI_D}{dm} \tag{4.50}$$

where b is the vaneless diffuser width, B is the area blockage due to the boundary layer growth, c_f is the skin friction coefficient, I_D is the diffusion loss term, and m is the meridional coordinate.

Staniz [57] derived another correlation to estimate the vaneless diffuser loss by using continuity, meridional momentum , tangential momentum, heat transfer, and fluid state equations as:

$$\Delta h_{vld} = C_p T_{02} \left[\left(\frac{P_3}{P_{03}} \right)^{(\gamma-1)/\gamma} - \left(\frac{P_3}{P_{02}} \right)^{(\gamma-1)/\gamma} \right] \tag{4.51}$$

where p_3 and p_{03} represent the static and stagnation pressures of the flow at the diffuser exit.

Galvas [48] presented a simplified form of the Staniz diffuser flow model by assuming adiabatic flow. The total pressure change inside the diffuser is estimated using the relation by Coppeage et al. [50].

4.1.10 The Volute Loss

Aungier [7] presented one-dimensional performance analysis of volutes based on Weber and Koronowski [58] analysis. The meridional component of the diffuser exit velocity is assumed to be lost entirely, while the loss due to the tangential velocity component is estimated as a function of a volute sizing parameter, SP, defined as:

$$SP = r_4 C_{u4} / (r_5 C_5) \tag{4.52}$$

where C_{u4} and C_5 represent the tangential velocity at the volute inlet and the absolute throat velocity respectively.

The tangential velocity enthalpy loss is given by:

$$\begin{aligned} \Delta h_U &= \frac{1}{2} \frac{r_4 C_{u4}^2}{r_5 C_4^2} \left[1 - \frac{1}{SP^2} \right], \quad SP \geq 1 \\ \Delta h_U &= \frac{r_4 C_{u4}^2}{r_5 C_4^2} \left[1 - \frac{1}{SP} \right]^2, \quad SP < 1 \end{aligned} \tag{4.53}$$

Figure 4.1 shows the iterative procedure followed to estimate the compressor performance at different impeller rotational speeds. The iteration starts by collecting input geometric and thermodynamic data. The initial value of flow density at the impeller tip is assumed and then updated after the 1-D code calculates the impeller's losses, resulting in a new estimate of density. Once density convergence has been achieved, the 1-D code calculates the diffuser and volute losses and estimates the compressor stage efficiency and pressure ratio values.

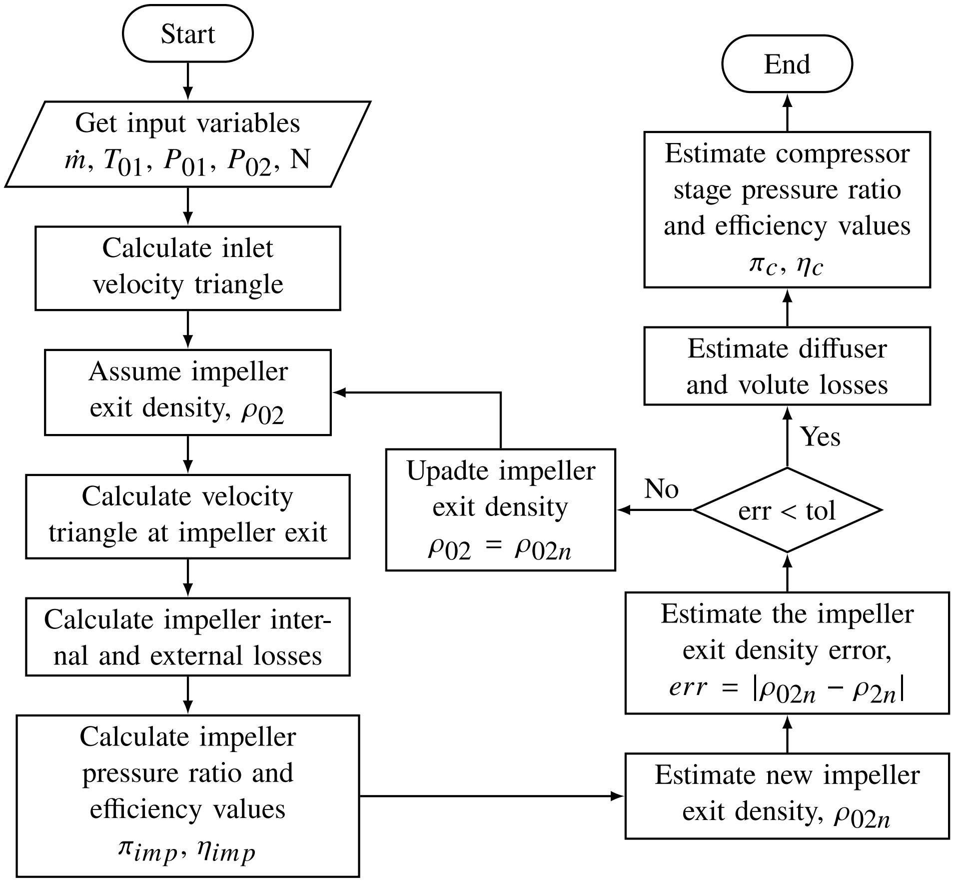

Figure 4.1: Procedure to estimate the compressor performance parameters and loss contributions

The 1-D code used three different loss model combinations to estimate the compressor's performance at each impeller rotational speed. The loss model combinations tabulated in Table 4.1 include the Oh method and a newly developed loss combination method. Figures 1 - 3 show the estimated pressure ratio and efficiency values for the Eckart B compressor and the experimental data.

Table 4.1: The Oh and the newly formulated loss model combinations for 1-D estimation of a compressor stage performance

Losses	Oh loss combination	New loss combination
Slip factor	Wiesner	Aungier
Incidence	Conard et al.	Aungier
Blade loading	Coppage et al.	Coppage et al.
Skin friction	Jansen	Aungier
Mixing	Johnston and Dean	Aungier
Clearance	Jansen	Jansen
Disc friction	Daily and Nece	Daily and Nece
Recirculation	Oh et al.	Oh et al.
Choke	-	Aungier
Vaneless diffuser loss	Stanitz	Stanitz
Volute loss	-	Aungier

The results revealed that the 1-D compressor performance estimation worked well for the pressure ratio estimation in both Oh and the newly formulated loss combination methods. On the other hand, the isentropic efficiency value can be more accurately predicted by the suggested new loss combination model than by the Oh loss combination. The Oh method doesn't consider the volute losses, and it is highly dependent on the accurate estimation of the wake to jet ratio while predicting the mixing loss.

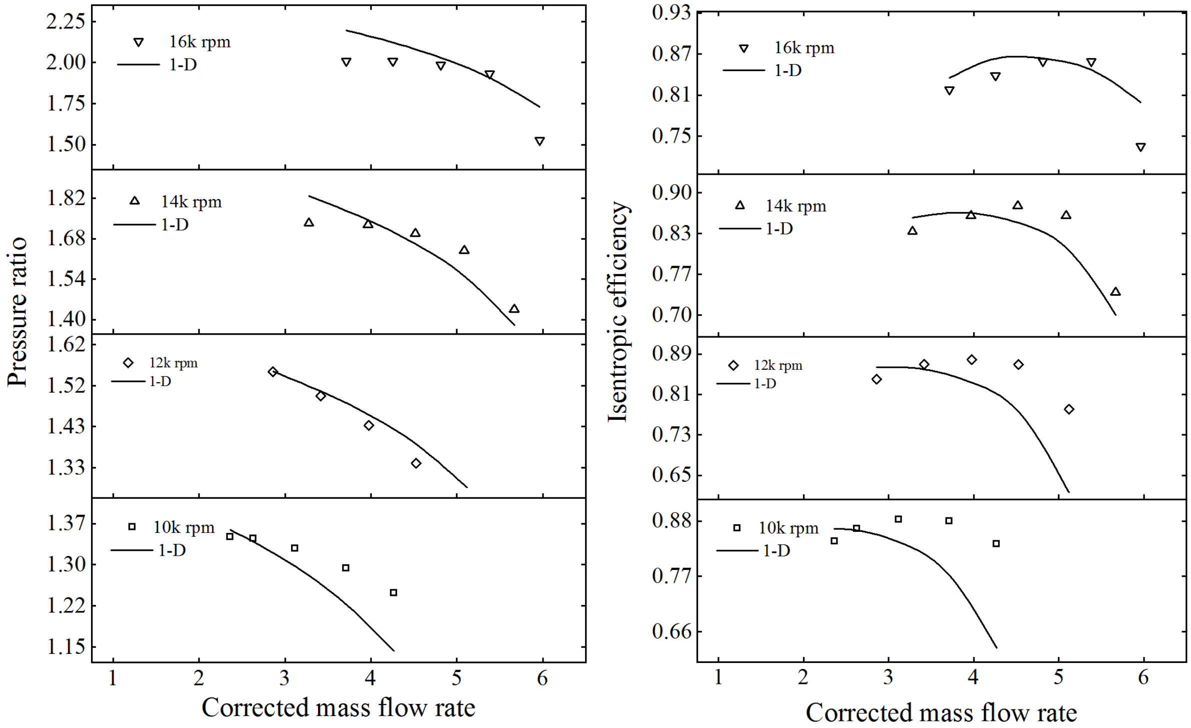

(a)

(b)

Figure 4.2: Experimental and the estimates from Oh 1-D loss model for the pressure ratio (a) and the isentropic efficiency (b) for the Eckart B compressor

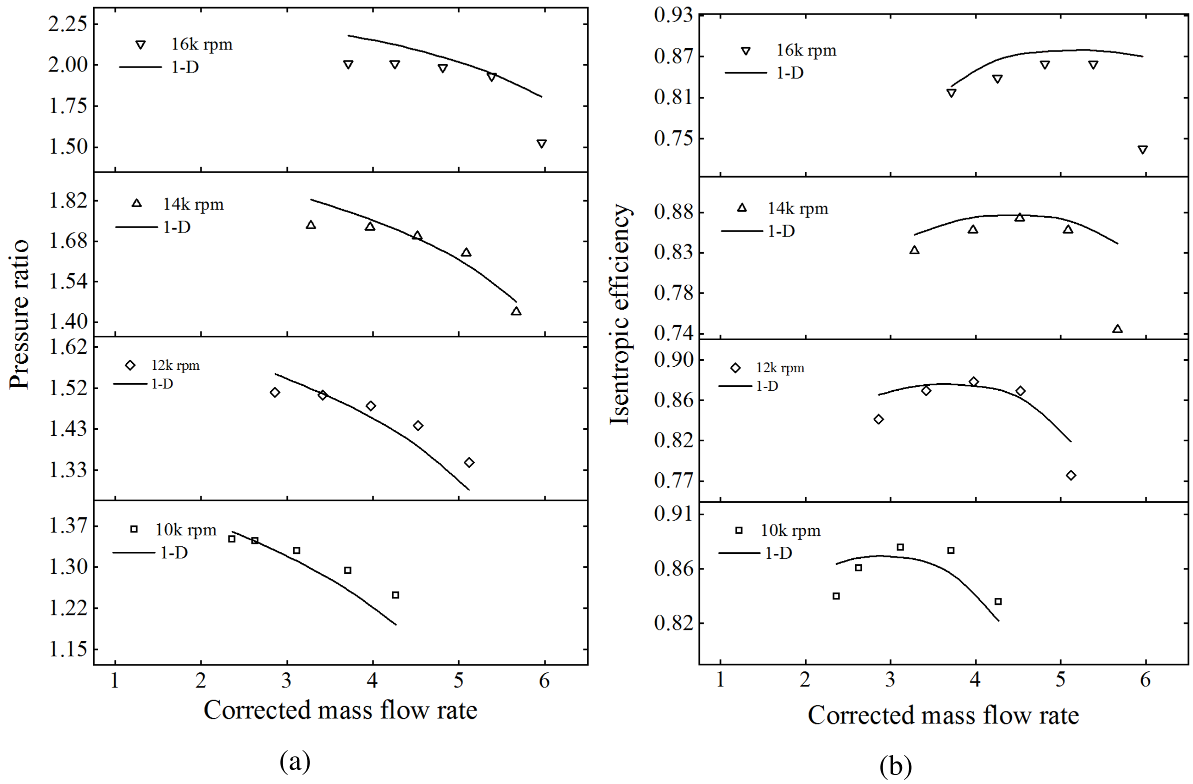

Figure 4.3: Experimental and the estimates from newly formulated 1-D loss model for the pressure ratio (a) and the isentropic efficiency (b) for the Eckart B compressor

Similarly, the 1-D code is used to predict the performance of the turbocharger compressor, whose dimensions are discussed in section 4.2. The 1-D estimates are compared with the CFD results, as shown in Figure 4.4. The results show that the 1-D code underestimates the compressor pressure ratio and isentropic efficiency values at lower impeller rotational speeds. On the other hand, at higher impeller rotational speeds, the 1-D overpredicts the compressor performance. When the rotational speed of the impeller is increased, the near choke performance prediction becomes less accurate. The performance prediction seems to be most accurate at 80k impeller rotational speed.

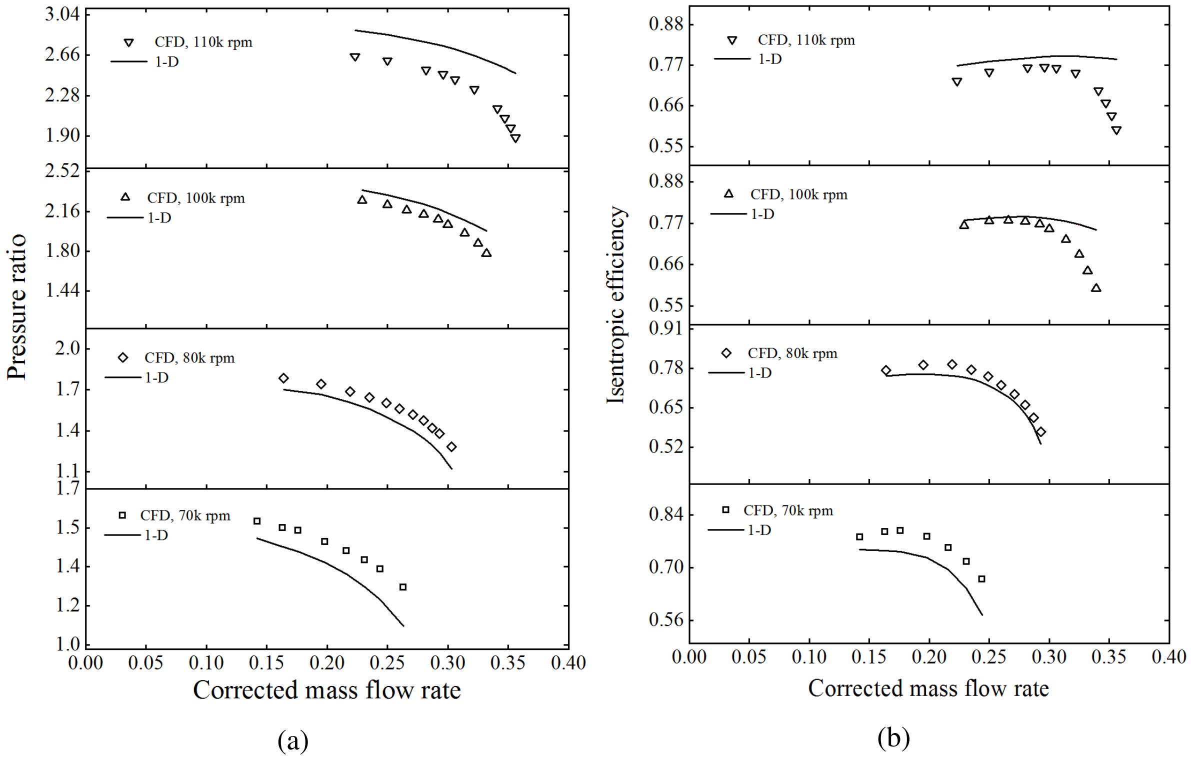

Figure 4.4: CFD and 1-D loss model estimates for the pressure ratio (a) and the isentropic efficiency (b) for the turbocharger compressor

4.2 Extracting Centrifugal Impeller Geometry Details from 3-D CAD Models

The performance of a centrifugal compressor is estimated using one-dimensional codes or using commercial numerical solvers (such as ANSYS, STAR CCM+ or OpenFOAM). Most of the time one-dimensional performance estimation is used in the preliminary design stage of a compressor while optimization of a compressor performance is mostly done in commercial numerical solvers before full-scale laboratory experimental result verification.

One dimensional performance estimating codes highly depend on detailed blade geometrical design data. Usually, the compressor and turbine impeller geometries from research sponsoring companies are provided in three-dimensional cad formats with additional hub and shroud curves data. A suitable CAD software should be used to extract the blade geometries at different-span sections from the hub to the tip of the blades. The extracted blade curves are three-dimensional and require further coordinate transformations to convert space points in a three-dimensional Cartesian coordinate to a two-dimensional m-rθ coordinate system to obtain the blade geometry details.

4.2.1 Coordinate Transformation

The blade curve in cylindrical three-dimensional coordinate system definition can be transformed to a two-dimensional curve by defining the meridional stream curve in terms of radius and cylindrical axis coordinate (z) values. The differential arc length *dm* is defined as:

$$dm = \sqrt{(dr)^2 + (dz)^2} \tag{4.54}$$

Figure 4.5 shows the m-direction($r\theta$) on the stream surface.

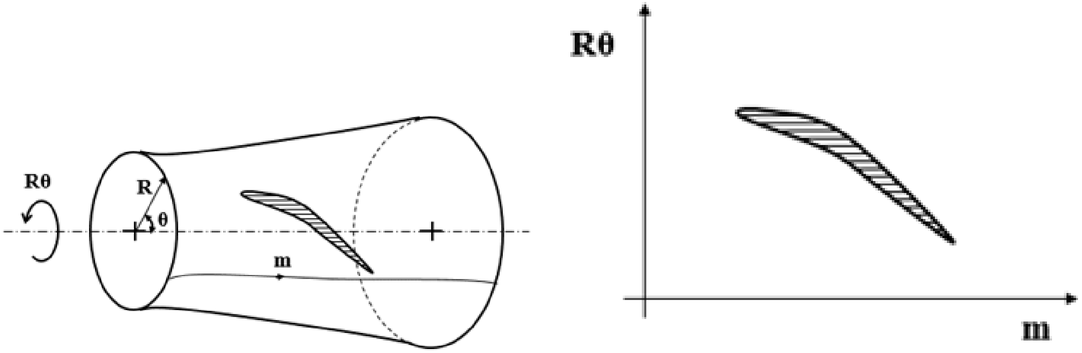

(a) (b)

Figure 4.5: Stream Surface m and $r\theta$ directions

The $m - r\theta$ stream coordinate system is length preserving. For angle measurements, the $m' - \theta$ coordinate is more appropriate. The $m' - \theta$ coordinate system is defined by normalizing the m and $r\theta$ values by the radius. The normalized arc length is defined by,

$$m' = \int \frac{dm}{r} = \int \frac{\sqrt{(dr)^2 + (dz)^2}}{r} \tag{4.55}$$

For general non-analytical blade sections, numerical integration is employed to solve eq.(4.55). Simple trapezoidal integration gives an acceptable approximation of the integral for reasonably dense blade curves data points as defined in eq.(4.56).

$$m'_i = m'_{i-1} + \frac{2}{r_i + r_{i-1}} \sqrt{(r_i - r_{i-1})^2 + (z_i - z_{i-1})^2} \tag{4.56}$$

The meridional coordinate m and m' values for each point on the blade curves are interpolated from the fluid zone m values at given radius and z values. The inlet to the fluid zone is marked as the start of the meridional curve with zero value of m. Each combination of r and z will give a unique of m. The meridional curve m values for each blade curve data point is interpolated from the fluid zone curve m values using a unique angle β, defined from the inlet to exit of the fluid zone curve. Angle β is defined from average radius and z values to the points on the fluid zone curve as shown in Figure 4.5.

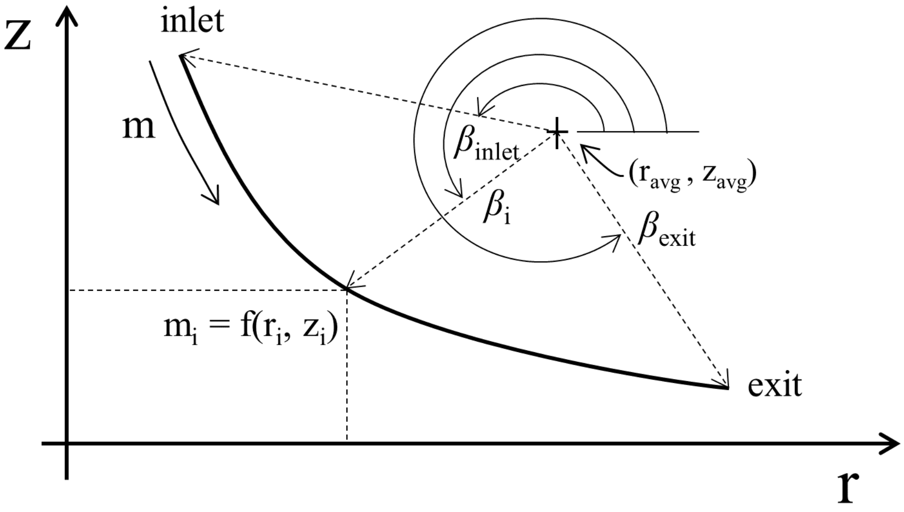

Figure 4.6: Angle β definition for the blade streamline

Angle β at any point on the fluid zone curve is defined as:

$$\beta_i = \tan^{-1}\left(\frac{z_i - z_{avg}}{r_i - r_{avg}}\right) \tag{4.57}$$

For a given value of Z_i and r_i on the blade curve, β_i is calculated using eq.(4.57). The calculated β_i is used to interpolate m value from the fluid-zone curve data. The $m - r\theta$ and $m' - \theta$ plots are done for five blade cross-sections, including the hub and shroud sections as shown in Figure 4.7.

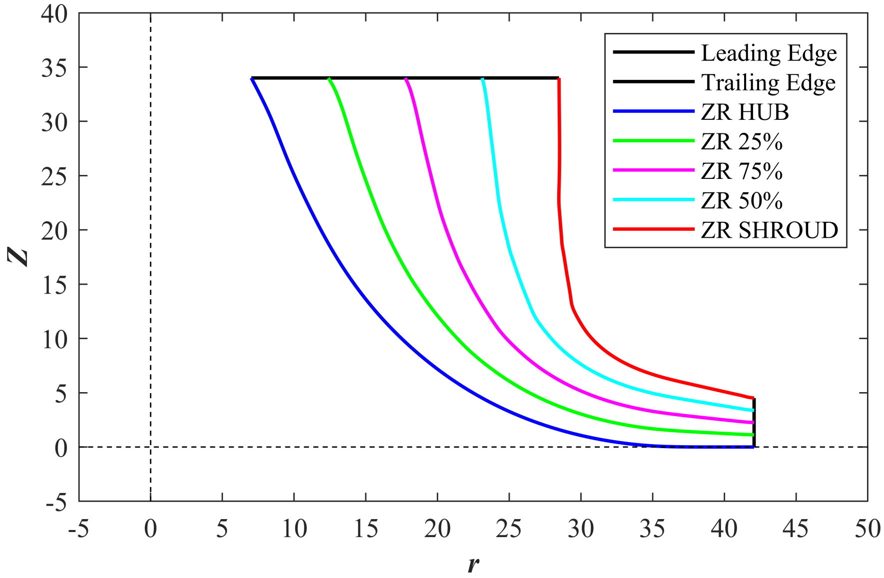

Figure 4.7: Meridional Plane Streamline curves from Hub to Shroud

A MATLAB code is written to convert the three-dimensional blade curves from cylindrical coordinate to the two-dimensional meridional plots as shown in Figure 4.8.

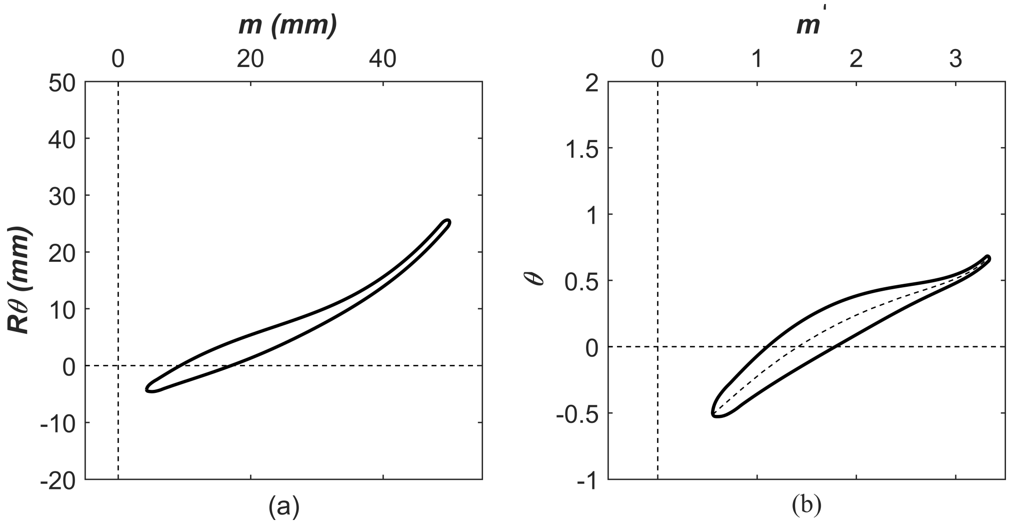

(a)

(b)

Figure 4.8: (a) $m - r\theta$ and (b) $m' - \theta$ plot for the main blade at the hub cross-section

The blade thickness distribution normal to camber line is interpolated from the $m - r\theta$ curve for all five blade cross-sections considered. All blade angles are defined from $m' - \theta$ curve of the camber line. To find the blade camber line, the blade curves are fitted to Béziers curves. Bézier curves are expressed in terms of Bernstein polynomials as shown in eq.(4.58) for a curve parameter $t \in (0, 1)$ [59].

$$b^n(t) = \sum_{i=0}^{r} b_i^{n-r}(t) B_i^r(t) \tag{4.58}$$

where: b_i^{n-r} – Bézier curve control points

$B_i^r(t)$ - Bernstein polynomial of degree r defined in eq.(4.59) defined as:

$$B_i^r(t) = \binom{n}{i} t^i (1-t)^{n-i} \tag{4.59}$$

where the binomial coefficients are defined in eq.(4.60),

$$\binom{n}{i} = \begin{cases} \frac{n!}{i!(n-i)!} & if \quad 0 \leq i \leq n \\ 0 & else \end{cases} \tag{4.60}$$

A rolling ball is fitted between the two curves of a given blade profile. The center locus of the rolling balls gives the camber line. The balls should be tangent to the two curves Bézier curves. The first derivative of the Bézier curve, eq.(4.61), gives the tangent line at all points used to find the camber line.

$$\frac{d}{dt} b^n(t) = n \sum_{i=0}^{n-1} (b_{i+1} - b_i) B_i^{n-1}(t) \tag{4.61}$$

The number of circles used to fit the camber line depends on the curve point resolution of the blade profile under consideration and the tolerance of the fit. The two curves for each blade profile are divided into $(1-5) \times 10^3$ points for improved resolution. The rolling ball algorithm is set up to have a tolerance of 10^{-3}. The algorithm can fit circles to a length 0.1% off of the first curve from both leading and trailing edge sides. Figure 4.9 shows the tangent circles fitted on the hub section profile of the main blade.

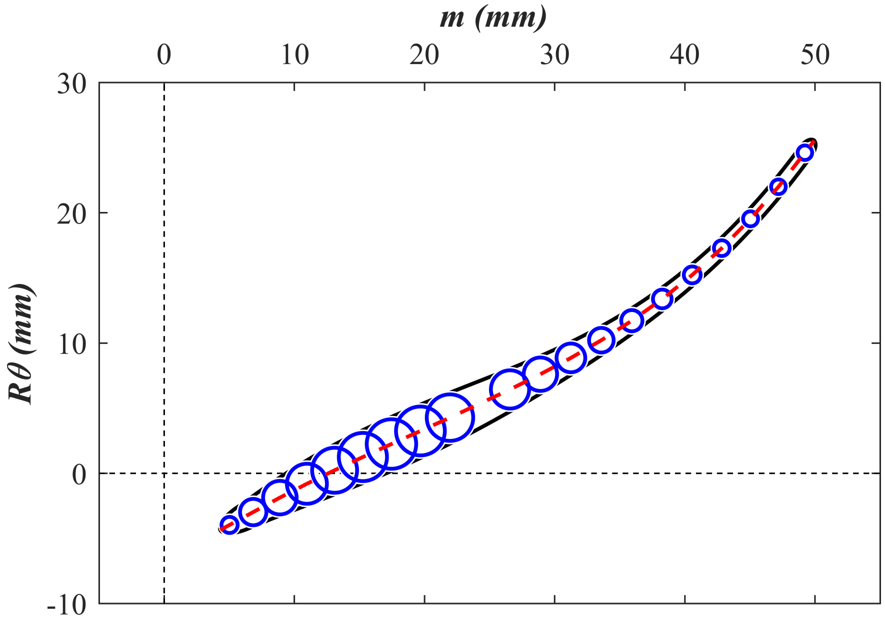

Figure 4.9: Tangent Circles fitted between two curves of the hub section profile of the main blade

The camber line algorithm uses cubic Bézier fit for the second curve to find the center coordinate positions of the tangent circles in the $m - r\theta$ plane. Each Bézier fit of the second curve is further subdivided into $10^3 - 10^4$ points for tangent circle fit tolerance fall in the set limit.

Three methods are used to find the leading and trailing edges of each blade profile. In the first method, two Bézier fits for each blade profile, either of them containing leading edge or the trailing edge, ensuring tangency and continuity of the fits at all breakpoints used. The curvature of a parametric curve is given by [60],

$$k(t) = \frac{|r' \times r''|}{|r'|^3} \tag{4.62}$$

where: $r = [x(t), y(t)]$ in two-dimensional space. Substitution for r in eq.(4.62) gives:

$$k(t) = \frac{|x'y'' - x''y'|}{|x'^2 - y'^2|^{3/2}} \tag{4.63}$$

The location of maximum curvature of the two Bézier fits give leading and trailing edge $m - r\theta$ coordinate values.

The second method involves fitting points near the leading and trailing edges as an ellipse. The intersection between the axes of the fitted ellipses and the blade profile curves gives the leading and trailing edge coordinate values. A general second-degree polynomial equation for conic sections in implicit form is given by,

$$f(x, y) = ax^2 + bxy + cy^2 + dx + ey + f = 0 \tag{4.64}$$

An ellipse should satisfy a constraint defined by,

$$b^2 - 4ac < 0 \tag{4.65}$$

where, a, b, c, d, e, f are coefficients of the ellipse. A least square method is used for the numerical fit of the ellipses at both ends of the blade profiles [61].

The third method considered uses the first two tangent circle fit centers to formulate a linear line near the leading edge. The intersection between the new linear line and the blade profile curve gives the approximate position of the leading edge. The same approach is applied to find the trailing edge by using the last two tangent circle fit centers of the camber line.

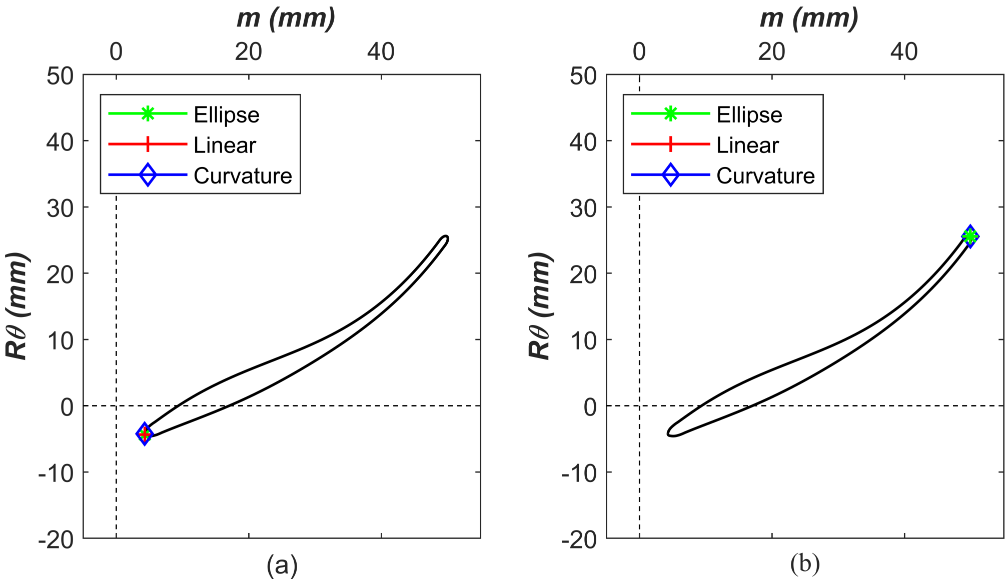

(a) (b)

Figure 4.10: (a) Leading edge (b) Trailing edge estimation using three methods for the hub blade profile of the compressor

All the three methods used to estimate leading and trailing edges gave close estimates. The adjusted curves for the hub blade profile of the compressor using the new values of the leading and trailing edges are shown in Figure 4.11

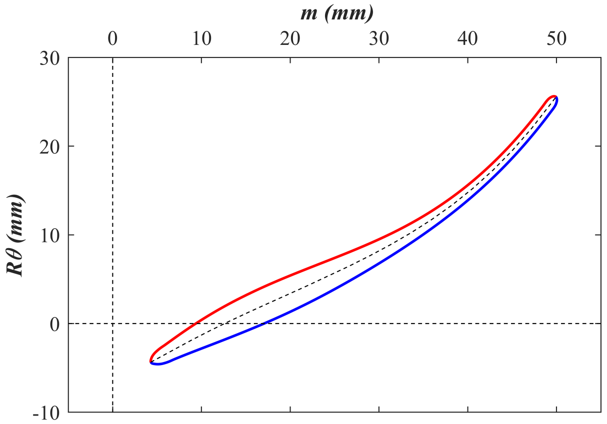

Figure 4.11: Adjusted Hub blade profile of the compressor

The inlet and exit blade angles from the meridional axis along with stagger angle are defined in angle preserving $m' - \theta$ space of the camber line as shown in Figure 4.12.

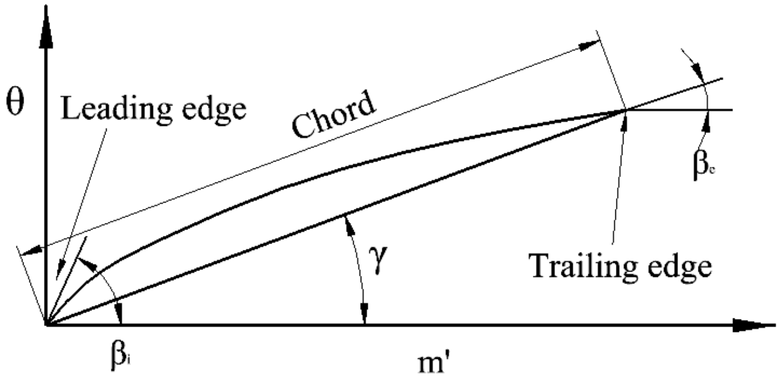

Figure 4.12: Mean Camber definition adapted from [62]

The blade angle, β is defined by Eq.(4.66),

$$tan(\beta) = \frac{rd\theta}{dm} = \frac{d\theta}{dm/r} = \frac{d\theta}{dm'} \tag{4.66}$$

4.3 Steady-state Compressor Performance Analysis

4.3.1 CFD Setup

The Reynolds averaged Navier-Stokes (RANS) steady-state equations are used to evaluate the compressor performance at various impeller speeds. All y+ resolution model of the CFD commercial software StarCCM+ [28] is used with an expansion factor of 1.3 and a total prism thickness of 0.15 mm. Three CFD meshes, each composed of approximately twenty-one million polyhedral and prism elements, are used to analyze the steady-state compressor performance. The three configurations correspond to choke channel being closed, opened, and to a base compressor with no case treatment, as shown in Fig. 4.13. To acquire a higher degree mesh density isotropy with smoother mesh size transitions, polyhedral mesh elements are preferred than trimmed cell element [28].

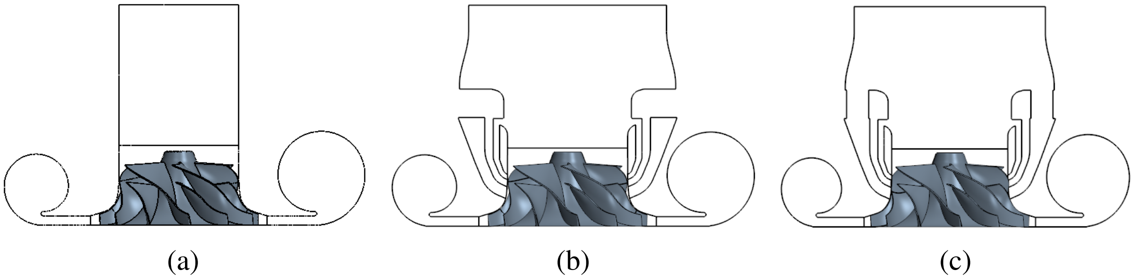
(a) (b) (c)

Figure 4.13: Computation models used for steady-state performance analysis for the (a) base compressor with no casing treatment, (b) when choke channel is closed, and (c) when choke channel is opened [63].

The compressor performance analysis applies a stagnation pressure inlet and a static pressure outlet boundary condition for mid to high mass flow rate values. For operating points from the peak efficiency to the surge point, the outlet boundary condition is changed to the mass flow rate targeting specific points on the compressor speed line. A double-precision version of StarCCM+ with the segregated flow solver is chosen over the coupled flow solver for faster convergence.

The compressor wheel for the study consists of 6 full blades and 6 splitter blades. The mesh used for steady-state performance uses all y+ treatment with a $y+ \approx 1$ targeted. The effect of y+ on the accuracy of steady-state performance estimation is studied for impeller running at 70k rpm with choke slot closed configuration, as shown in Fig. 4.14. As shown in the figure, high y+ ($30 < y+ < 80$) wall treatment gave relatively lower accuracy for both pressure ratio and efficiency plots. The low y+ wall treatment model gave values that match the test results closely [19].

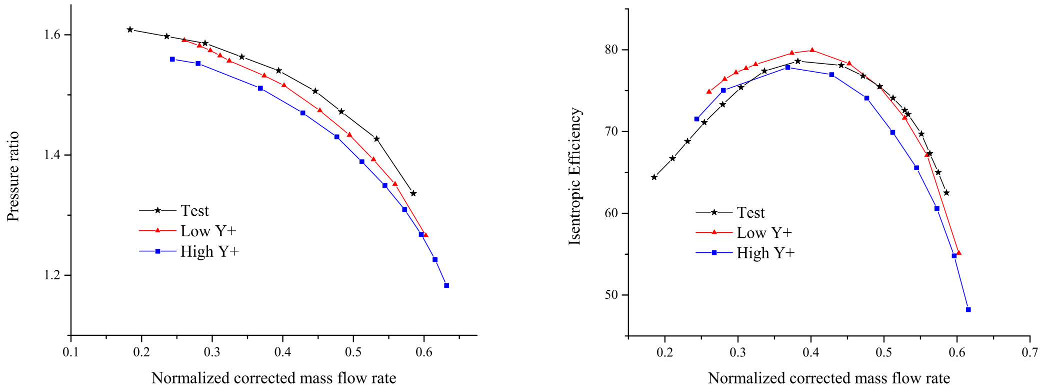

(a) (b)

Figure 4.14: Compressor performance running at 70k impeller rotational speed with choke slot closed configuration for low and high y+ wall treatment cases

In total, 292 steady-state runs are computed to get the full compressor map for the three compressor mesh settings. The pressure ratio versus mass flow rate of the three models is plotted in Figure 4.15a. As shown in the figure, compared to the base mesh, the choke slot open configuration modifies the choke limit by about 11% at the highest impeller rotational speed employed for the simulation. The open choke slot also increases the choke margin by approximately 10% in comparison with the choke closed operation.

With an increase in the impeller rotational speed, the near surge pressure ratio is improved with a significant map width. The exact quantification on the surge improvement of the casing treatments is not covered here as the analysis needs an extensive unsteady study at various rotational speeds of the impeller. Figure 4.15b shows that the mass flow rate values at the maximum efficiency point of the speed lines of the two CFD schemes with casing treatment are shifted to the surge point. This reveals the benefit of the casing treatments in providing stable operating points close to the surge limit.

At lower impeller speeds, no considerable pressure ratio gain or map width enhancement is observed with both choke slot closed and open configurations. A marginal increase in pressure ratio of the choke slot configuration over the choke slot open is observed with a rise in the compressor running speed. Both the choke slot closed and open arrangements gave a lesser maximum pressure ratio and efficiency values in comparison with the base compressor. In contrast with the base compressor, both the choke closed and open configuration provided better near surge performance.

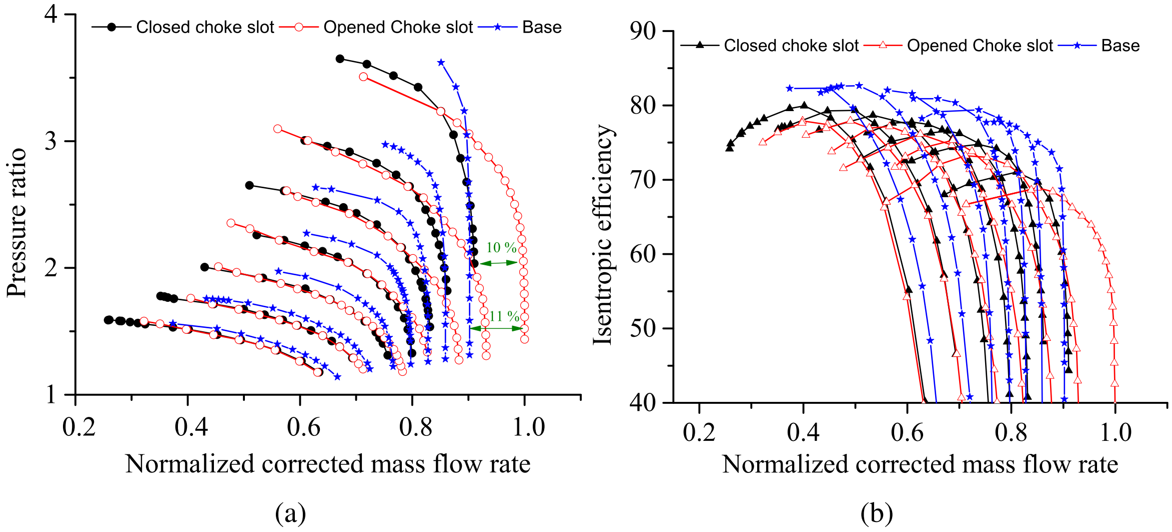

Figure 4.15: Compressor performance steady-state results for all three CFD configurations: (a) pressure ratio vs. normalized mass flow rate, and (b) isentropic efficiency vs. normalized mass flow rate.

The efficiency versus normalized mass flow rate for the three configurations is plotted in Fig. 4.15b. From the figure, it can be seen that for all impeller rotational speeds, the base compressor without any casing treatment gives the highest efficiency value. In comparison with choke slot open configuration, choke slot closed configuration gives higher efficiency values as the operating point moves closer to the surge point. The narrow working range of the base compressor is also noticeable from Figure 4.15b, with the CFD simulation unstable at relatively higher efficiency values.

4.4 Compressor Performance Map Modeling

Modeling turbocharger compressor performance is beneficial for many reasons. Following a compressor design, the model's predictions are valuable for estimating compressor performance before manufacturing and testing procedures. The testing of compressor performance is limited to a few impeller rotational speeds and mass flow rates since testing the entire range of operating points is impractical and expensive. Furthermore, an accurate turbocharger performance model can reduce the time and expense needed for testing during engine development.

4.4.1 Compressor Pressure Ratio

Jensen et al. [64] presented a model to predict the compressor pressure ratio and isentropic efficiency values using three non-dimensional numbers: the head coefficient, flow coefficient, and Mach number. The head coefficient of the compressor is defined as:

$$\psi = \frac{c_p T_{01}\left[\Pi_c^{\frac{\gamma-1}{\gamma}} - 1\right]}{\frac{1}{2}U_2^2} \tag{4.67}$$

The flow coefficient is defined as:

$$\phi = \frac{\dot{m}}{\rho_{01}\pi r_2^2 U_2} \tag{4.68}$$

where U_2 is the blade tip speed calculated by:

$$U_2 = \frac{\pi d_2 N}{60} \tag{4.69}$$

The Jensen & Kristensen model uses an invertible relation between the head and flow coefficients using three constants. Each of the three constants depends linearly on the Mach number of the flow. The model is defined as:

$$\psi = \frac{C_1 + C_2\phi}{C_3 - \phi}, \quad C_i = C_{i1} + C_{i2}M, \quad i = 1, 2, 3 \tag{4.70}$$

The model parameters c_1, c_2, and c_3, are determined by a statistical fitting of the manufacturer's experimental data. The inlet Mach number, M, is defined as the ratio of the impeller tip speed and the sonic velocity of the flow at the compressor inlet:

$$M = \frac{U_2}{\sqrt{\gamma R T_{01}}} \tag{4.71}$$

In interpolation and extrapolation of the compressor map at a given impeller rotational speed, the head and flow coefficient definitions in Eq.(4.67) and Eq.(4.68) are used to predict the pressure ratio and mass flow rate values. Jensen et al. stated that their model predicted the pressure ratio values with ±1% accuracy for most impeller speeds. Their model's prediction accuracy diminished as impeller rotation speeds increased due to increasing Mach numbers in inlet flow.

Jensen et al. used a second-degree polynomial equation of the flow coefficient to estimate the compressor efficiency. The coefficients of the polynomial equations are derived from three other coefficients and the flow inlet Mach number.

$$\eta = a_1\phi^2 + a_2\phi + a_3, \quad a_i = \frac{a_{i1} + a_{i2}M}{a_{i3} - M}, \quad i = 1, 2, 3 \tag{4.72}$$

Jansen et al. reported that their efficiency model predicted a result within ±3% of the manufacturer's experimental data.

The fit of head coefficient against the flow coefficient for all compressor speeds using the Hadef and Jansen's model is shown in Figure 4.16. From the plots it can be seen that the model by Jansen and Hadef give very close fit of head coefficient against flow coefficient.

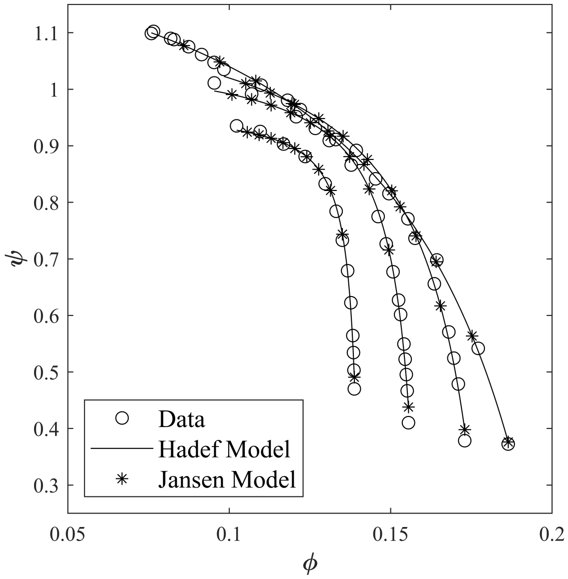

Figure 4.16: Flow Coefficient vs Head Coefficient for all impeller rotational speeds from the (Experimental or CFD) compressor map

The C_1, C_2, and C_3 values are unchanged for all ψ and ϕ values at given impeller rotational speed. The variation of this three constants against the turbocharger rotational speed can expressed by second order polynomial fits as [65]:

$$C_i = C_{i,1} * {\omega_t}^2 + C_{i,2} * \omega_t + C_{i,3} \tag{4.73}$$

As shown in Figure 4.17, C_1, C_2, and C_3 values are well approximated by second order polynomial fits. Since the c_i values can be interpolated at a given ω_t, extrapolation and interpolation of ψ and ϕ values is possible at a rotational speed of interest.

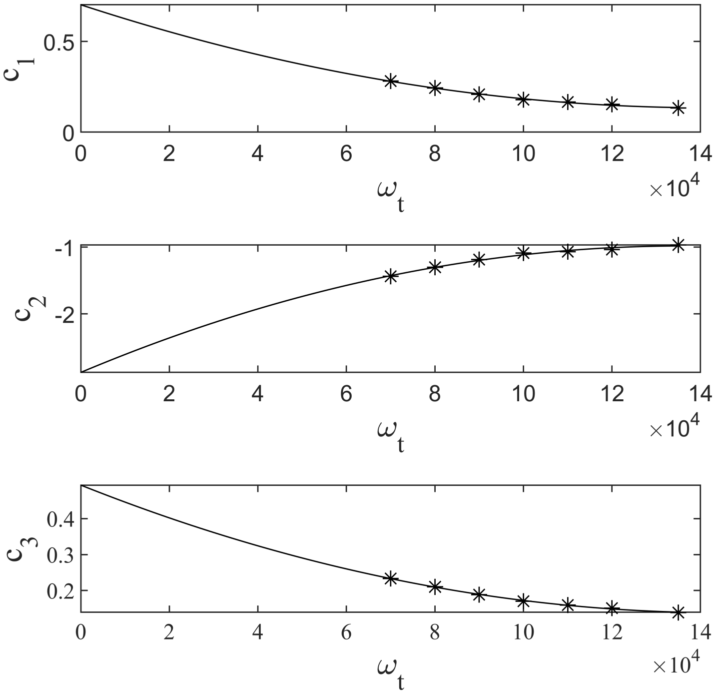

Figure 4.17: Second order fits of C_1, C_2, and C_3 values plotted against turbocharger rotational speed, ω_t

Using Eq.(4.67) and Eq.(4.68) the pressure ratio and the corrected mass flow rate can be estimated from the known ψ and ϕ values for a given turbocharger rotational speed as shown in Figure 4.18. It can seen from Figure 4.18 that the predicted values confirm with the compressor map values especially at lower turbocharger rotational speeds. Where as at middle rotational speeds, the accuracy of the fit decreases near lower mass flow rate values.

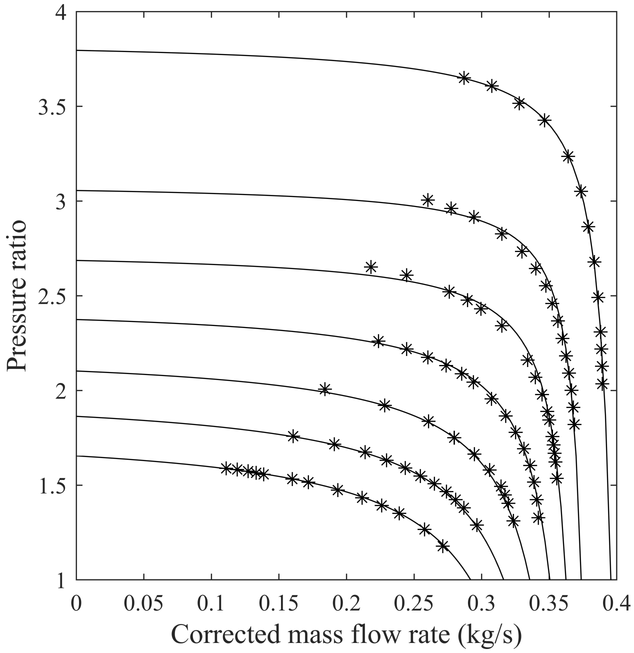

Figure 4.18: Predicted (—) vs compressor map ($*$) pressure ratio values at various impeller rotational speeds

4.4.2 Surge Modeling

The compressor performance prediction method incorporated the surge model developed by Moore-Greitzer [66]. The unstable part of the compressor characteristics curve to the left of the maximum pressure point of a given turbocharger speed line can be estimated using a third order polynomial equation [67]:

$$pr = pr_o + \beta \left[1 + 1.5 \left(\frac{\dot{m}_c}{\phi} - 1 \right) - 0.5 \left(\frac{\dot{m}_c}{\phi} - 1 \right)^3 \right] \tag{4.74}$$

where pr_o is the pressure ratio at zero flow, β, and ϕ are parameters identified in Figure 4.19 and $\dot{m}_c$ is the compressor corrected mass flow rate.

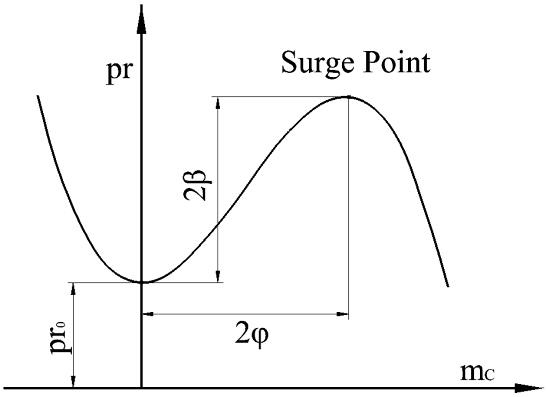

Figure 4.19: Compressor characteristic parameters adapted from Reference [67]

To the left the maximum pressure point of each speed line, the slope of pressure ratio vs mass flow rate is positive, while in the stable zone, where the compressor is expected to operate, the slope is negative. At maximum pressure point of a given compressor speed line the slope is zero. During interpolation and extrapolation of the compressor map at different speed lines, the zero-slope line is predicted using a third-order polynomial fit of the maximum pressure points of the compressor map as shown in Figure 4.20. The origin is included in the polynomial fit so that a unique zero-slope line point is evaluated at each speed line.

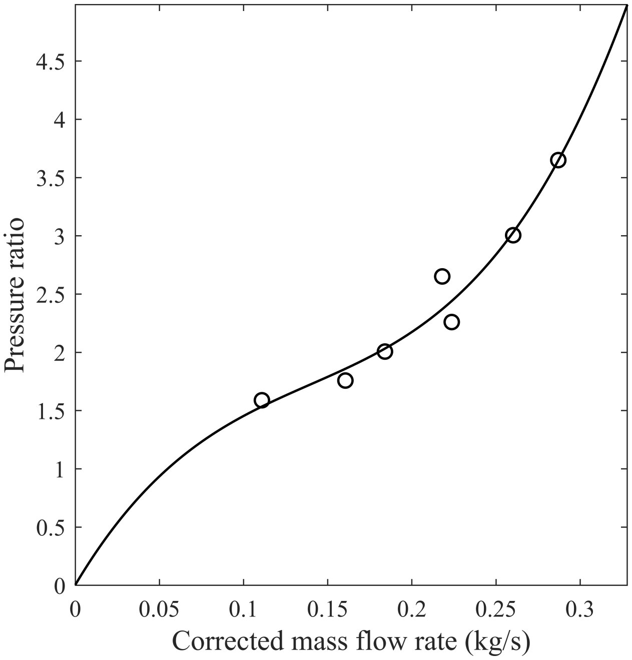

Figure 4.20: Polynomial fit (—) of the compressor map zero-slope line points (○)

The final predicted compressor map that includes the surge model is shown in Figure 4.21.

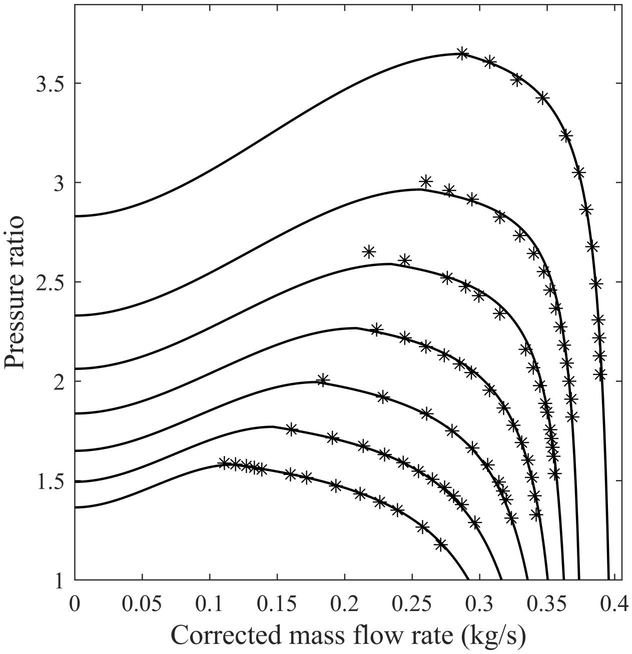

Figure 4.21: Predicted (—) vs compressor map (∗) pressure ratio values at various impeller rotational speeds including the surge model

4.4.3 Compressor Efficiency

The isentropic efficiency of a turbocharger compressor is defined as a ratio of specific enthalpy (Δh) and isentropic enthalpy (Δh_{is}) between the inlet and exit of the compressor.

$$\eta_{comp} = \frac{\Delta h_{is}}{\Delta h} \tag{4.75}$$

The isentropic enthalpy change across the turbocharger compressor can be equated from the pressure ratio between the inlet and exit of the compressor as:

$$\Delta h_{is} = c_p T_{0,1} \left[\Pi_c^{\frac{\gamma-1}{\gamma}} - 1 \right] \tag{4.76}$$

The actual enthalpy change across the compressor can be equated from Euler's equation using velocity triangle values at inlet and exit of the compressor impeller as defined by Eq.(4.1). Considering most turbocharger compressors are designed without inlet swirl [12], the tangential component of the absolute velocity at inlet will have zero value ($C_{u1} = 0$).Using the slip factor, σ, and velocity triangle relations at the exit, the actual total enthalpy rise across the compressor is equated as:

$$\Delta h = \sigma U_2^2 \left(1 - \phi_2 \tan(\beta_{2b})\right) \tag{4.77}$$

where β_{2b} is the exit blade angle of the impeller vanes, and ϕ_2 is the flow coefficient at impeller exit equated as:

$$\phi_2 = \frac{C_{m2}}{U_2} = \frac{\dot{m}_c}{\rho_2 U_2 A_2} \tag{4.78}$$

where ρ_2 is the compressor impeller exit air density and A_2 is the compressor exit area. Air density at the exit of the compressor varies considerably for each speed line of the turbocharger compressor map. The density also increases as the operating point moves to the maximum pressure point of a given speed line. Substituting flow coefficient in equation (4.77) gives Eq.(4.4).

From Eq.(4.4), the actual enthalpy across the impeller can be related to mass flow rate linearly as stated in Eq.(4.79):

$$\Delta h = x_1 - x_2 * \dot{m}_c \tag{4.79}$$

where x_1 and x_2 are determined from the linear fit of the total enthalpy change of the compressor map data as shown in Figure 4.22. The linear fit error is minimal near design rotational speed of the turbocharger (second fit line from bottom). Below the design rotational speed, the fit errors are higher near surge operating points whereas beyond the design rotational speed, the fit errors are higher near choke operating points.

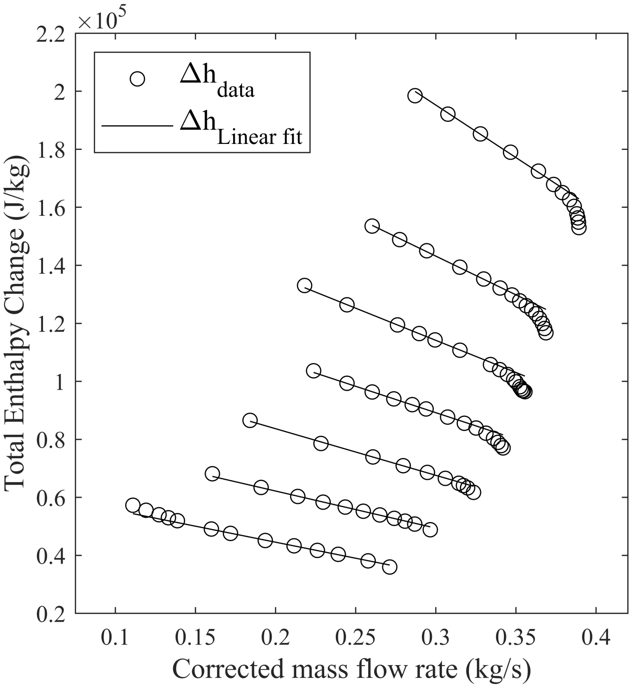

Figure 4.22: Linear fit of the total enthalpy change of the compressor map data

The dependency of x_1 and x_2 on turbocharger rotational speed is shown in Figure 4.23. Extrapolation and interpolation of the compressor efficiency at different turbocharger rotational speeds can be achieved using a second order polynomial fit of x_1 and x_2 with turbocharger rotational speed as:

$$x_i = x_{i,1} * w_t^2 + x_{i,2} * w_t + x_{i,3} \tag{4.80}$$

where $x_{i,1..3}$ are the six second polynomial fit coefficients of x_1 and x_2. The second order polynomial fits x_1 and x_2 are shown in Figure 4.23.

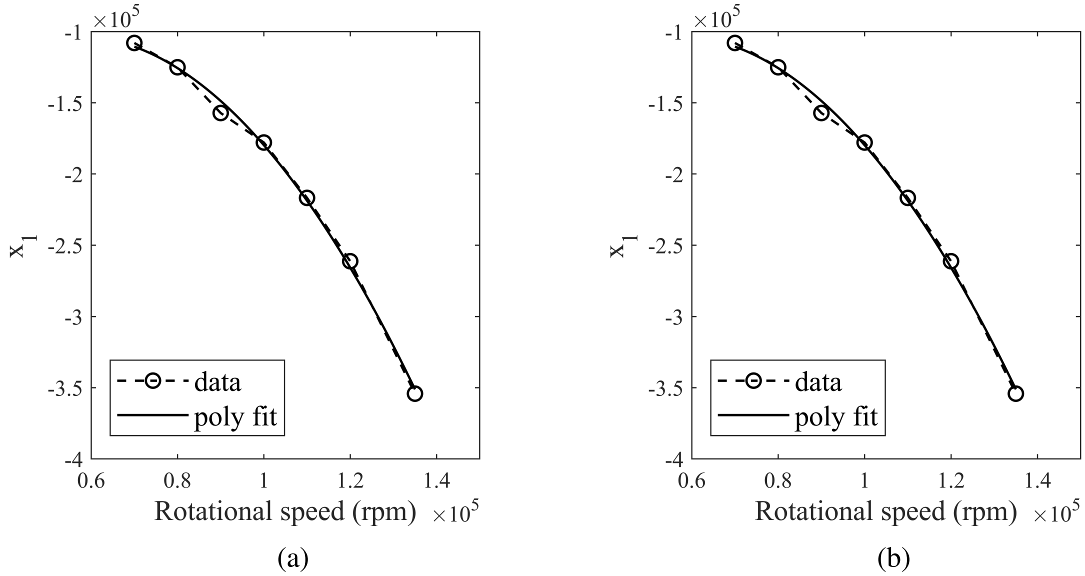

Figure 4.23: Variation of x_1 and x_2 with turbocharger rotational speed

The compressor efficiency model is validated using the compressor map as shown in Figure 4.24. As can be seen form the figure, the model fits the data well on most of operating points at all turbocharger rotational speeds.The model accuracy decreases as it overestimates the compressor efficiency at operating points near the surge points mostly at lower turbocharger rotational speeds.

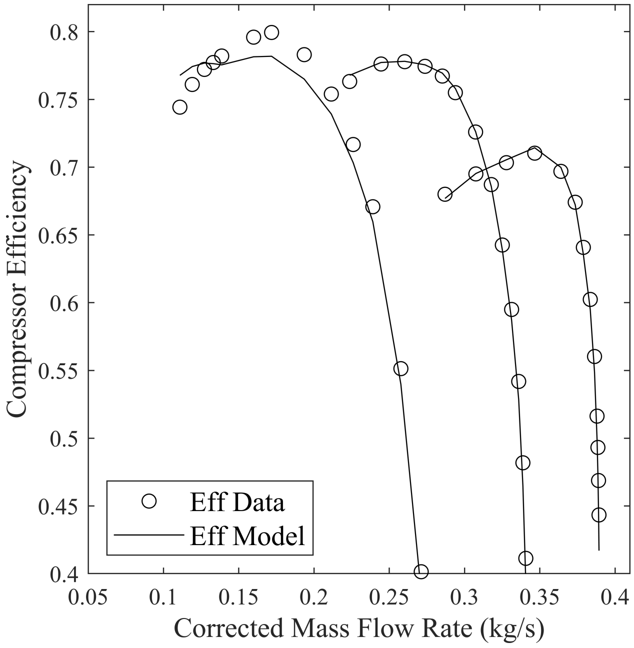

Figure 4.24: Compressor efficiency model validation

The design point of the compressor can be approximated considering that the compressor has maximum efficiency at design point. The efficiency contours plotted in Figure 4.25 show that the maximum efficiency contour can be approximated as an ellipse using least square methods [61] where the center of the ellipse gives design mass flow rate and pressure ratio points.

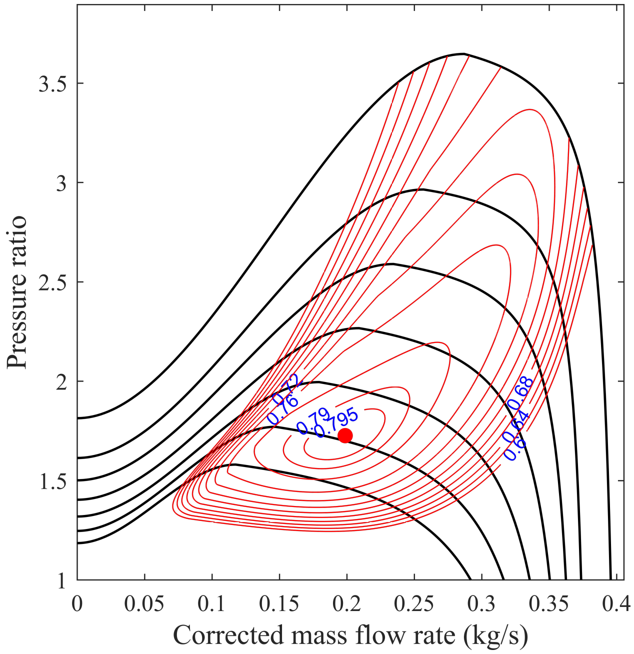

Figure 4.25: Predicted Compressor Map with Efficiency Contours

4.5 Effect of Casing Treatment

The base compressor surge and choke limit performance is enhanced by employing passive and active shroud ports. The passive port, which is open at all compressor operating conditions, increases the surge limit with little efficiency penalty. The active port is only functional when the compressor operating points move closer to the choke limit.

The compressor's near choke performance is impacted by flow separation downstream of the splitter blade's throat. The separated flow region increases as the impeller rotational speed increases as shown in Figure 4.26. This separated flow region has a lower static pressure than the inducer and is preceded by a high relative Mach number, as illustrated in Figure 4.27.

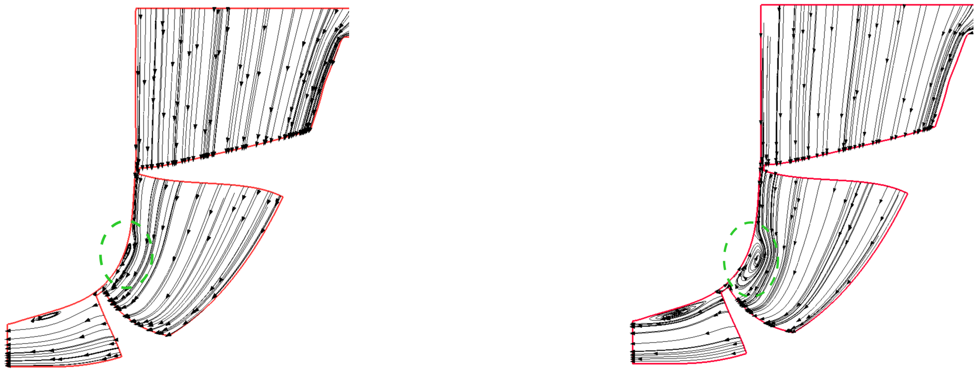
(a) (b)

Figure 4.26: Near choke flow streamline of a base compressor with no casing treatment running at impeller rotation speed of: (a) 80k, (b) 120k.

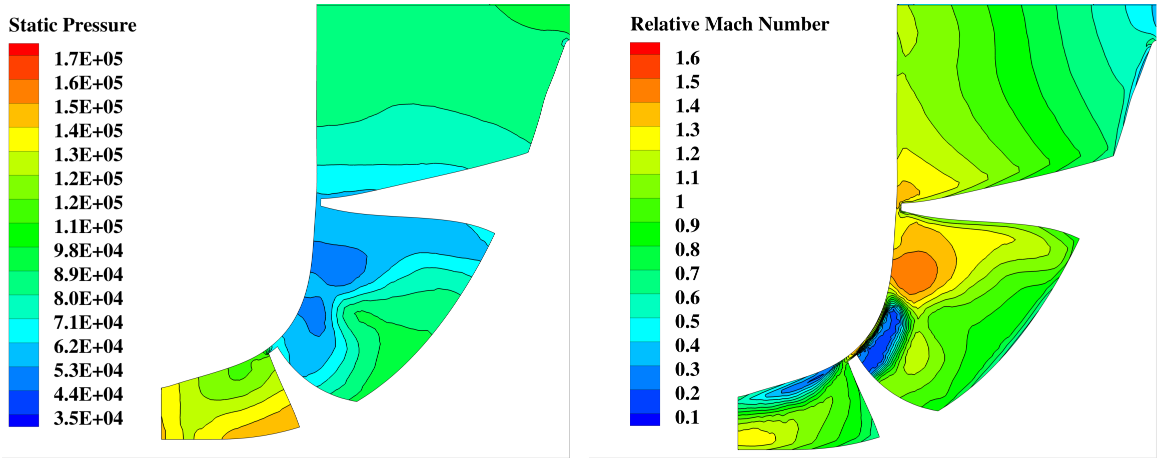

(a) (b)

Figure 4.27: Impeller Static Pressure distribution (a) and impeller relative Mach number distribution (b) for a base compressor operating near choke margin at 120k impeller shaft rotational speed

Usually, the surge slot is positioned near the impeller leading edge as the blade loading is higher near the leading edge at reduced mass flow rates [68]. Figure (4.28) shows the static pressure distribution of the base compressor at near surge operating conditions.

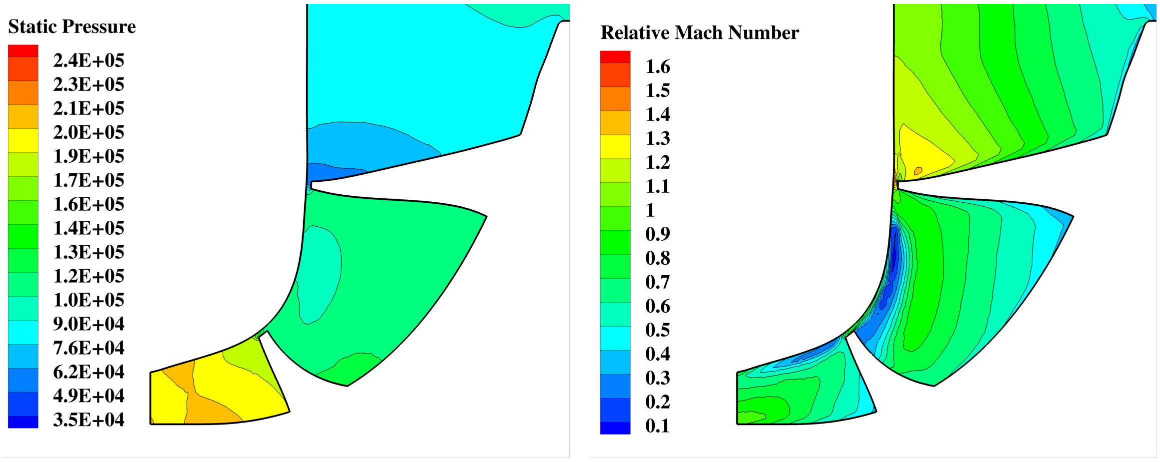

(a) (b)

Figure 4.28: Impeller Static Pressure distribution (a) and impeller relative Mach number distribution (b) for a base compressor operating near surge margin at 120k impeller shaft rotational speed

A larger surge port width increases the recirculation mass flow from the shroud to the inlet near surge operating conditions. On the contrary smaller port width reduces the peak efficiency penalty induced by the addition of the surge port. Consequently, the final surge port width should be set iteratively by considering the peak efficiency penalty and the surge margin improvement.

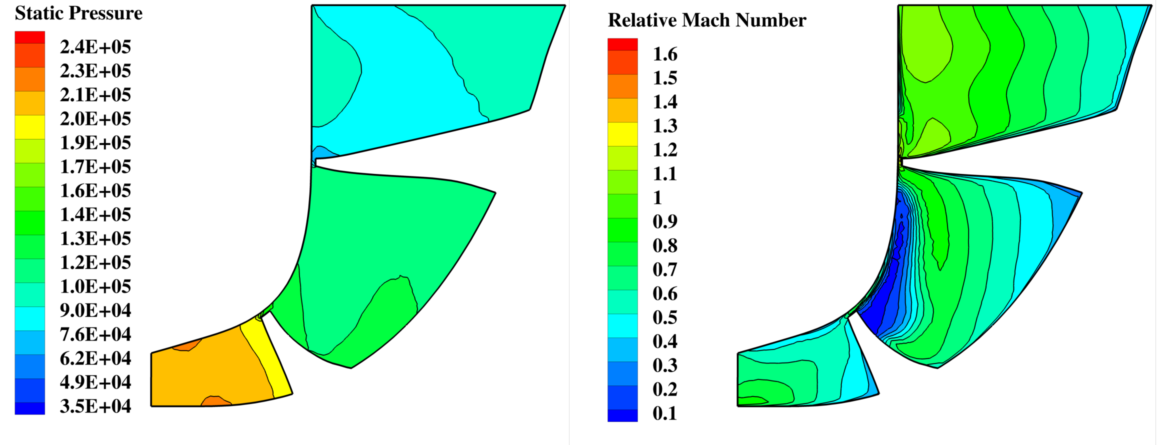

(a) (b)

Figure 4.29: Impeller static pressure distribution (a) and impeller relative Mach number distribution (b) for a compressor with only surge channel included near surgin margin at 120k impeller shaft rotational speed

During near surge compressor operation, the recirculating flow inside the surge port has a positive pre-whirl (rotating in the same direction as the impeller) when it reenters back to the inducer's main flow. The recirculating flow decreases the wheel tip relative velocity reducing both the Mach number and the inducer tip incidence angle. The decrease in Mach number and the incidence angle diminishes the inducer's energy losses, delaying surge [15, 69].

The pressure difference between the shroud and the inducer forces a recirculation (backflow) flow in the surge port, increasing the surge margin. This pressure difference must be higher than the port's pressure loss to induce the backflow. Prober shape and size optimization of the surge port geometry is essential so that pressure loss in the surge port is reduced.

The circumferential recirculated flow near surge mixes with the axial flow inside the inducer. During the mixing of the two flow streams, the surge port's inefficient design is susceptible to inducing flow separation and mixing losses at the impeller inlet. The bleed flow angle and velocity magnitude are dependent on the shape and size of the surge channel end near the inducer.

Various shapes and angles are analyzed during the optimization process and a 90-degree entrance seems to aid the flow move in the axial direction. (more)

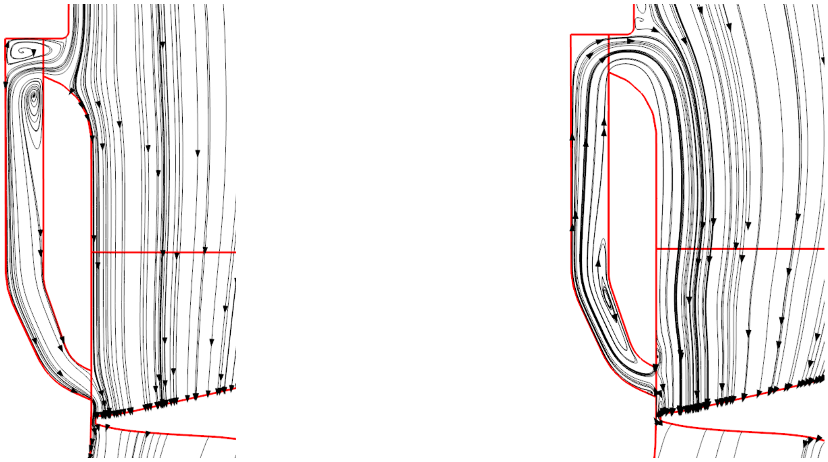
(a) (b)

Figure 4.30: Impeller Static Pressure distribution (a) and impeller relative Mach number distribution (b) for a base compressor operating near choke margin at 120k impeller shaft rotational speed

The surge channel improved the surge limit by about 5% compared to the baseline compressor without any casing treatment. Including the surge port increased the surge limit without a significant efficiency drop from the baseline compressor. In the active casing geometry compressor operation, the choke channel's addition, even though closed near surge operation, deteriorate the compressor efficiency by almost 3%. The figure below shows the compressor pressure ratio and efficiency values for the three compressor configurations: the baseline with no casing treatment, when only the surge channel is included, and when both the surge and the closed active choke channels are included.

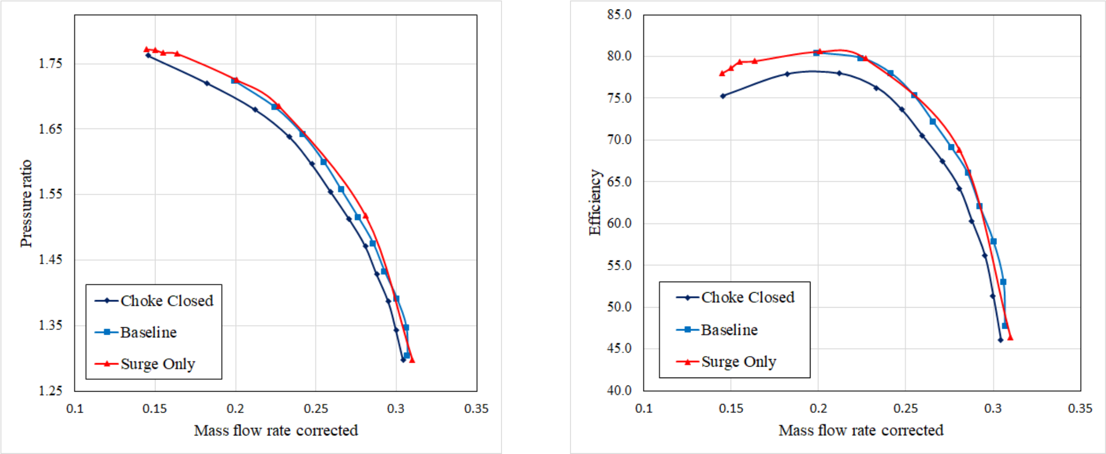

(a) (b)

Figure 4.31: Plots of pressure ratio vs. corrected mass flow rate (a) and Efficiency vs. corrected mass flow rate (b) for three compressor configurations:basline with no casing treatment, compressor with the surge port added, and compressor with the surge and the closed choke ports added at 80k impeller speed

The flow recirculation occurs in the surge channel when the pressure difference between the inducer and shroud casing is high enough to force a flow. In most of the compressor speed lines, there is no recirculation flow inside the surge channel [15]. This reasons why the pressure ratio and efficiency values for the compressor configuration with the surge channel are close to the baseline compressor without any casing treatment.

The casing treatment effect on the Mach number distribution of the compressor at 95% span location is plotted in Figure 4.32 for base compressor without any casing treatment and for compressor equipped with both surge and choke slots. Two impeller rotational speeds are considered:the first at the design point, and the second at the maximum rotational speed of the steady-state analysis. For both rotational speeds considered the presence of the choke and surge slots show a distinct reduction of the Mach number near the slot positions. The plots also revealed a pronounced difference of the Mach number distribution with the increase in the impeller rotational speed.

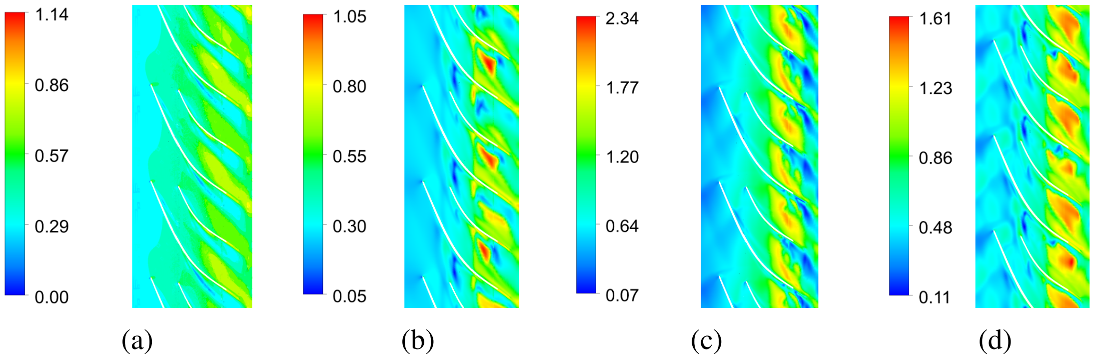

(a) (b) (c) (d)

Figure 4.32: Relative Mach number at 95% span of the compressor running near choke condition at design point and maximum rotational speed: with no casing treatment (a,c), when both surge and choke channels are open (b,d)

4.6 Choke Channel Geometry Optimization

The choke channel extends the choke margin of the compressor beyond the sonic limit by bypassing the aerodynamic throat at higher mass flow compressor operation. The choke channel slot is closed for near surge operations, disconnecting the additional flow path between the compressor shroud surface below the aerodynamic throat and the compressor inlet. Initial surge geometry optimization work that includes optimization of the surge channel width, thickness, and angle with the choke slot closed configuration didn't alter the compressor performance that significantly. Conversely, removing the choke slot improved compressor efficiency values considerably near surge compressor operating points, as demonstrated in Figure 4.31. Despite the choke slot being closed, a portion of the flow with higher temperature and pressure values is still directed into the choke slot, altering the compressor flow below the choke slot.

The choke slot doesn't increase the choke margin significantly at lower compressor speeds. In contrast, the choke slot extends the choke margin as the compressor speed increases. At the highest compressor speed considered, the addition of the choke slot improved the choke margin by almost 11%, as shown in Figure 4.15. Therefore, eliminating the choke slot is counterproductive for the compressor operating points near the choke margin at mid to higher compressor speeds. It is possible to modify the choke slot geometry by adjusting the angle of the slot outlet, thickness, and interface position with the compressor shroud surface. Three choke slot thicknesses are considered for the optimization of the choke geometry in this study. The first choke slot geometry is the original one with approximately 5.5 mm thickness, while the other two geometries have 4 mm and 2.5 mm thickness values, as shown in Figure 4.33.

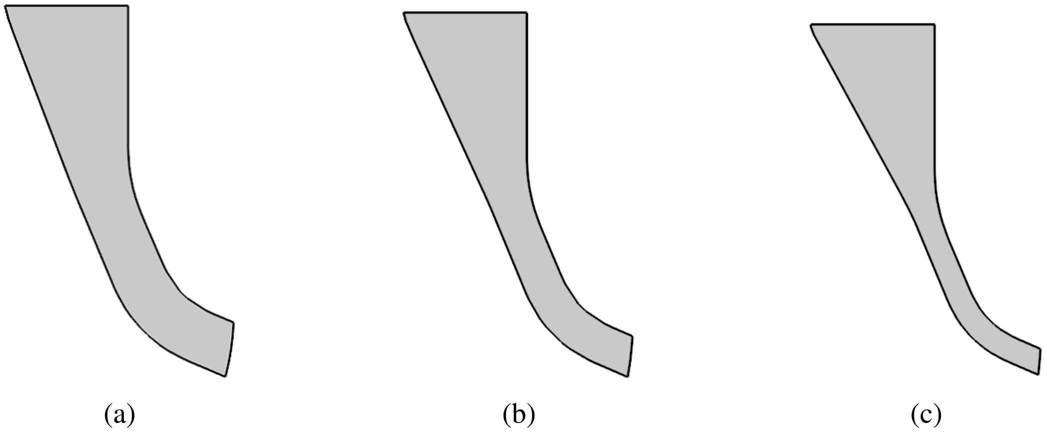
(a) (b) (c)

Figure 4.33: The three choke slot outlet thicknesses: (a) 5.5 mm, (b) 4 mm, and (c) 2.5 mm

Two different compressor rotational speeds - 80k rpm and 120k rpm - are considered for optimizing choke slot thickness, as shown in Figure 4.34 and Figure 4.35. In both compressor speeds, the pressure ratio between the compressor inlet and exit is not significantly affected. In contrast, the compressor efficiency is greatly affected when the operating point approaches the surge margin, which becomes more noticeable as the compressor speed increases. The original choke slot closed compressor design delivered a lower efficiency value of about 3% compared with the one without any choke slot. As the choke slot thickness decreased, the isentropic efficiency value approached the value of no choke slot compressor.

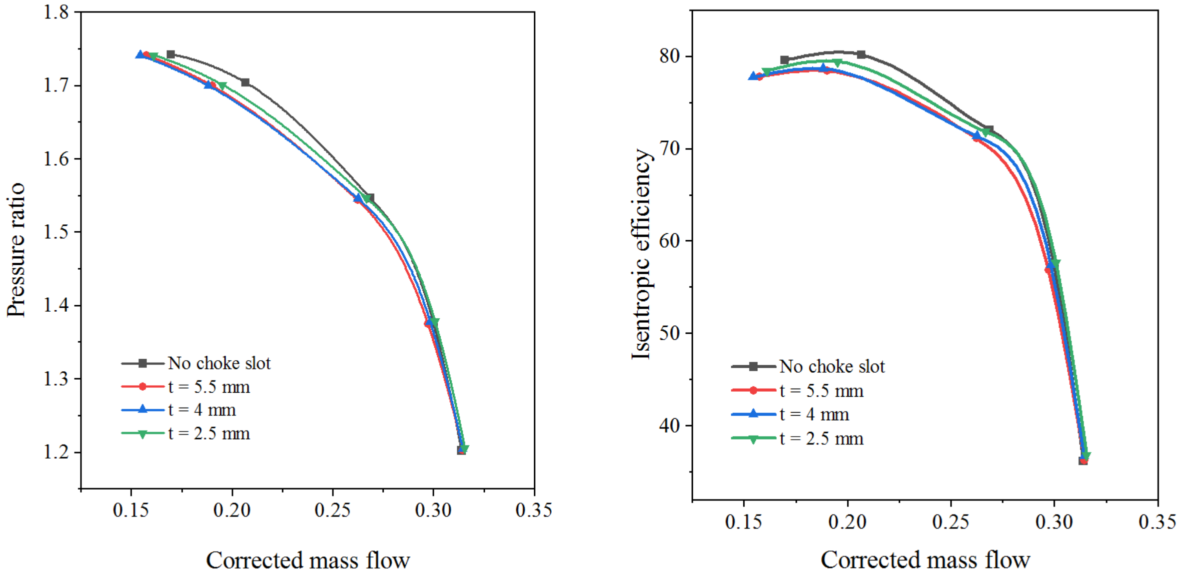

(a) (b)

Figure 4.34: Effect of the choke slot thickness on the pressure ratio (a) and isentropic efficiency (b) values at 80k rpm impeller speed

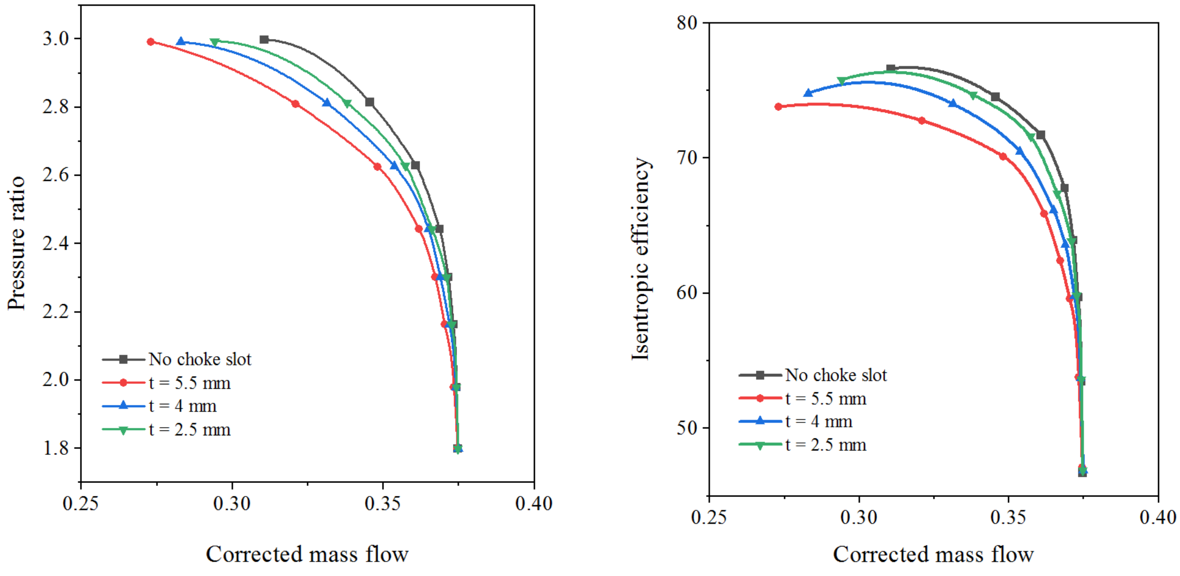

(a) (b)

Figure 4.35: Effect of the choke slot thickness on the pressure ratio (a) and isentropic efficiency (b) values at 80k rpm impeller speed

In both compressor speeds, the variation in choke slot thickness does not affect the near-choke performance of the compressor. This is understandable as the compressor performance plots in

Figure 4.15 demonstrate the choke slot closed configuration does not improve the choke margin. Another interesting finding of this optimization work is the slight shifting of the speed lines to the right as the choke slot thickness decreases, which indicates that even when closed, the choke slot helps improve the surge margin.

The choke-slot open compressor configuration increases the choke margin at mid to higher compressor rotational speeds. Figure 4.36 shows the results of the slot thickness optimization for choke-slot open compressor configuration. Decreasing the choke slot thickness resulted in an improved pressure ratio and isentropic efficiency values. The choke slot with a thickness value of 2.5mm exhibited an increased choke margin and a higher isentropic efficiency near surge operating points.

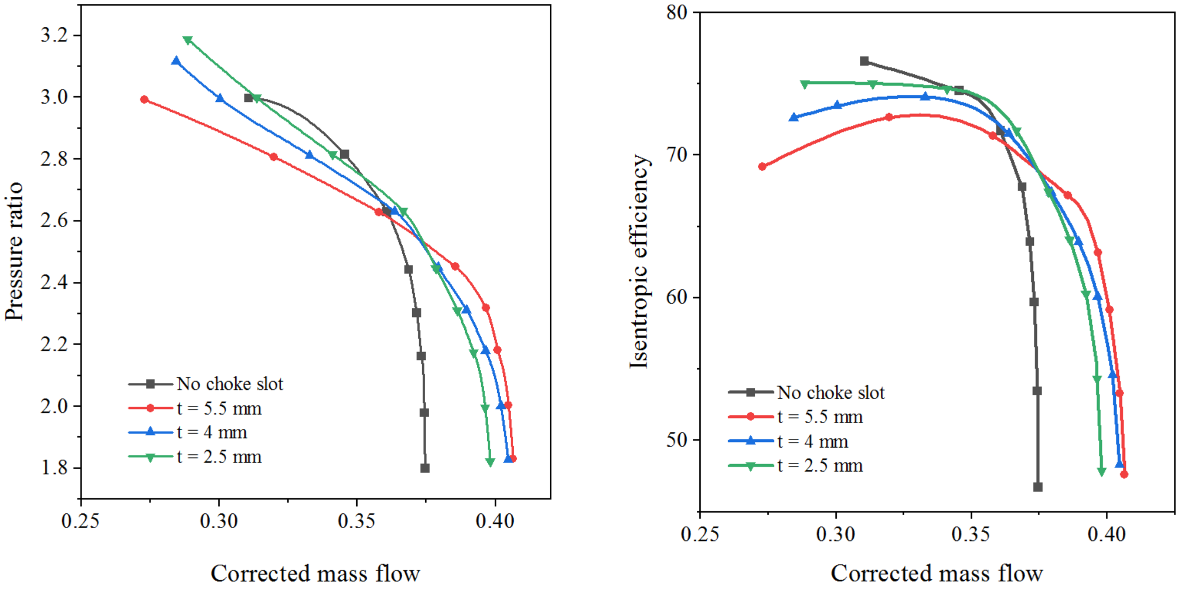

(a) (b)

Figure 4.36: Effect of the choke slot thickness on the pressure ratio (a) and isentropic efficiency (b) values at 120k rpm impeller speed when the choke slot is open

CHAPTER 5

COMPRESSOR AEROACOUSTICS PERFORMANCE STUDY

5.1 Introduction

Turbocharger noise arises from passive and active sources. Passive sources consider the low-frequency propagation of pressure pulsations from the engine into the intake and exhaust systems, whereas the active noise sources are related to the fluid flow in the turbocharger system. Many researchers in recent years have studied noise created in centrifugal compressors; Evans and Ward [22] concluded the broadband ’whoosh’ noise, also known as surge noise, in automotive turbochargers operating near full load acceleration is due to the turbulence generated when the compressor operates within or close to the marginal surge line. Teng and Homco [23] suggested that this surge noise can be reduced by improving the surge margin applying a negative pre-whirl at the compressor inlet.

Raitor and Neise [24] experimentally investigated the sound generation mechanisms in centrifugal compressors to identify tonal noise at blade passing frequencies, buzz-saw noise, and blade tip clearance noise as the primary sound sources. Buzz-Saw Noise occurs near the leading edge of the rotor blades at supersonic flow condition. Due to the rotor manufacturing irregularities, the buzz-saw pressure distributions are not circumferentially identical. The impeller blade produces buzz-saw noise, a monopole type source, with its contribution felt at harmonics of the rotor shaft frequency [38].

Inflow disturbances and rotor-stator interactions create a fluctuating pressure source, a dipole source, of noise. This acoustic signal consists of harmonics of the blade passing frequency (BPF) defined as the product of the rotor shaft frequency and the number of main rotor blades. The secondary flow through the gap between the compressor casing and the impeller blades induced a narrow-band noise termed as “tip clearance noise” (TCN). The effect of TCN is pronounced at mass flow rates less than the design flow rate [24].

The effect of the casing treatment on the turbocharger acoustics is investigated experimentally by Dehner [21] and Tanna [70]. Tanna et.al. developed an optimized ported shroud compressor housing targeting improved aerodynamic performance and lower blade pass acoustic level. They reported that the presence of the ported shroud contributed to an increase of BPF noise level by approximately 15-20 dB.

Besides experimental works, various researchers have concluded favorably on the capability of transient CFD simulations predicting the turbocharge noise [71, 72, 73]. Unsteady Reynolds Average Navier-Stokes (URANS) flow models, although computationally cheaper, do not predict flow-induced noises accurately [74, 28]. On the other hand, LES models are capable of resolving the flow-induced sounds rigorously with incurred computational cost as LES demands more elements close to the walls [75]. Detached Eddy Simulation (DES), a hybrid modeling approach that uses RANS simulation for part of the flow near to the wall and LES for part of flow far enough from the wall, is employed for the transient simulation in this study. Improved Delayed Detached Eddy Simulation (IDDES) of StarCCM+ is selected to allow RANS to be used in wall distances much smaller than the boundary layer thickness. For all precursor steady-state and transient simulations, the boundary condition at the inlet is modified to eliminate the non-reflecting boundary effects by using free-stream boundary condition as recommended by CD-Adapco [28].

In this thesis, compressor spectra at two compressor speeds at 120k and 80k rpm are analyzed using DES turbulence modeling. Choke channel closed configuration is selected at 120k rpm with the compressor operating near surge. At 80k rpm compressor speed, the near design operating point with the choke channel open configuration is selected. A polyhedral mesh is used to determine the acoustic performance of the compressor at all flow conditions considered. Due Consideration must be given in setting the appropriate mesh size such that, the mesh can resolve both the sound generating turbulence scales as well as the propagating acoustic waves [28].

5.2 Effect of the Casing Treatment Geometry on the Turbocharger Noise

Broadband and tonal noises arising from pressure fluctuation near the boundary or form flow turbulence are inherently transient. CFD simulations, such as CAA (computational aeroacoustics) or segregated source propagation methods, can accurately model the transient flow to identify the noise source and its propagation. CAA simulations provide detailed noise data that includes the estimates of the noise spectrum, directiveness, and SPL levels by employing very fine mesh at small temporal discretizations. Despite their advantages, CAA simulations are computationally expensive and impractical for grading design varieties on the noise signatures they generate. Broadband noise sources, on the other hand, based on steady-state simulations, offer a valuable and inexpensive estimate of noise source strength, employing approximate analytical models. The broadband steady-state noise analogies include the Curle surface acoustics, Proudman acoustic power, and Liley turbulent shear flow noise models.

The Curle's analogy estimates the dipole noise sources on the compressor surface. The analogy assumes an isotropic turbulent flow field to calculate the fluctuating surface pressure on the flow by the presence of solid boundaries [28]. The dipole noise sources in rotating machines arise due to rotor-stator interaction that involves fluctuating pressure fields created by the rotor on diffuser blades (if they exist). The dipole noise is periodic and consists of the blade passing frequency (BPF) and its harmonics. Another source of dipole noise is the blade vortex shedding due to flow leaking from the blade's high to the low-pressure side.

The Proudman acoustics power shows the estimation of the local contribution of the quadrupole source as generated by isotropic turbulence [28]. Since turbulence near the wall is not isotropic, the estimate is not perfect in the boundary layer regions.

Two compressor operating points at a speed of 120k rpm are used to evaluate the compressor broadband noise sources. For the speed line considered, the first operating point falls close to the maximum efficiency point of the compressor's speed line, and the second point is close to the surge point, where increased flow-induced noise is expected due to higher flow recirculation. Broadband noise sources are evaluated for choke slot open and closed configurations.

Figures 5.1 and 5.2 show the acoustic power in dB predicted by Proudman's analogy. Volume integrals of the Proudman's acoustic power are used to predict the turbulent noise generated from each compressor part. In all four compressor points investigated, the impeller is the primary source of the quadruple noise, followed by the volute. The impeller is responsible for more than 65% of the noise generated by the flow turbulence. When the compressor point moves from near maximum efficiency to the surge point, the contribution of the inlet parts increases from 2% to 23% in the choke slot open configuration. With the choke slot is closed, the amount of turbulent noise generated by the choke channel rises from 3 to 12% as the operating point nears the surge limit

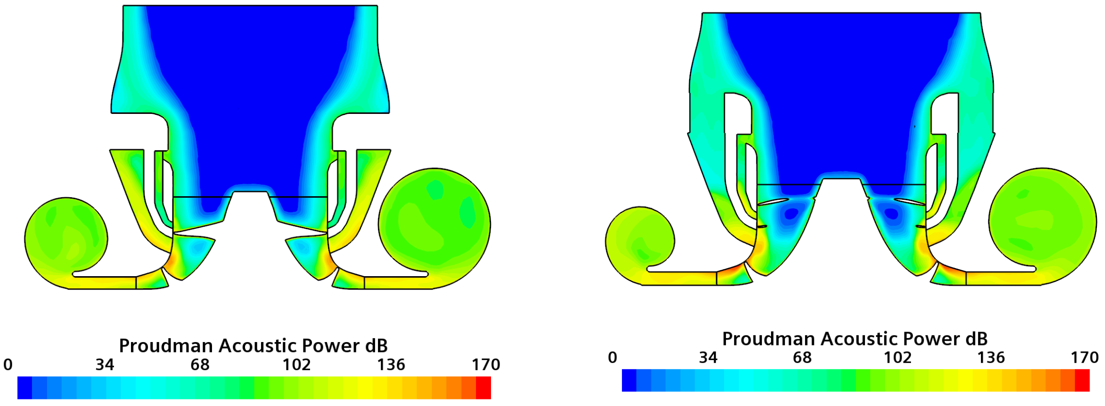

(a) (b)

Figure 5.1: Proudman acoustic power (dB) at 120k rpm compressor speed near maximum efficiency point for: (a) choke slot closed configuration, and (b) choke open configuration.

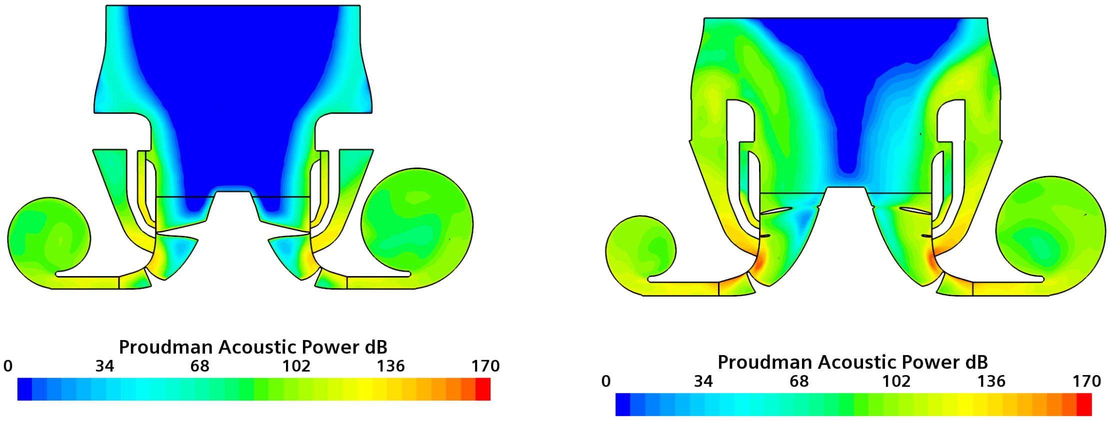

(a) (b)

Figure 5.2: Proudman acoustic power (dB) at 120k rpm compressor speed near surge point for: (a) choke slot closed configuration, and (b) choke slot open configuration.

The separated flow downstream of the choke channel and tip gap flows are the primary impeller regions responsible for noise generation, as shown in Figures 5.1 and 5.2. In the choke slot closed compressor configuration, the choke and surge slot flow induces a locally rotating separated flow that contributes to the quadrupole noises. As the compressor operating point approaches the surge, the turbulent noise generated by the choke and surge slots increases. With an open choke slot compressor configuration, as the compressor's operating point moves to the surge point, more flow recirculates in the choke channel, causing turbulent noise in the choke slot and compressor inlet parts.

Figures 5.3 and 5.4 show the compressor noise generated by dipole sources. The noise generated by dipole sources is estimated by surface integrals of acoustic power based on Curle's analogy. Almost half of the noise from the dipole source comes from the impeller surfaces, while the rest is from volute surfaces. The dipole sound sources are more pronounced in the impeller tip, impeller exit, and the vaneless diffuser walls where the static pressure builds up.

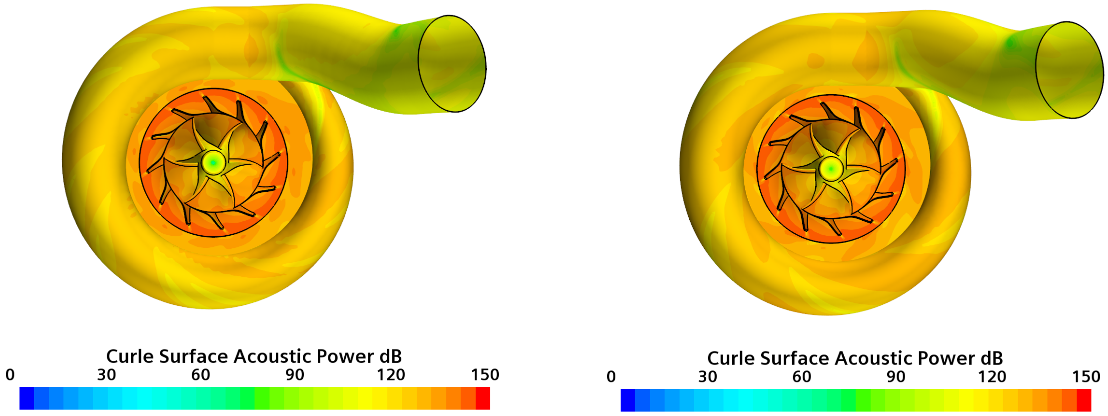

(a)

(b)

Figure 5.3: Curle surface acoustic power (dB) at 120k rpm compressor speed near maximum efficiency point for: (a) choke slot closed configuration, and (b) choke slot open configuration.

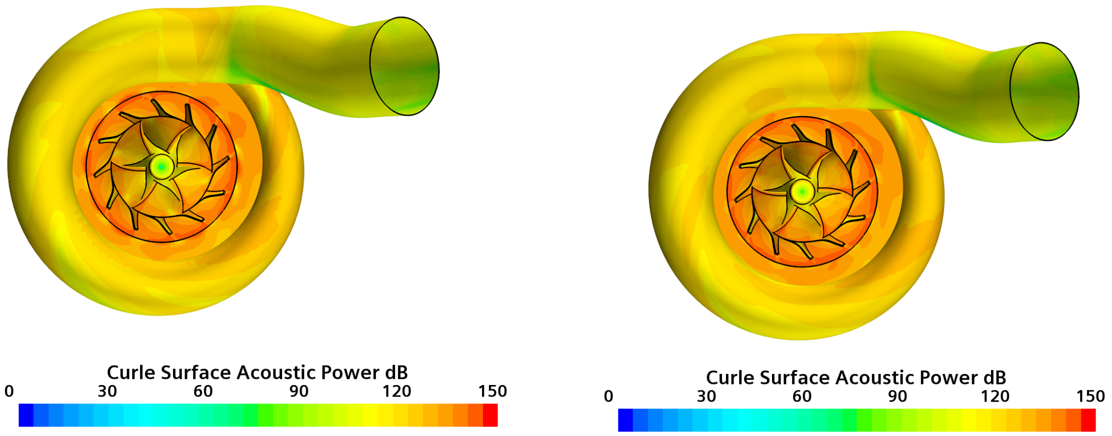

(a) (b)

Figure 5.4: Curle surface acoustic power (dB) at 120k rpm compressor speed near surge point for: (a) choke slot closed configuration, and (b) choke slot open configuration.

The steady-state acoustic analogies are helpful to identify the different noise sources. However, both Proudman and Curle's aeroacoustic analogies are unable to predict the dominant noise frequencies. Consequently, for more comprehensive noise source identification, directiveness, and propagation study, transient analysis of the compressor models is required for various compressor configurations and speeds.

5.3 Transient Aeroacoustics Performance of the the Turbocharger Compressor

The system of non-linear partial differential equations of Navier-Stokes equations does not have analytical solutions. Consequently, numerical techniques are used to solve the equations with additional considerations of boundary and initial conditions. In this study StarCCM+, a finite volume and element CFD software is used.

The transient acoustic performance of the compressor is evaluated near surge operating point where the noise level is expected to be high [71]. Consequently, the pre-cursor steady state analysis is computed when the choke slot is closed as shown in Figure 4.13b.The other compressor configuration considered for the transient simulation is the choke slot open case as shown in Figure 4.13c. As a result of the choke slot being open, an additional flow path is created, potentially increasing the compressor's noise level.

5.3.1 Spatial Discretization

Transient aeroacoustic CFD mesh size estimation is done by examining the results of a precursory steady-state simulation. Appropriate mesh size is set iteratively depending on how well the mesh resolves the turbulence scales generating the sound. In starCCM+, the Mesh Frequency Cutoff scalar field function identifies areas requiring further mesh refinement based on the highest frequency of interest [28, 76].

According to Wagner [76] for a local turbulent kinetic energy k and a cell dimension of Δ, the smallest length scale of a turbulent eddy structure captured by the mesh is 2Δ. The isotropic fluctuation velocity is $\sqrt{2k/3}$. The maximum frequency resolved by the local grid spacing Δ is calculated by,

$$f_{MC} = \frac{\sqrt{2k/3}}{2\Delta} \tag{5.1}$$

Mesh size requirement to resolve acoustic waves for direct aeroacoustic CFD simulations properly depends on the shortest wavelength to be resolved in the simulation [28]. For second-order schemes, it is recommended to have 15-20 grid points per wavelength [77]. Using the maximum frequency to be resolved and the speed of sound of the flow, the mesh size to resolve acoustic waves can be estimated by Eq.(5.2) [28] as,

$$\Delta = \frac{C - U}{20f} \tag{5.2}$$

where U is the mean velocity of the flow, C is the speed of sound and f is the maximum frequency of the flow. The ratio between integral length scale (L_t) and local grid size (Δ) is also plotted at various fluid domain cross-sections. These plots are used to locate the mesh regions outside the boundary layer where the grid size is not sufficiently fine enough to resolve 80% of the turbulent kinetic energy of large energy-containing eddies. The turbulence integral length can be equated from the converged precursor RANS steady state simulation as [40]:

$$L_t = k^{1/2}/C_{\mu}\omega \tag{5.3}$$

The local grid size is estimated from the cell volume, $\Delta = \sqrt[3]{V_{cell}}$. The mesh capacity to resolve the propagating acoustic waves is also checked using 20 cells for the shortest wavelength resolved in the simulation as recommended by CD-Adapco [28]. for second-order space and time discretization. For higher-order discretization, the number of elements desired lowers significantly; for six-order schemes, 6 – 10 elements are enough [78]. Mesh frequency cutoff plot for open choke configuration is shown in Figure 5.5.

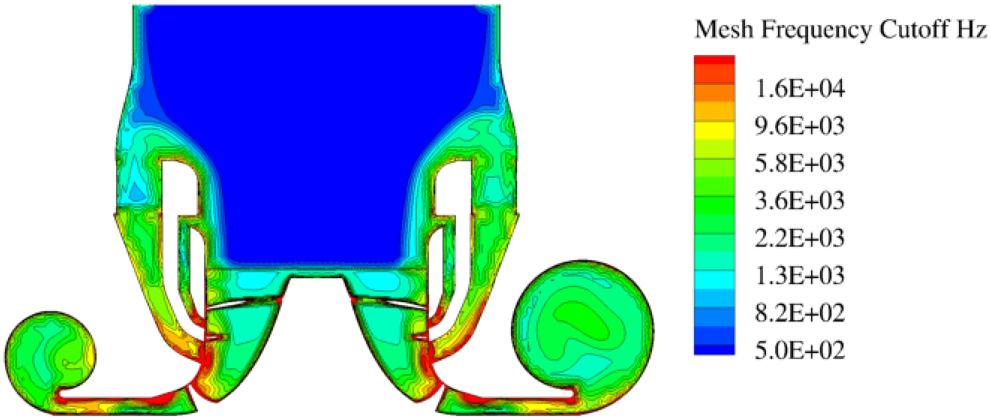

Figure 5.5: Mesh frequency cutoff plot for open choke configuration

The mesh frequency cutoff value in the inlet region is relatively small as the turbulent isotropic velocity fluctuations have a lower magnitude, allowing larger local mesh sizes upto 1.5 mm. A constant mesh size of 0.5 mm is applied in the impeller region to resolve acoustic waves progressing upstream of the flow.

The near wall prism cell thickness is varied from meshes used for steady-state performance studies to keep the y+ value less than one in all first layer prism cells. The mesh size of the leading and trailing edge surfaces of the compressor are made fine enough so that the geometry of the impeller is exactly captured by the mesh. The prism cells have 15 layers with 1.3 growth rate in all wall boundaries. The impeller hub and blades y+ value is displayed Figure 5.6.

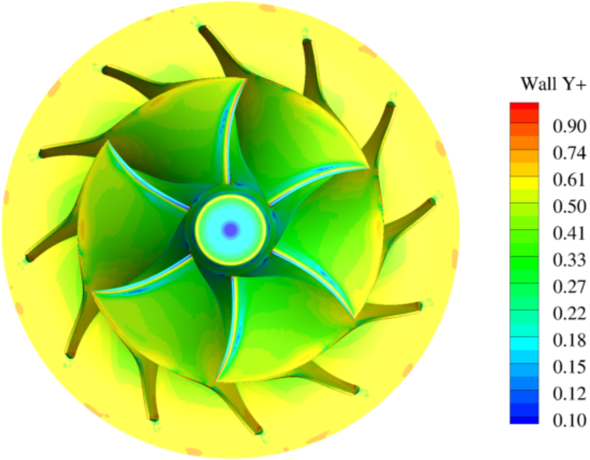

Figure 5.6: Impeller y+ value for choke open configuration

Approximately 33 million polyhedral and prism cells are used in the near surge transient aeroacoustics simulation of the choke-closed compressor rotating at 120 k rpm. In contrast, for the choke-open compressor aeroacoustics simulation at 80k rpm near the design point, approximately 25 million elements are used.

Total pressure at the start of the inlet pipe and static pressure at the end of the exit pipe are selected as a boundary condition for the simulation. These boundary conditions are used in all RANS steady compressor map generation simulations. The same boundary condition is kept for all DES simulations. No-slip boundary condition with no heat transfer (adiabatic) is used at the wall.

5.3.2 Temporal Resolution

The transient acoustic simulation requires accurate time resolution. Courant Number, maximum resolvable frequency, and local Strouhal shedding frequency criterion are all checked to find minimum time step to minimize numerical dissipation as recommended by CD-Adapco [28]. The ratio of the spatial to temporal resolution gives the dimensionless Courant-Friedrichs-Lewy (CFL) number. The Courant number is based on the velocity of the fluid, u, given by:

$$CFL = \frac{u\Delta t}{\Delta x} \tag{5.4}$$

where Δt is the temporal resolution, Δx is space resolution and u, flow velocity. For LES and DES simulations the CFL values are chosen to have a value near unity. For acoustic simulations of compressible flows, considering the speed of sound, the flow velocity is modified to be, $|u| + c$, to resolve high sound frequencies [28].

The flow vortex shedding frequency should also be considered in estimating the temporal resolution of the simulation. Strouhal number is defined as,

$$St = \frac{fd}{U_\infty} \tag{5.5}$$

where f is vortex shedding frequency, d is the Characteristic size of the body and U_∞ is the flow velocity. Strouhal number can be equated from Reynolds number as [79],

$$St = 0.198\left(1 - \frac{19.7}{Re}\right) \tag{5.6}$$

Temporal discretization can also be set by specifying the number of time steps per blade passing. ANSYS Fluent [80] recommends 20-time steps per blade passing, while CD-Adapco [28] recommends 15. Navarro [72] has concluded accurate low-frequency spectra prediction can be achieved using a time step up to $\Delta t = 4$. For all aeroacoustics transient simulations in this thesis, checking the convergence, the mesh is set to rotate at $\Delta t = 0.5$ per time step for all transient runs.

5.3.3 Fourier Transform of the Generated Noise

Point time Fourier transform are used to deconstruct signals in time domain representation to frequency domain representation so that the dominant frequencies of the noise in the flow can be identified.

When the measured signal does not have an integer number of periods, a phenomenon called spectral leakage occurs. Spectral leakage induces discontinuity in the FFT by adding high-frequency components not present in the original signal. This causes an altered FFT amplitude with spectral noise lines that spread into wider frequency values. The effects of spectral leakage are minimized by applying windows on the input data tapering the data off at both ends. This force the endpoints of the waveform to meet resulting in a continuous waveform without sharp transitions. In this study, the Hanning window with three blocks and a 50% overlapping ratio is selected for the Fourier transform of the pressure probe signals.

5.3.4 Pressure Spectra

The inlet and exit pipes of the turbocharger are modeled as straight ducts by extruding the inlet and volute end cross-sectional diameters five times longer to reduce the computational effort [73]. The CFD domain also includes three pressure point probes on exit and inlet pipe extrudes. In addition to the pressure point probes, three circumferential line pressure probes on each exit and inlet pipe extrude are included, as shown in Fig. 5.7.

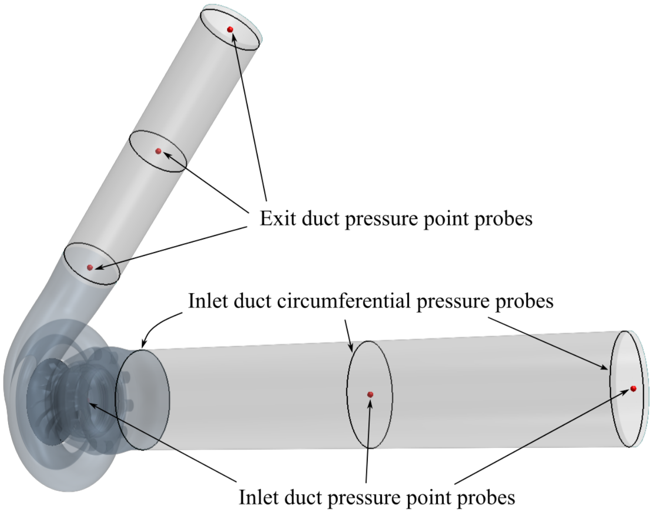

Figure 5.7: Circumferential line and point probes of the turbocharger CFD fluid domain

The sound power spectrum of the compressor operating near surge is composed of broadband and pure tonal noises. The inlet pipe noise spectrum is plotted in Figure 5.8 and Figure 5.9, while Figure 5.10 and Figure 5.11 display the noise spectrum at the outlet pipe. Based on the rotational speed of the compressor and the number of main blades in the compressor, the blade passing frequencies (BPF) can be determined as:

$$BPF = Z_{MB} \times n/60 \tag{5.7}$$

where Z_{MP} is the number of main blades and n is the compressor rotational speed in rpm.

As shown in the figures, the first harmonic of the BPF noises have the highest value with subsequent decreases of the SPL levels with the increase of the harmonics. Raitor and Neise [24] proved the SPL level of the BPF noises, and their harmonics increase with an increase in the rotational speed of the impeller.

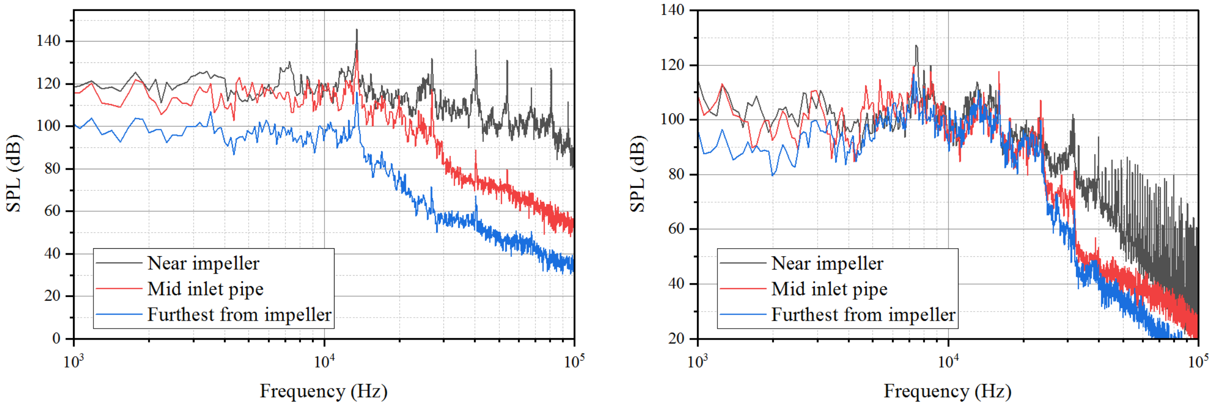

(a) (b)

Figure 5.8: Inlet pipe center point pressure spectra for near surge choke-closed compressor operation at 120k rpm (a), and near design point choke-open compressor operation at 80k rpm (b).

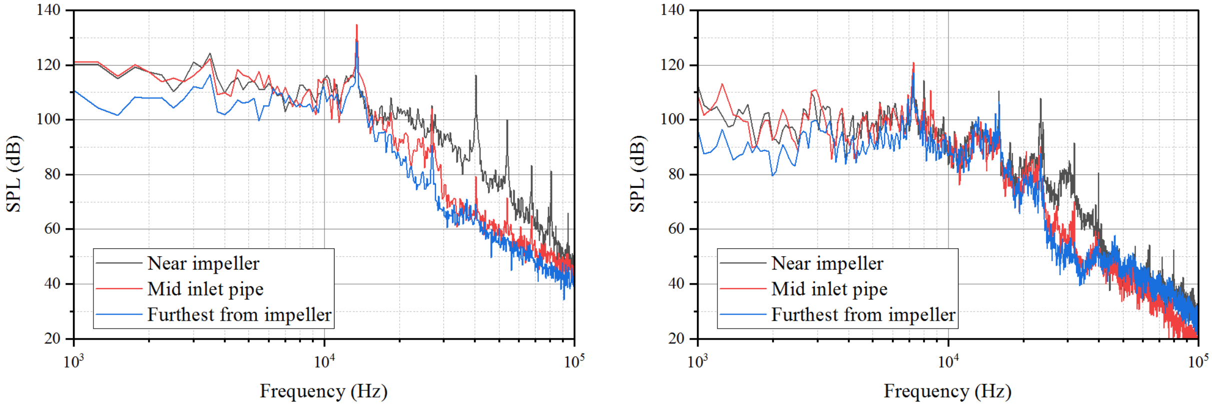

(a) (b)

Figure 5.9: Inlet pipe circumferential line average pressure spectra for near surge choke-closed compressor operation at 120k rpm (a), and near design point choke-open compressor operation at 80k rpm (b).

The BPF noise level at the exit duct is found to be higher than the inlet duct noise level by approximately 20 dB. A pronounced decay in broadband and tonal noise levels is observed as the

the pressure probe points move away from the impeller in both inlet and exit ducts as demonstrated in Figure 5.8 and Figure 5.10. Noise level predicted from the center probe points and the line average circumferential probe points gave equivalent results for broadband and tonal noises. The circumferential probes, however, distinguished the sound level better at higher BPF harmonics.

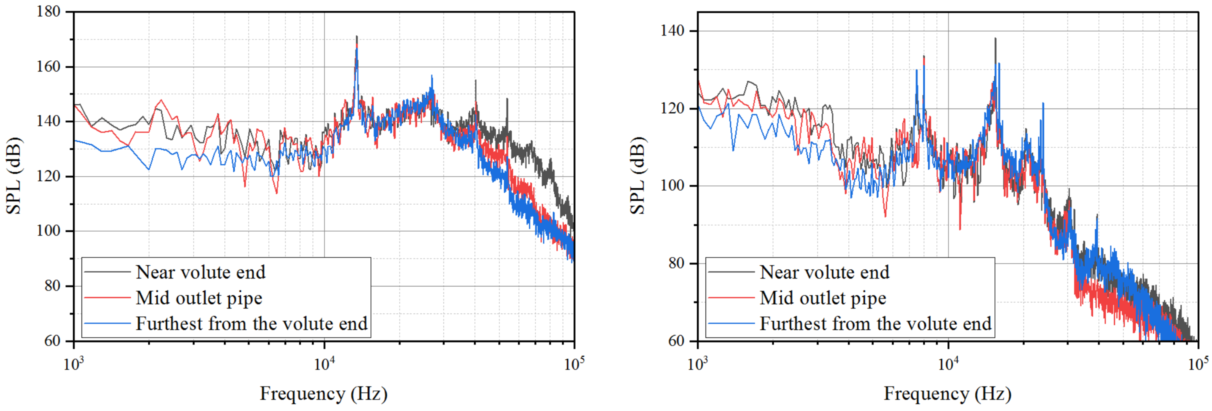

(a) (b)

Figure 5.10: Exit pipe center point pressure spectra for near surge choke-closed compressor operation at 120k rpm (a), and near design point choke-open compressor operation at 80k rpm (b).

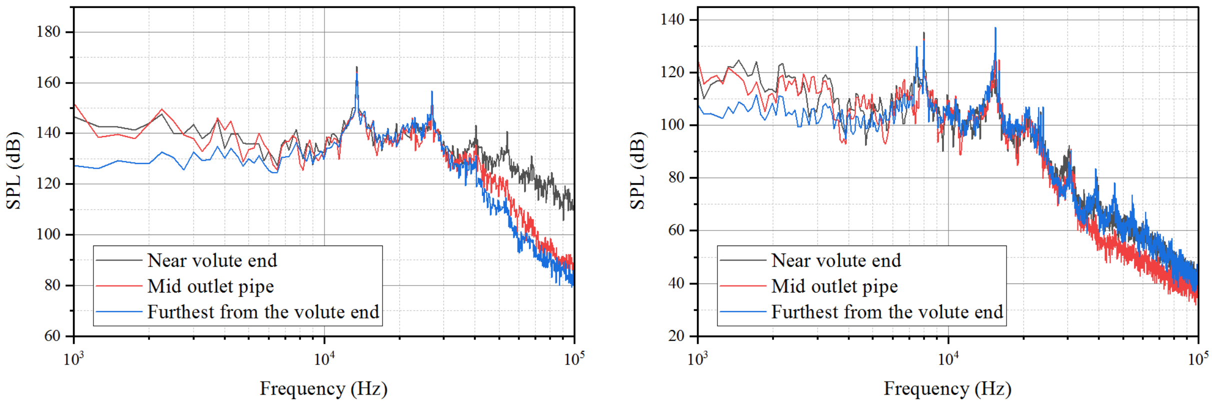

(a) (b)

Figure 5.11: Exit pipe circumferential line average pressure spectra for near surge choke-closed compressor operation at 120k rpm (a), and near design point choke-open compressor operation at 80k rpm (b).

The effect of the compressor rotational speed on the BPF and broadband noises is studied by comparing the pressure spectrum of inlet and exit probe points located furthest away from the compressor wheel, as shown in Figure 5.12. Both broadband and BPF noise levels increased with the rotational speed of the compressor.

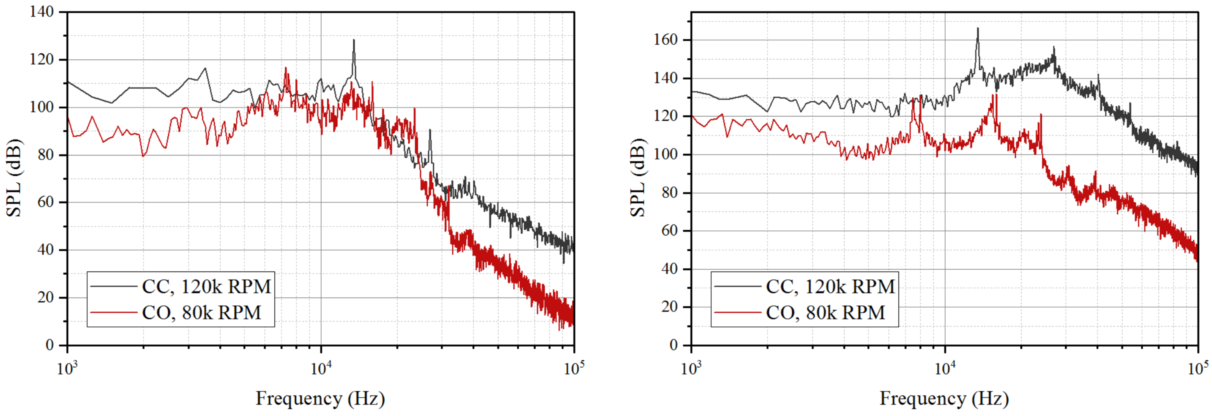

(a) (b)

Figure 5.12: Pressure spectra at further probe point away from compressor wheel for the inlet pipe (a), and for the exit pipe (b).

CHAPTER 6

DUAL-ENTRY TURBINE PERFORMANCE ANALYSIS

6.1 Introduction

Demanding exhaust gas emission standards for diesel engines has forced car manufacturers to develop innovative designs that decrease nitrogen oxides (NO_x) and particulate matter releases. For turbocharged diesel engines, exhaust gas recirculation (EGR) systems help reduce NO_x emission levels by decreasing engine combustion temperature [81, 82, 83, 2]. EGR operation in engines with variable geometry turbochargers (VGTs) is closely tied with the VGTs control. Conventional VGTs designs are equipped with a nozzle angle-adjusting system to alter the exhaust gas flow through the engine's EGR valve by increasing the upstream turbine pressure at a nearly closed nozzle vane position [81, 83]. The VGTs also help regulate the engine intake air boost at various engine operating conditions.

During the blow-down phase of a medium-duty engine with more than four cylinders, exhaust gas pulse energy is utilized better if flows from the different cylinders are grouped based on firing order and engine layout [12]. Turbocharger manufacturers commonly use twin and double-entry volutes to isolate pressure peaks into two streams to avoid pressure peak dumping. Twin and double-entry volutes, compared with single-entry volutes, offer improved turbine power output and better compressor efficiency value with additional casting and design-specific material costs.

In twin-entry volutes, the two flow streams from the engine exhaust manifold feed the entire turbine inlet circumference preserving the flow pulse energy by isolating each stream into two scrolls. The flows in the scrolls interact with each other before being admitted to the turbine. Turbocharger manufacturers adopt the twin-entry volute option for its relatively inexpensive and simple design.

High-pressure difference between scrolls in twin-entry volutes forces a cross-flow between scrolls at the exhaust blow-down phase. In cross-flow, a portion of the higher pressure gas is directed away from the turbine wheel as it recirculates in the second scroll altering flow direction and turbine efficiency. Lückmann,Dominik, et al, [84, 85] used hot gas test bench results to quantify the amount of cross-flow in twin-entry volutes. To reduce the impact of cross-flow in exhaust pulse separation, they suggested utilizing circumstantially segmented turbine admission, double-entry volutes, with minimized flow interaction between the two entries of the volute with the exclusion of areas near the tongues. In double-entry volutes, the inlet is divided into two channels, where each channel feeds approximately each half of the turbine circumferential area.

Various researches have discussed double entry turbine performance at full and partial admissions using steady and transient state numerical simulations [86, 87, 88, 89]. Copeland et al. [86] used steady state simulation results to study the effect of unequal flow across the two volute entries on turbine performance. Their analysis showed increased mixing losses at nozzle inter-space and turbine rotor wheel regions at partial admissions flow cases.

Several studies have applied local entropy production analysis to identify turbocharger components' losses using RANS and LES CFD simulations [88, 89, 90, 91]. Palenschat et al. [90] applied local entropy generation analysis to audit a twin-scroll turbine losses. Their work showed accurate estimation of local entropy generation from CFD results is highly mesh dependent. They also identified loss locations, and portions are significantly admission dependent.

In this chapter how a double inlet, variable geometry turbocharger, loss distribution develops for one even and three uneven admissions at low to high turbine mass flow rates. The local entropy generation rates are computed for eleven sub-regions of the CFD model to identify the turbine loss sources. The effect of an uneven turbine inlet flow on local entropy distribution is also discussed for each of the three mass flows considered for the study.

6.2 The CFD Methodology

All computational results are obtained using StarCCM+, a commercial finite-volume solver. The Reynolds averaged Navier-stokes (RANS) steady-state equations are utilized to evaluate the turbine performance at three pre-selected operating conditions. Four admissions, one even and three uneven, are assessed at each of the three cases. A full 3D model, composed of the volute, the nozzle, the turbine wheel, and the diffuser, is developed to replicate the turbine's exact flow development as close as possible. Polyhedral cells are selected for all through-flow regions far away from the wall, while prism cells with ten layers are used for all near-wall flow regions. Compared with hex and tet elements, polyhedral cells have a higher face to element count ratio with an equal refinement level, resulting in a reduced computational time [92]. The thickness of the first layer of the prism cells nearest to the wall is set, targeting a $y^+ \leq 5$ value at operating condition close to the design point so that near wall turbulence is well resolved. The first layer thickness value also aids in proper cell thickness propagation from near wall to core flow regions.

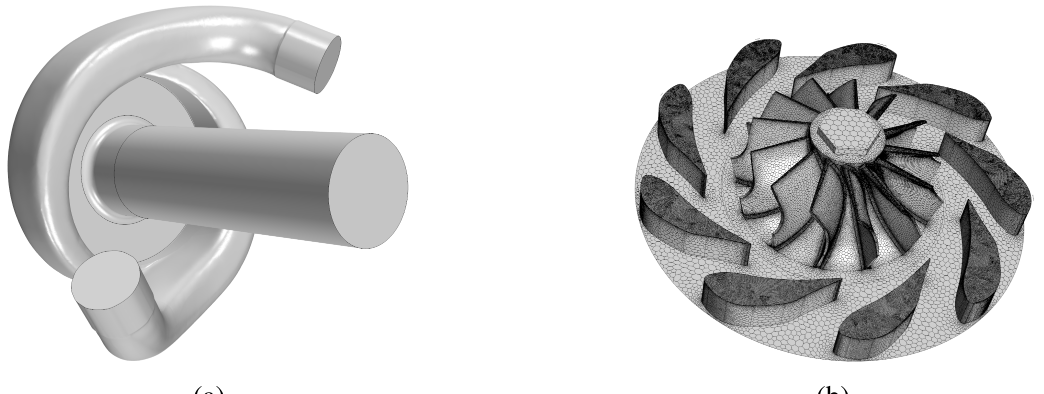
(a)
(b)

Figure 6.1: (a) full computational domain , and (b) Nozzle and rotor blade surface mesh

A constant blade tip to shroud gap of 0.4 mm value is applied at rotor blades. Local surface mesh size controls are adopted to capture curvatures near the leading and trailing edges of both rotor and nozzle blades. The full computational model is displayed in Figure 6.1a, while Figure 6.1b shows the surface mesh of the rotor and nozzle blades. Mesh sensitivity study was conducted considering the variation of impeller moment, mass flow, and isentropic efficiency quantities with total element count of the computational model. A final mesh with approximately 6 million elements and a 2 mm base size is used for all steady-state results in this paper.

The turbine performance analysis applies a mass flow inlet and a static pressure outlet boundary conditions for all simulations. The double-precision version of StarCCM+ with the segregated flow solver is chosen over the coupled flow solver for faster convergence with marginal penalties on the predictions' accuracy.

A k-ω SST model with the re-attachment modification is used for all steady-state simulations in this paper. The k-ω model, a two-equation model, based on turbulent eddy-viscosity relations, is widely used in turbomachinery simulations as it provides a suitable trade-off between accuracy and robustness. The SST model's re-attachment modification provides additional production term to the turbulence kinetic energy equation, improving the accuracy of the model predictions [92].

6.3 Performance Parameters

Four parameters define the turbine performance: the pressure ratio, the mass flow parameter, the isentropic efficiency, and the mean blade speed ratio. In the double-entry turbine's real engine working conditions, since the two inlets' flow properties are different, performance parameter definitions for a single entry turbine should be modified. The pressure ratio values for each entry are defined as a ratio of the total pressure at the two volute inlets and the diffuser exit static pressure value as defined in Eq.(6.1).

$$\pi_{ts,in1} = \frac{p_{0,in1}}{p_{s,out}} \ , \ \pi_{ts,in2} = \frac{p_{0,in2}}{p_{s,out}} \tag{6.1}$$

A single equivalent pressure ratio value for the double-entry turbine is defined in Eq.(6.2) by taking the mass flow average of the two pressure ratio values in Eq.(6.1). At even flow since the two inlets have equal mass flows, the equivalent pressure ratio value is reduced to the arithmetic mean of each inlet's pressure ratio values.

$$\pi_{eqv} = \frac{\dot{m}_{in1}}{\dot{m}_{in1} + \dot{m}_{in2}} * \pi_{ts,in1} + \frac{\dot{m}_{in2}}{\dot{m}_{in1} + \dot{m}_{in2}} * \pi_{ts,in2} \tag{6.2}$$

The equivalent mass flow parameter is defined in Eq.(6.3) as a sum of the MFP values from each inlet.

$$MFP = \left(\frac{\dot{m}\sqrt{T_0}}{P_0}\right)_{in1} + \left(\frac{\dot{m}\sqrt{T_0}}{P_0}\right)_{in2} \tag{6.3}$$

The isentropic total-to-static efficiency for double-entry volute is defined as the ratio of actual work utilized by the turbine to the maximum power available if the air expands isentropically from each entry as expressed by Eq.(6.4).

$$\eta_{ts} = \frac{\overrightarrow{\tau} \cdot \overrightarrow{\omega}}{\left(\dot{m} C_p T_0 \left[1 - (\pi_{ts})^{\frac{1-\gamma}{\gamma}}\right]\right)_{in1} + \left(\dot{m} C_p T_0 \left[1 - (\pi_{ts})^{\frac{1-\gamma}{\gamma}}\right]\right)_{in2}} \tag{6.4}$$

The mean blade speed ratio is evaluated in Eq.(6.5) as defined in Watson [93].

$$\frac{U}{C_{is}} = \frac{U}{\sqrt{\left(\frac{2}{\dot{m}_{total}}\right) \times \left[\left(\dot{m} C_p T_0 \left[1 - (\pi_{ts})^{\frac{1-\gamma}{\gamma}}\right]\right)_{in1} + \left(\dot{m} C_p T_0 \left[1 - (\pi_{ts})^{\frac{1-\gamma}{\gamma}}\right]\right)_{in2}\right]}} \tag{6.5}$$

6.4 CFD Performance Results

6.4.1 Comparison with Experimental Data

In Figure 6.2, the turbine test bench results are compared with CFD results for nine operating points with the turbine shaft running at 70% of the rated turbine speed. The experimental measurements are carried out at Ford Motor Company's turbocharger test rig in Dearborn at equal admission. The test's pressure ratio varies between 1.44 and 1.69, and the speed ratio ranges between 0.52 and 0.62.

Figure 6.2b shows the turbine efficiency values from CFD and turbine bench testing. At higher velocity ratio values (lower loads), the CFD predicted values match well with the test bench results. The discrepancy between the test and CFD results increased at lower velocity ratio values (higher loads), with an efficiency discrepancy as high as 4.2%. Overall, the CFD computations resulted in a higher efficiency value than the test results. The inherent simplification of the RANS CFD models and the adiabatic system assumption contributes to the results' variation.

The CFD predicted pressure ratio values are in good agreement with the test bench results, as shown in Figure 6.2a. The average pressure ratio difference between the CFD and the test bench results of all operating points compared is approximately 0.36%. Based on the discussion above, one can conclude that the CFD model setup can be considered reliable for the additional studies below in the paper.

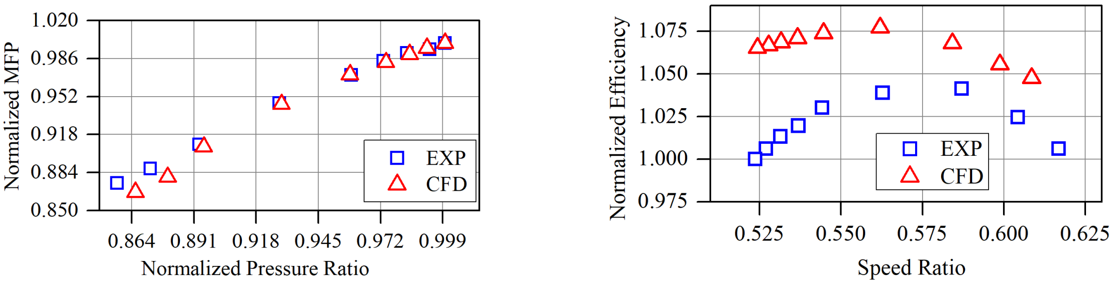

(a) (b)

Figure 6.2: Turbine test rig and CFD results: (a) pressure ratio vs mass flow parameter, and (b) speed ratio vs isentropic efficiency

6.4.2 Turbine Performance at Equal, Unequal and Partial Admissions

Three critical turbine operating cases are selected to study the turbine's uneven flow at three different mass flow rate values. The first one is the low-speed low-load case, with a lower mass flow rate than the turbine design point. The pressure ratio across the turbine for the first case considered is around 1.256 at full admission. The second case is where the turbine operates near the best efficiency point. At this condition, the turbine's isentropic efficiency is close to the optimum value at a pressure ratio value of 2.752 at equal admission. The third case is where the turbine mass flow is considerably higher than the design point flow rate. At this condition, due to high turbine backpressure, the turbine inlet pressure value is significantly higher than the design point value with a pressure ratio value of 2.124 at equal admission.

The turbine performance is studied at equal (full) admission where both inlets will have 50% of the total turbine mass flow rate. In addition to the full admission condition, three uneven flows are considered by increasing the mass flow rate into one of the volute inlets to have 70%, 90%, and 100% of the total turbine mass flow share. The four volute inlet flow proportions provide a simplistic simulation of the effect of different EGR rates when EGR is taken from one side of the engine.

Figure 6.3 - 6.5 show the uneven flow admission effect on turbine performance for the three flow cases considered for the study. The equal admission values are used to normalize each flow case performance parameter at unequal admissions. Figure 6.3a - 6.5a show that the normalized

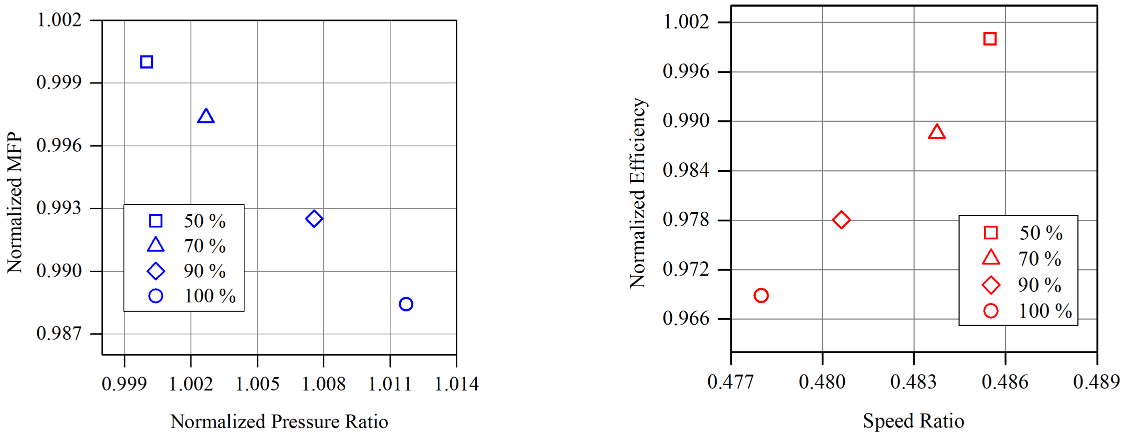

(a) Pressure ratio vs mass flow parameter (b) Speed ratio vs isentropic efficiency

Figure 6.3: Effect of equal and unequal admissions on turbine performance for low mass flow rate case

pressure ratio values increase linearly with a drop in normalized MFP values when the unevenness in the flow admission increases. On the contrary, the normalized efficiency values dropped linearly with a decrease in speed ratio as the inlet flow unevenness increases, as shown in Figure 6.3b - 6.5b. Both changes in normalized pressure ratio and normalized efficiency values from equal admission values increased with an increase in the turbine mass flow rate.

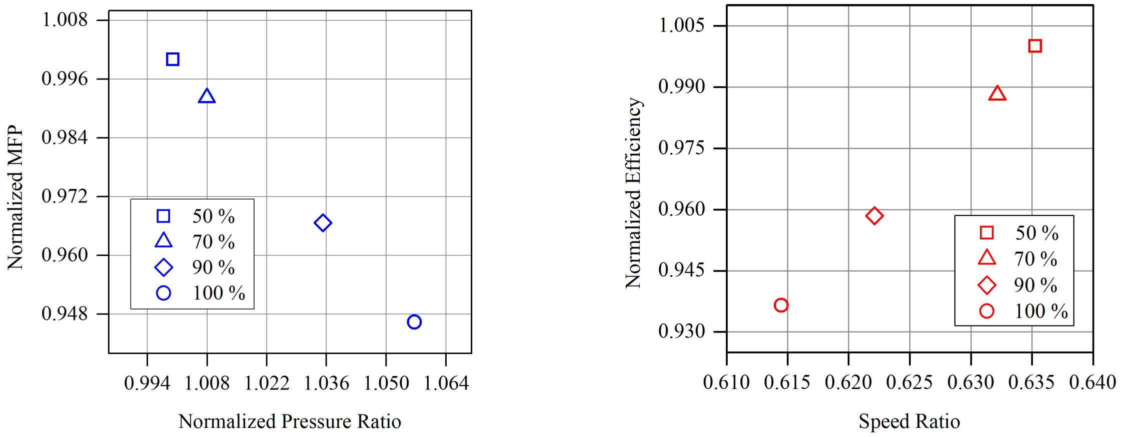

(a) Pressure ratio vs mass flow parameter (b) Speed ratio vs isentropic efficiency

Figure 6.4: Effect of equal and unequal admissions on turbine performance for mid mass flow rate case

The decline in efficiency at uneven flows can be explained by the non-uniform circumferential static pressure distribution at the volute to nozzle interface, as shown in Figure 6.6a. At even flow

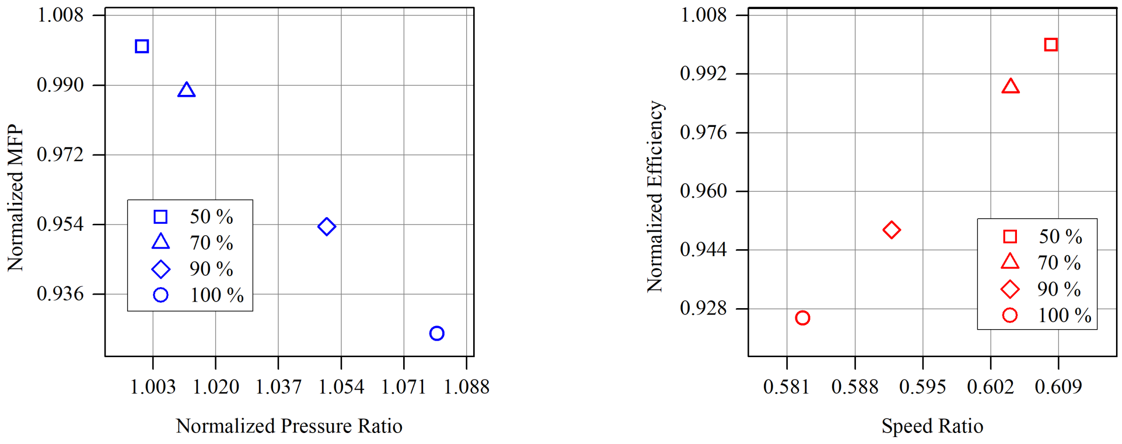

(a) Pressure ratio vs mass flow parameter (b) Speed ratio vs isentropic efficiency

Figure 6.5: Effect of equal and unequal admissions on turbine performance for high mass flow rate case

(50%), the static pressure spikes at nine points corresponding to the nine nozzle inlet blade tips. Since the incoming flow from the volute is incident to the nozzle blade tips, the flow static pressure increases as the fluid dynamic pressure drops. Figure 6.6a also shows that the static pressure value drops mid-way between two successive blades. Overall, even flow static pressure's circumferential distribution resembles a sinusoidal wave that peaks at the inlet nozzle blade tips and valleys mid-way between two succeeding nozzle blades. At uneven flows, the circumferential static pressure distribution becomes non-uniform as the volute inlet-1 flow increases (around circumferential angle 220) while the volute inlet-2 flow decreases. The non-uniformity of the static pressure increases with a further rise in the uneven flow between the two volute inlets. The non-uniform static pressure distribution at the nozzle inlet is amplified at the nozzle outlet, as shown in Figure 6.6b. The pressure distribution at the nozzle outlet (impeller inlet) peaks at uneven flows in an extended circumferential angle range between 250° - 325° in Figure 6.6b, than the nozzle inlet pressure distribution that ranges between 200° - 230° in Figure 6.6a. The pressure distribution plots in Figure 6.6b justify the choice of employing a full impeller simulation instead of a single passage. A single passage simulation with a periodic boundary condition would not represent the actual circumferential pressure variation into the impeller at uneven flows.

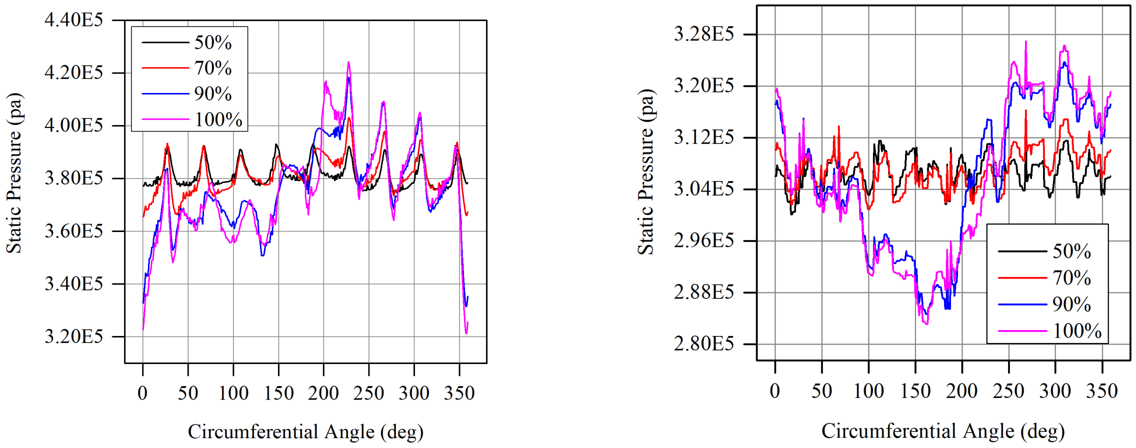

(a) Volute exit (Nozzle inlet)

(b) Nozzle exit (Impeller inlet)

Figure 6.6: Circumferential static pressure distribution for mid mass flow rate case at volute and nozzle exits

6.4.3 Entropy Production

Local entropy production rate can measure the efficiency loss in turbomachines as it is directly related to the destruction of useful work. Denton [94] identified viscous effects in boundary layers and the mixing process, shock waves, and heat transfer across temperature differences as the turbomachines' main entropy sources. Greitzer et al. [95] formulated control volume entropy change rate per unit mass using thermodynamics conversations laws as given by:

$$T\frac{Ds}{Dt} = \dot{Q} - \frac{1}{\rho}\frac{\partial q_i}{\partial x_i} + \frac{1}{\rho}\tau_{ij}\frac{\partial u_i}{\partial x_j} \tag{6.6}$$

The $\dot{Q}$ term in Eq.(6.6); represents the heat generation rate inside the control volume under consideration. This term can be neglected as the study in this paper does not involve any internal heat formation process such as combustion. The second term on the right-hand side of Eq.(6.6) expresses the control volume heat change due to conductive heat fluxes, whereas the last term represents the system heat content change via shear dissipation of the flow's mechanical energy. The stress tensor term,τ_{ij}, in Eq.(6.6) for compressible flows is defined in Batchelor [96] as given by:

$$\tau_{ij} = \mu\left(\frac{\partial v_i}{\partial x_j} + \frac{\partial v_j}{\partial x_i}\right) + \lambda\frac{\partial v_k}{\partial x_k}\delta_{ij} \tag{6.7}$$

The second term on right side of Eq.(6.7), represents the energy dissipation during volumetric dilatation. This term is considered negligible for most compressible flows as it has small magnitudes except in special flow cases such as shock waves where the density changes in extremely narrow gaps [97, 98].

Direct CFD computation of the instantaneous entropy generation rate in Eq.(6.6) is only possible if DNS models are utilized. In this paper, the RANS CFD approach is used to solve Eq.(6.6) by splitting the instantaneous values into time-mean and fluctuating parts. Such Reynolds decomposition of Eq.(6.6) is discussed in Moore and Moore [97] by modeling the fluctuating viscous dissipation terms using eddy viscosity. More recently, Kock and Herwig [99] derived the time average and fluctuating components of Eqn.(6.6) using a similar approach to Moore and Moore [97]. In their derivation, the $k - \epsilon$ turbulence model is used to estimate the entropy production caused by turbulent dissipation. The local entropy production rate per unit volume is given by:

$$\begin{aligned}\dot{S}_{PRO} = \frac{\mu}{\overline{T}} \Bigg[& 2\left\{ \left(\frac{\partial \overline{u}}{\partial x}\right)^2 + \left(\frac{\partial \overline{v}}{\partial y}\right)^2 + \left(\frac{\partial \overline{w}}{\partial z}\right)^2 \right\} + \left(\frac{\partial \overline{u}}{\partial y} + \frac{\partial \overline{v}}{\partial x}\right)^2 \\ & + \left(\frac{\partial \overline{u}}{\partial z} + \frac{\partial \overline{w}}{\partial x}\right)^2 + \left(\frac{\partial \overline{v}}{\partial z} + \frac{\partial \overline{w}}{\partial y}\right)^2 \Bigg] \\ & + \frac{\rho \epsilon}{\overline{T}} + \left(1 + \frac{\alpha_t}{\alpha}\right) \frac{\kappa}{\overline{T}^2} \left[\left(\frac{\partial \overline{T}}{\partial x}\right)^2 + \left(\frac{\partial \overline{T}}{\partial y}\right)^2 + \left(\frac{\partial \overline{T}}{\partial z}\right)^2 \right]\end{aligned} \tag{6.8}$$

The thermal diffusivity term in Eqn.(6.8) is defined as ratio of turbulent viscosity to turbulent Prandtl number, $\alpha_t = \mu_t/(\rho.Pr_t)$. The turbulent Prandtl number,Pr_t can be calculated using correlations or assumed constant. Ansys Fluent [100] uses a value of 0.85 value at all conditions while Palenschat et al. [90] set Pr_t value to one. Various correlations are found in literature [101, 102, 103] to define the turbulent Prandtl number, Pr_t. For this study, the correlation by Kays and Crawford [103] is used as given by:

$$Pr_t = \frac{1}{\left\{ 0.5882 + 0.228\left(\frac{\nu_t}{\nu}\right) - 0.0441\left(\frac{\nu_t}{\nu}\right)^2 \left[1 - exp\left(\frac{-5.165}{\frac{\nu_t}{\nu}}\right)\right]\right\}} \tag{6.9}$$

Every term in Eq.(6.8) and Eq.(6.9) can be evaluated in CFD post-processing stage. To locate entropy production sources, the computational domain divided into nine sub-regions by following similar approach by Abel et al. [104] and Palenschat et al. [90] as shown in Figure 6.7. The impeller region is divided into four sub-regions: the inlet, the passage pressure side (PS), the passage suction side (SS), and the tip. The nozzle is split into two sub-regions: the nozzle passage and the nozzle exit. Similarly, the diffuser is partitioned into the tip and core passage sub-regions.

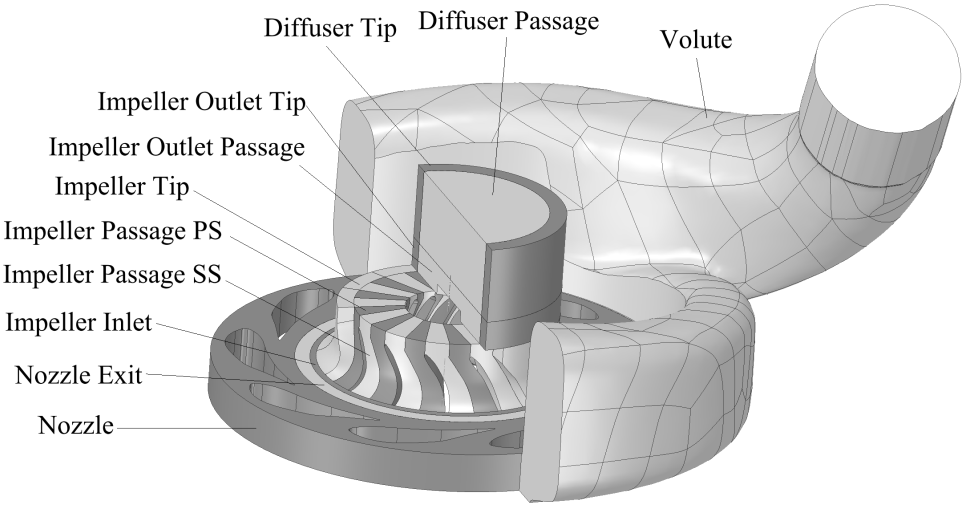

Figure 6.7: Sub-region decomposition of the CFD model for numerical estimation of the local entropy production rate

The local entropy production rate within each sub-region in Figure 6.7 is estimated by volume integration of Eq.(6.8) over each sub-volume. Values from the same sub-region category are then added to each other to determine the total entropy production rate per sub-region. A StarCCM+ java macro file is utilized to automate the whole process.

The local entropy production rate is highly grid dependent [90]. A separate grid sensitivity analysis is completed by considering the entropy ratio defined as the entropy production rate calculated by Eq.(6.8) divided by the entropy production rate estimated via Gibb's entropy equation. The ratio asymptotically approaches one as the computational domain grid gets finer [90, 104]. A final mesh with approximately 50 million elements is used in this study to estimate the local entropy production rates for all admissions cases at the three engine loads with an average entropy ratio value of 0.72. As discussed in Denton [94], rapid velocity changes at near wall surfaces are responsible for entropy production in the inner boundary layers. Consequently, to accurately estimate the entropy production in the boundary layers, the near-wall CFD grids are adjusted to keep y^+ values well below one.

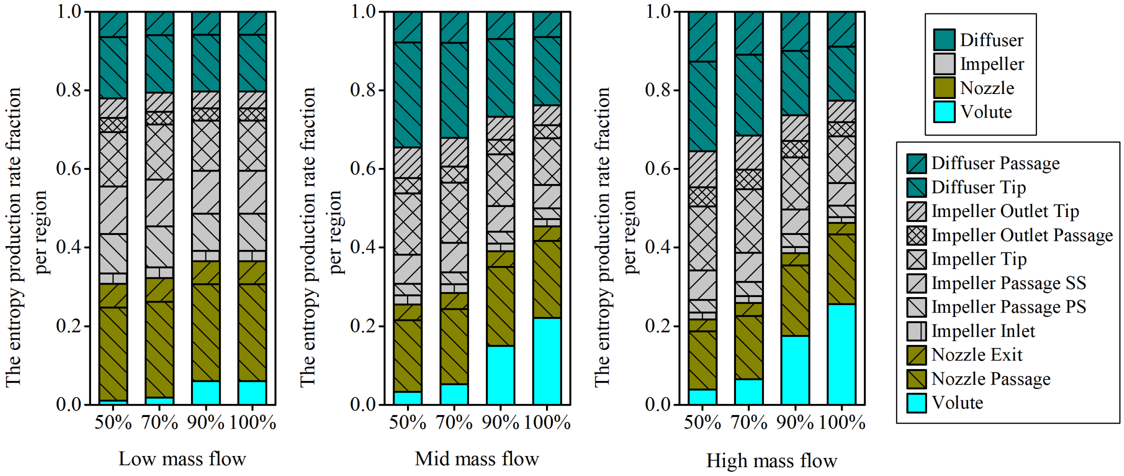

Figure 6.8: Fraction of the entropy production rate per region for three mass flow rate cases with one equal and three unequal admissions for each flow case

At equal admission (50 %), the most substantial entropy generation rate comes from the impeller for all the three engine load cases, as shown in Figure 6.8. Out of the six impeller sub-regions, the impeller tip regions are the primary sources of entropy at all turbine mass flow and admission cases. Between the leading and trailing edges of the turbine, losses related to the impeller's leakage flow from the high-pressure side to low-pressure through the blade tip gap dominate the total tip losses. In the tip region, the entropy production on the impeller blades' suction side is higher than the pressure side because of the tip leakage mixing with the main flow. The tip leakage also builds up flow separation losses on the low-pressure side by transporting the slow-moving separation bubbles from the boundary layers in tip gap regions [94, 105]. In all twelve cases considered, the impeller suction side has a higher loss contribution than the pressure side, irrespective of the mass flow rate or the admission values as displayed in Figure 6.8.

Figure 6.10 and Figure 6.9 show the streamwise distribution of the local entropy production rate per volume in logarithmic scale for full and partial admission cases at the three engine load cases considered for the study. Both figures show that the tip loss increases with the mass flow rate.

At at equal admission, the tip loss accounts for 40%, 59%, and 56% of the total impeller loss for low, mid mass, and high mass flow rate cases, respectively. At the two moderate to high turbine mass flows, the tip region losses are localized at a smaller area near the leading edge of the turbine and cover a wider area of the tip region near the trailing edge of the turbine as demonstrated in Figure 6.10b, Figure 6.10c, Figure 6.9b, and Figure 6.9c. The tip losses are less dependent on the three engine load cases' admission value as the loss magnitude increases by small margins when the admission values vary from full to partial.

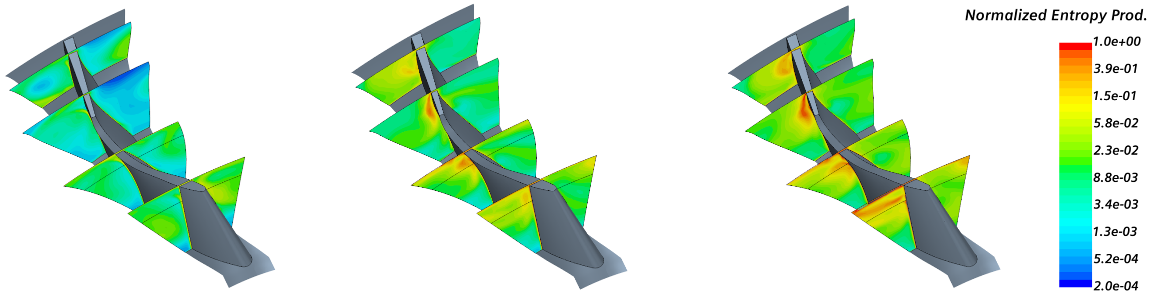

(a) Low mass flow (b) Mid mass flow (c) High mass flow

Figure 6.9: Normalized entropy production rate per volume at partial load for the three flow rate cases

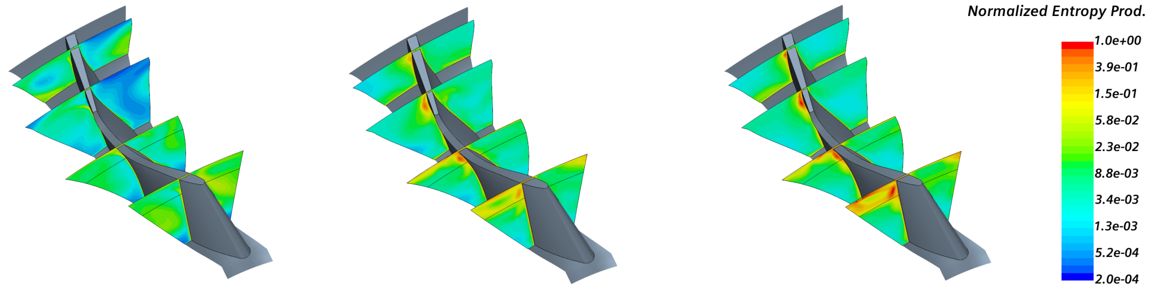

(a) Low mass flow (b) Mid mass flow (c) High mass flow

Figure 6.10: Normalized entropy production rate per volume at full load for the three flow rate cases

Downstream of the turbine, the diffuser losses contribute a significant amount to the overall turbine losses. The exit flow accounts for 22%, 34.5%, and 35.5% of the overall turbine loss at low, mid, and high mass flow rate cases at equal admission. The diffuser flow losses are less dependent on the admission values as the flow mixing in the turbine impeller exit dumps the flow admission effects. The diffuser entropy production rate at each three flow cases varied by an insignificant amount for all four admission cases at each flow case. Due to a substantial increase in the local entropy production rate in the nozzle and volute regions at partial admissions, the overall turbine loss portion from the diffuser decreased to 19%, 23.8%, and 22.6% at low, mid, and high mass flow rate cases, respectively.

The uneven turbine inlet flows affected the volute performance considerably for all three engine loads. At low-speed engine load with the smallest turbine inlet mass flow, the volute contribution to overall turbine losses jumped from 1% to 9% when the admission value changes from full to partial. The uneven flow effect on the volute performance is witnessed more at higher mass flow rate cases. At the two moderate to high mass flow cases, the volute contribution to overall turbine losses jumped from 3% to 22%, and 4% to 26%, respectively, when the admission value changes from equal to unequal as shown in Figure 6.8.

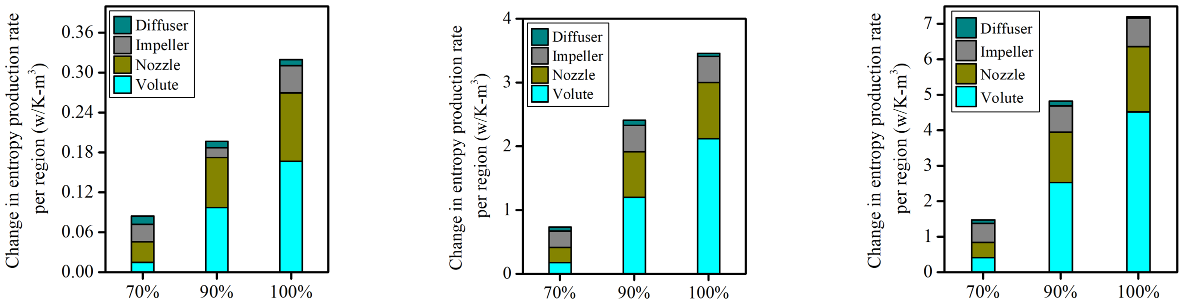

(a) Low mass flow

(b) Mid mass flow

(c) High mass flow

Figure 6.11: Unequal admission's change in entropy production rate per region from equal admission for three flow rate cases

Figure 6.11 shows the change in entropy production rate per region between unequal and equal admissions for three flow cases. The figure shows the change in entropy production rate from equal admission increases with the unevenness of the flow distribution for all three cases considered. Figure 6.11 also reveals that the unequal admission affected the volute flow the most out of the four regions. In each flow case considered, in partial admission (100%-0%) cases, the volute's entropy production rate change accounts for more than 50% of the total turbine's change from equal admission values.

The normalized local entropy production rate per volume at nozzle mid-span is plotted in Figure 6.12 in logarithmic scale for equal (50% - 50%) and unequal (100% - 0%) admission cases at the mid mass flow rate case. The volute local entropy production rate at equal admission is minimal except for areas near the two tongues, as presented in Figure 6.12a. At unequal admissions, the local entropy production increases measurably in half of the volute circumferential segment since there is no flow from the volute inlet that feeds the segment's flow, as shown in Fig. 6.12b. When the volute flow from only one inlet (volute inlet 1 in Figure 6.12) expands in the entire volute circumference at unequal admissions, in half of the volute segment, the flow velocity decelerates, and local secondary flows emerge, intensifying the local entropy production rate. The nozzle losses at equal admission of the low mass flow rate case contribute approximately 30% of the overall turbine assembly losses. At moderate to high turbine mass flow conditions, the nozzle loss contribution lowered to 22% and 18%, respectively, at equal admission as presented in Figure 8. Uneven flow at the turbine inlets affects the nozzle performance by altering the nozzle blades' flow incidence angle and the flow pressure distribution. Figure 6.12b shows that entropy production increased considerably on the nozzle flow channels close to the volute inlet2 tongue where there is no flow at partial admission.

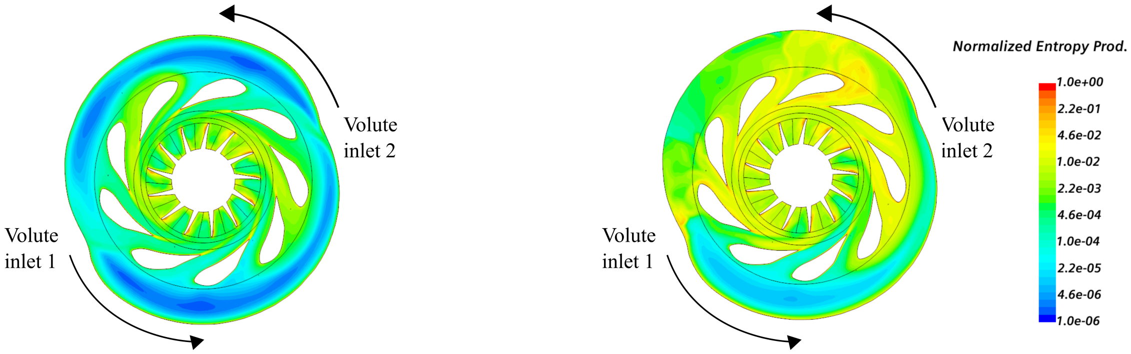

(a) Equal admission (50%-50%)

(b) Unequal admission (100%-0%)

Figure 6.12: Normalized local entropy production rate per volume at nozzle mid span for high mass flow rate case

CHAPTER 7

SINGLE AND TWIN-SCROLL VOLUTE DESIGN AND OPTIMIZATION

7.1 Introduction

Volute in turbocharger turbines convert the static enthalpy of the engine exhaust gas into kinetic energy and guides the resulting flow around the turbine circumference. The pressure and velocity are expected to remain uniform around the periphery of an efficient volute.

Initial volute designs follow one-dimensional mass and free vortex conservation equations to fix the volute dimensions at different azimuth angles. In the preliminary volute design approach, the flow exiting the scroll is assumed to have a uniform pressure and flow angle distribution at each nozzle flow channel. Despite the simplified one-dimensional design approach assumptions, numerous experimental studies [106, 107, 108, 109] have shown that flow inside volute channels is three-dimensional and does not follow the conservation of free vortex equations over its entire circumference. Due to the interaction between the volute and nozzle blade, the distribution of flow mass, pressure, and incidence angle vary between the nozzle flow channels.

Several researchers [110, 111, 112] have also employed computational methods to investigate the three dimensional nature of the volute flow in vaneless and vaned turbocharger turbine volutes. Lee et al. [110] conducted a steady-state and pulsed flow numerical analysis of the secondary flows in vaned turbine volutes using symmetrical volutes with circular cross-sections. Their steady-state results show vortices in volute cross-sections up to 90° from the throat. In contrast, the secondary flow structures disappear at higher azimuth angles due to the reduced volute section area. Their pulsed flow analysis shows that the secondary flow is time dependent.

Yang et al. [111] compared secondary flow structures in two vanless turbocharger turbine volutes with different aspect ratios under steady and pulsating flow conditions. Different secondary flow structures are observed as the large aspect ratio volute operates at transient and steady flows. Compared to the volute with a smaller aspect ratio, the one with a larger aspect ratio responded slowly to pulsating flows because of the increased inertia of the vortices.

The effect of scroll cross-sectional shape on volute secondary flow development and overall turbine efficiency has been examined by several researchers [113, 114, 115, 116]. The impact of tongue design on the performance of radial turbines was investigated by Suhrmann et al. [113], who recommended a tongue geometry with a small tongue radius and tongue angle values for greater turbine efficiency. Conversely, they suggested that a larger tongue angle would help reduce wheel blade fatigue failures. Three volute aspect ratio values were investigated under steady and pulsating flow conditions by Lee et al. [114] to determine how volute shape affects vanless mixed flow turbine performance. They concluded that the volute aspect ratio significantly impacts the stage MFP value while the overall turbine efficiency change for the three compared volute shapes is minimal.

The final volute shape depends on the geometry parameters at the preliminary volute design stage. As discussed in the literature above, the scroll shape directly impacts the secondary flows in the volute. The secondary flows negatively impact the performance of the volute and thereby the overall turbine efficiency. This chapter discusses the design of single-scroll and twin-scroll turbine volutes and compares the performance of each of the two scroll cases with dual-entry scrolls. Moreover, the effect of three crucial volute geometry parameters - tongue angle, tongue clearance, and volute shape - on the performance of a turbocharger turbine with nozzle blades is discussed. The study also explains how secondary flows from volute have a direct relationship with the three design parameters.

7.2 Volute Design Procedure

Different authors propose various volute design methods [117, 118, 119, 120] for centrifugal machines. The two most common design procedures adopted by the industry are the Stepanoff [118] and Pfleiderer [117] methods. In the Stepanoff volute design procedure, the mean velocity of the flow in the volute passage is maintained constant at the design point to obtain a uniform pressure distribution around the impeller circumference. The Pfleiderer method assumes the volute housing losses are minimized if the volute is diminished by the conservation of the flow angular momentum.

Both methods are applied to design a pump volute resulting in little pressure head difference between consecutive volute sections [121].

For a simple volute flow model, where secondary flows are neglected, a free vortex centered at the turbine axis is a good approximation, as shown in Eq.(7.1). The free vortex model gives a velocity profile that decreases with radius, as shown in Figure 7.1.

$$C_\theta r = constant = K \tag{7.1}$$

The free vortex assumption of the volute flow is further modified by considering the swirling flow at any azimuth angle [122] as given by Eq.(7.2).

$$C_\theta r^m = constant = K \tag{7.2}$$

Another correlation used for volute flow angular momentum accounts for the influence of wall friction inside the volute. A Swirl coefficient (S) is introduced to consider the role of wall friction on the angular momentum conservation between volute inlet and outlet. Japikse et al. suggested the swirl coefficient value to fall between 0.85 and 0.95 [6]. Eq.(7.3) relates the volute angular momentum conservation between volute inlet and outlet using a swirl constant S.

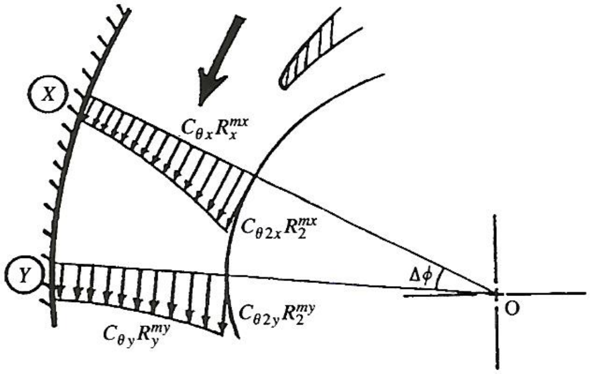

Figure 7.1: Volute velocity profile from inner to outer radius [122]

$$C_{\theta 1} r_1 = S C_{\theta 2} r_2 \tag{7.3}$$

Whitfield et al. [122] defined an angular momentum dissipation term, S_{xy}, between two successive volute sections (section x and y in Figure 7.1) in terms of the overall dissipation parameter, S, as shown in Eq.(7.4).

$$S_{xy} = 1 - \frac{\Delta\psi}{2\pi}\frac{C_1 r_1 \sin\alpha_1}{C_x r_x \sin\alpha_x}(1 - S) \tag{7.4}$$

Turton [121] suggests the effect of friction is neglected in volute design steps as it has little impact on the volute cross-section areas. The mass flow through any cross-section plane at azimuth angle ψ is:

$$\dot{m}_\psi = \rho_\psi A_\psi C_{\theta\psi} \tag{7.5}$$

For a uniform distribution of mass flow round the volute,

$$\dot{m}_\psi = \dot{m}\left(1 - \frac{\psi}{2\pi}\right) + \dot{m}_R \tag{7.6}$$

where $\dot{m}$ is the total mass flow rate. The recirculation mass flow rate $\dot{m}_R$ ranges from 0 to 5% of the design mass flow rate [122]. The area to centroid radius ratio for zero tongue recirculation is given by Eq.(7.7).

$$\frac{A_\psi}{r_\psi} = \frac{\dot{m}}{\rho_\psi K}\left(1 - \frac{\psi}{2\pi}\right) \tag{7.7}$$

where r_ψ is the radius of the centroid of the section at azimuth angle ψ. To achieve a uniform amass flow distribution around the volute, for the case of incompressible flow or where density variations are relatively small, the ratio A_ψ/r_ψ must be a linear function of the azimuth angle. Assuming uniform flow around the exit periphery of the volute, the angle of the flow at exit is given by:

$$tan\ \alpha_2 = C_{\theta 2}/C_{m2} \tag{7.8}$$

Substituting for the velocities $C_{\theta 2}$ and C_{m2} form the free vortex and continuity equations,

$$C_{\theta 2} = C_{\theta 2} r_1/r_2 = C_1 r_1/r_2 \tag{7.9}$$

$$C_{m2} = \frac{\dot{m}}{\rho_2 A_2} = \frac{\rho_1 A_1}{\rho_2 A_2} C_1 \tag{7.10}$$

which gives,

$$tan\ \alpha_2 = \frac{\rho_2}{\rho_2}\frac{A_2/r_2}{A_1/r_1} \tag{7.11}$$

Normally the volute exit area is fixed by nozzle or rotor. The exit flow angle is determined by the choice of inlet area and radius. The value of A/r decreases linearly with azimuth angle for uniform exit conditions, as shown in Eq.(7.7). Choice of A/r at the inlet determines the exit flow angle, as shown in Eq.(7.11). The total enthalpy at inlet, h_{01}, is calculated from the reference specific heat value and inlet total temperature values as:

$$h_{01} = C_{p_{ref}} T_{01} \tag{7.12}$$

The total entropy at the volute inlet is calculated using total temperature and pressure values of the air as:

$$s_{01} = s_{ref} + C_{p_{ref}} \ln\left(\frac{T_{01}}{T_{ref}}\right) - R_{ref} \ln\left(\frac{p_{01}}{p_{ref}}\right) \tag{7.13}$$

The governing equations Eq.(7.1) - Eq.(7.13) are used to define the single-scroll volute geometry as discussion in Section 7.3.

7.3 Single-scroll Volute Geometry Definition

Before a detailed design of a volute, the preliminary component sizing of the volute must be completed. Further modification and optimization of the components are followed, employing one-dimensional, numerical, and experimental methods. This procedure helps to analyze and decide the final component dimensions and performance limits.

Volute detail design thus starts from preliminary component size parameters of the turbine impeller and the nozzle, if any. For this study, the impeller and variable geometry nozzle blade dimensions are pre-known. The initial stage design specifications used for the volute design include the flow and geometry variables such as stage mass flow rate, stage inlet total temperature, stage inlet total pressure, volute exit(nozzle inlet) tangential velocity, volute exit(nozzle inlet) radius, and the volute exit (nozzle inlet) passage width. The volute design parameters are expressed in dimensionless and pseudo-dimensionless values in Table 7.1. The nozzle inlet radius (r_2) and nozzle inlet passage width (b_2) values are normalized by the impeller inlet radius (r_4) values.

Table 7.1: Volute design flow and geometry parameters

Design variable	**Value**
Mass flow parameter $\left(MFP = \dot{m}\sqrt{T_{01}}/p_{01}\right)$	0.0216 $(kg/s \cdot \sqrt{K}/kPa)$
Pressure ratio $(PR = p_{01}/p_{s5})$	2.78 (-)
Reduced rotational speed $\left(N_{red} = N/\sqrt{T_{01}}\right)$	3,359.29 $(rpm/\sqrt{K})$
Nozzle inlet tangential velocity $(C_{\theta 2})$	63.5 (m/s)
r_2/r_4	2.0 (-)
b_2/r_4	0.3427 (-)

Single scroll gas turbine volutes can be classified as an external and internal one. The external volutes are generally preferred over the internal ones as they provide a higher tangential velocity for the same volute inlet velocity. On the other hand, the internal volutes have a compact shape [123]. Common volute cross-sectional shapes include circular, elliptical, rectangular, and overhang (internal) volutes[124, 125]. An external volute with an elliptical cross-section is used to design the single inlet volute. The volute cross-section comprises three-quarters of an ellipse and a rectangle with width and height values defined by the ellipse major and minor radii values, as shown in Figure 7.2.

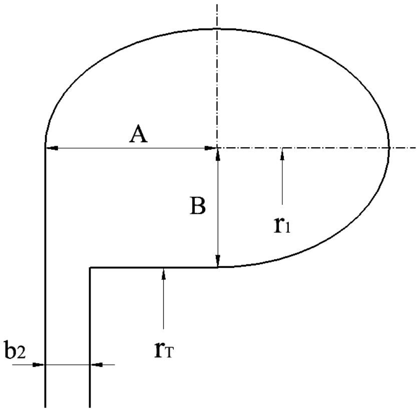

Figure 7.2: Single scroll elliptical shape external volute adapted from Aungier [123]

The scroll throat dimensions are evaluated iteratively, assuming the flow density variation in the scroll inlet duct is minimal. The aspect ratio of the ellipse, AR, is given as the major to minor radius ratio. Aungier [123] suggested AR value ranges between 0.75 and 1.5. In the single scroll preliminary design, the throat radius value, r_T, is fixed to be 1.05 of the nozzle inlet radius, r_2. The volute cross-section area is calculated by Eq.(7.14).

$$Area = (3\pi/4 + 1) \times A \times B \tag{7.14}$$

The iterative procedure starts by setting the initial throat centroid radius equal to the throat radius, r_T. The conservation equations, Eq.(7.3) and Eq.(7.5), and scroll geometry definition provide a new estimate for the centroid radius. The iterative procedure ends when the centroid radius converges sufficiently. The flow chart in Figure 7.3 describes the steps and equations used to estimate the throat profile.

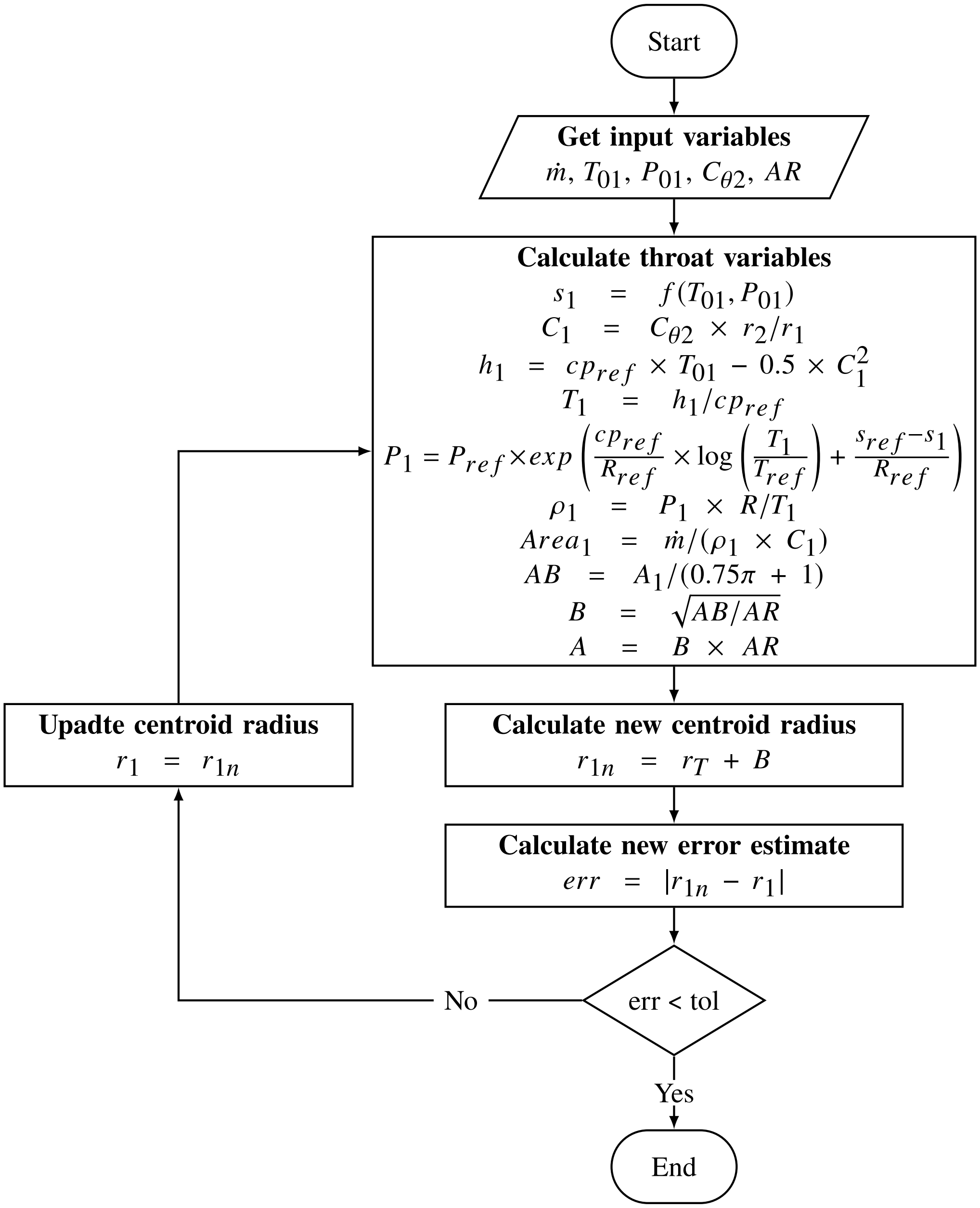

Figure 7.3: Procedure to estimate the volute throat geometry and flow variables

The dimensions of the volute section profiles at azimuth angles from the throat (0°) to the last volute section (360°- θ_{ton}) are set using the volute cross-section area and A/r definitions. The tongue angle, θ_{ton}, is a design parameter that ranges from 10° to 30°. The density value at each volute cross-section is held constant, equal to the throat density value. The minor ellipse radius at azimuth angle, ψ, is calculated by Eq.7.15.

$$B_{\psi} = \frac{k}{2 \times AR} + \sqrt{\left(\frac{k}{2 \times AR}\right)^2 + \frac{k \times r_T}{AR}} \tag{7.15}$$

In Eq.(7.15), the k constant is defined by combing the volute cross-section area definition given by Eq.(7.14) and the A/r ratio value defined by Eq.(7.7).

$$k = \frac{\dot{m}}{\rho_{\psi} \times C_1 \times r_1}\left(1 - \frac{\psi}{2\pi}\right) \times \left(\frac{1}{3\pi/4 + 1}\right) \tag{7.16}$$

The major ellipse radius of the volute cross-section, A_{ψ}, is calculated from the ellipse aspect ratio, AR, and the minor ellipse radius, B_{ψ}. Since the major and minor ellipse radii values are determined, the volute cross-section shape is fully defined at azimuth angle, ψ. Figure 7.4 shows the A/r and section profile variation with azimuth angle for ten volute cross-sections at 1.25 ellipse aspect ratio. A java macro script file is used to loft the volute cross-sections and create the three-dimensional scroll geometry in StarCCM+.

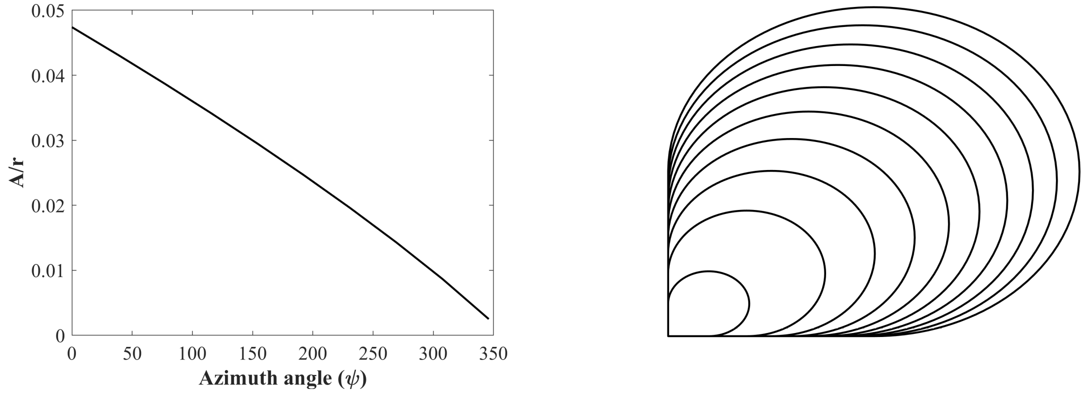

(a)

(b)

Figure 7.4: Plots of A/r variation with azimuth angle ψ (7.4a) and volute cross-sections at different azimuth angles (7.4b)

The volute inlet pipe can be considered as a tapering pipe with a pipe inlet area larger than the volute throat area. Since the flow accelerates in the pipe, a slight pressure drop is expected at the pipe outlet. Flow separation is not usually expected in converging pipes, making pipe taper angle value less significant than in diverging pipes. The pipe taper angle affects the pipe flow friction loss as it sets the overall shape of the pipe. The throat area, pipe taper angle, and pipe inlet area values determine the pipe length.

7.4 The CFD Methodology

In this study, all computational results have been obtained with StarCCM+, a commercial finite-volume solver. Reynolds averaged Navier-Stokes (RANS) steady-state equations are utilized to assess the turbine performance at all operating conditions. The complete CAD model for the computational study includes the single-entry volute, the nozzle, the turbine wheel, and the diffuser.

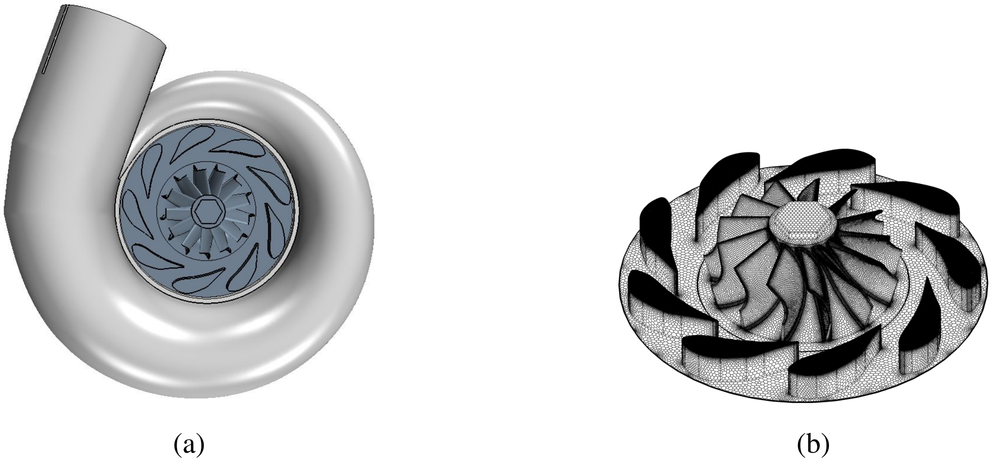
(a) (b)

Figure 7.5: (a) full computational domain , and (b) Nozzle and rotor blade surface mesh

Polyhedral cells are selected for the flow regions far from the wall, while prism cells with fifteen layers are used for the flow regions near the wall. In contrast to hex and tet elements, polyhedral cells with equivalent refinement levels have a higher face to element count ratio, which results in a faster computation [92]. A $y^+ \leq 5$ value is targeted for the first layer of prism cells nearest the wall to resolve the near-wall turbulence. In addition, a sufficient first layer thickness value also promotes suitable thickness propagation between near-wall and core flow regions.

In rotor blades, a constant blade tip-to-shroud gap of 0.4mm is applied. In both rotors and nozzles, the size of the local surface mesh is regulated to capture curvatures near the leading and trailing edges of the blades. The computational CAD model is displayed in Figure 7.5a, while Figure 7.5b shows the surface mesh of the rotor and nozzle blades. An evaluation of mesh sensitivity was carried out considering the change in impeller moment and isentropic efficiency quantities as a function of the number of elements in the computational model. The mesh sensitivity analysis follows a similar procedure to Gladio's[126], employing six meshes with the element count ranging from 2-6 million. The variation of the isentropic efficiency and impeller moment with the element count is displayed in Figure 7.6. This study uses meshes with approximately 3.5 million elements and a 2 mm base size for all steady-state results.

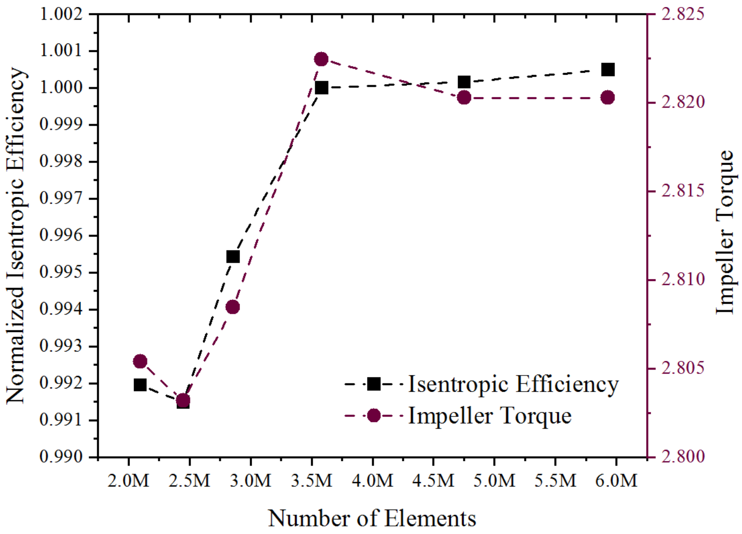

Figure 7.6: Mesh sensitivity study

Each of the simulations for turbine performance analysis is done using mass flow inlet and static pressure outlet boundary conditions. Double-precision StarCCM+ with the segregated flow solver is chosen over the coupled flow solver for faster convergence with marginal penalty prediction accuracy. All steady-state simulations in this study are based on the $k - \omega$ SST model with the re-attachment modification. $k - \omega$, a two-equation model based on turbulent eddy-viscosity relations, is widely used in turbomachinery simulations since it provides a good compromise between accuracy and robustness. By providing additional terms to the turbulence kinetic energy equation, the SST model's re-attachment modification improves the model's accurate predictions [92].

7.5 Single-scroll Volute Geometry Optimization

Even though one-dimensional methods are used to design the volute, the volute flow is fully three-dimensional with additional secondary flows superimposed on the main through flow. The secondary flows arise due to various volute design parameters such as the tongue angle, nozzle inlet to volute outlet clearance gap, and volute cross-sectional shape. Figure 7.7 shows the volute flow at different volute azimuth angles for near design operation. Local vortices near the tongue and non-uniform flow distribution at all volute sections are noticeable from the velocity plot. The non-uniform flow distribution is expected to intensify at off-design operating conditions. The effect of each volute design parameter is discussed in the subtopics below.

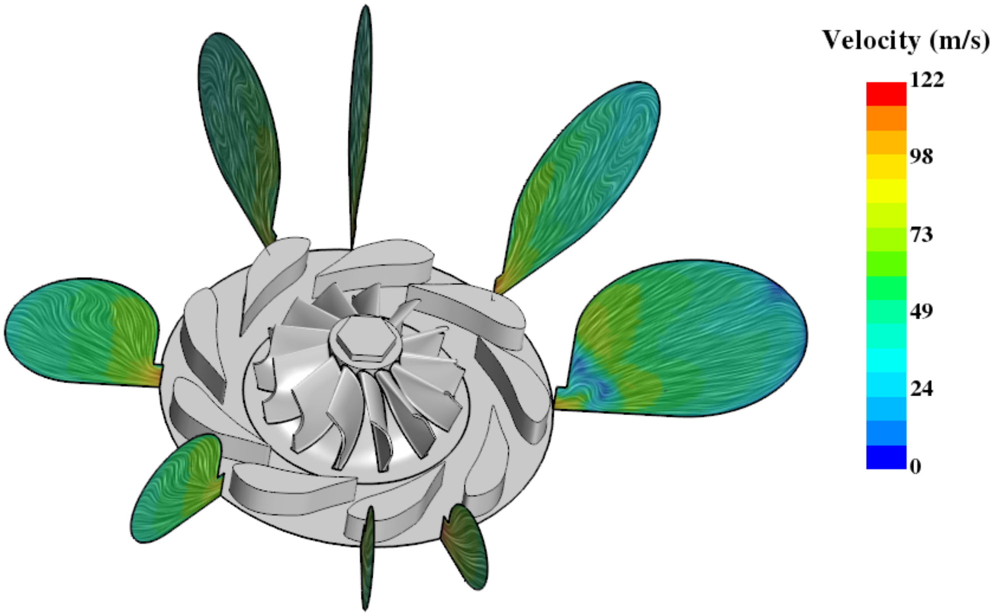

Figure 7.7: Flow velocity at different volute sections for near design operating condition

7.5.1 Effect of Volute Tongue Angle

The volute tongue is responsible for generating non-uniform flow around the circumferential outlet of the volute, altering the flow angle admitted to nozzle blades. Various researchers studied the effect of tongue geometry on a vaneless radial turbine performance [113, 127]. Hussain et al. [127] used an experimental investigation to find the optimum tongue angle for vaneless to be approximately 23°. This optimized tongue angle is suggested by considering the radial vortex development and while keeping a higher tangential velocity in the radial direction.

Five volute tongue angles between 10° and 30° are used to optimize the single-scroll geometry near design point flow conditions, as shown in Figure 7.8. Two performance parameters, namely, the isentropic turbine efficiency and volute pressure loss coefficient, are used to compare the volute performance at different volute tongue angles. The isentropic turbine efficiency is defined between volute inlet and diffuser exit enthalpy values as given by Eq.(7.17). The volute pressure loss coefficient is estimated by dividing the change in total pressure across the volute to the volute exit dynamic pressure, as defined in Eq.(7.18).

$$\eta_{TS} = \frac{h_{01} - h_{06}}{h_{01} - h_{6s}} \tag{7.17}$$

$$C_{PL} = \frac{P_{01} - P_{02}}{P_{02} - P_2} \tag{7.18}$$

In Eq.(7.17) and Eq.(7.18) subscripts (1), (2), and (6) represent the volute inlet, volute exit, and diffuser exit, respectively. The isentropic efficiency is maximized at a tongue angle close to 20°. In contrast, the pressure loss coefficient has the lowest value at a tongue angle near 15°.

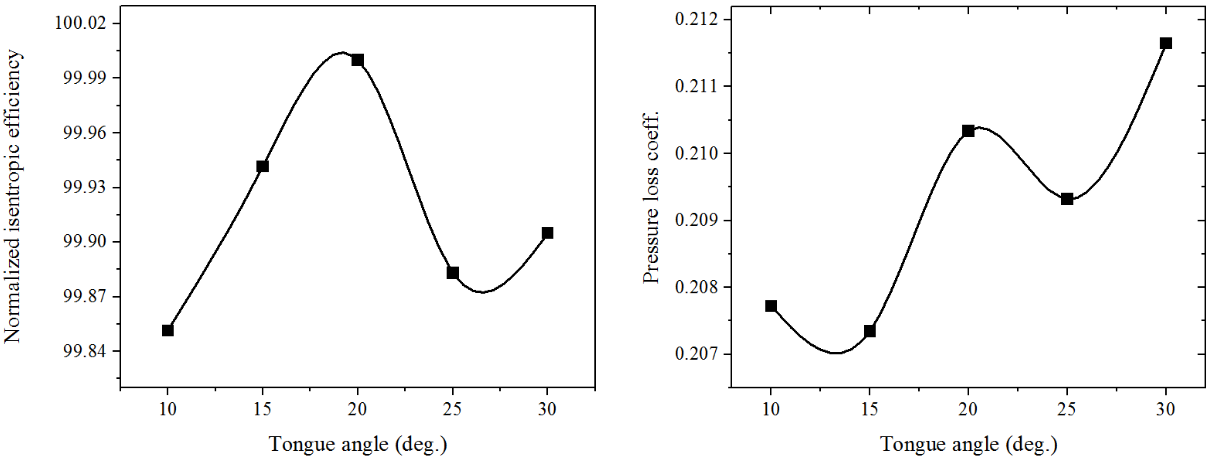

(a) (b)

Figure 7.8: Effect of volute tongue angle on the single-entry turbine isentropic efficiency (7.8a) and volute pressure loss coefficient (7.8b) near design point

Figure 7.9 shows the flow velocity distribution around the whole circumference of the volute-nozzle interface. The flow direction and magnitude depend on the nozzle blade position. Near the leading edge of the nozzle blade, the flow has a smaller magnitude (higher static pressure), and the flow direction is reversed. The flow then accelerates in the nozzle flow channel with a subsequent drop in static pressure. The static pressure distribution of the flow resembles a sinusoidal wave with a valley midway of the nozzle channel and the pick located at the leading edges of the nozzle blades. The lowest pressure valley is positioned at the last nozzle flow channel of the volute-nozzle interface before the tongue. An increase in tongue angle resulted in a further drop of the lowest static pressure around the volute-nozzle interface.

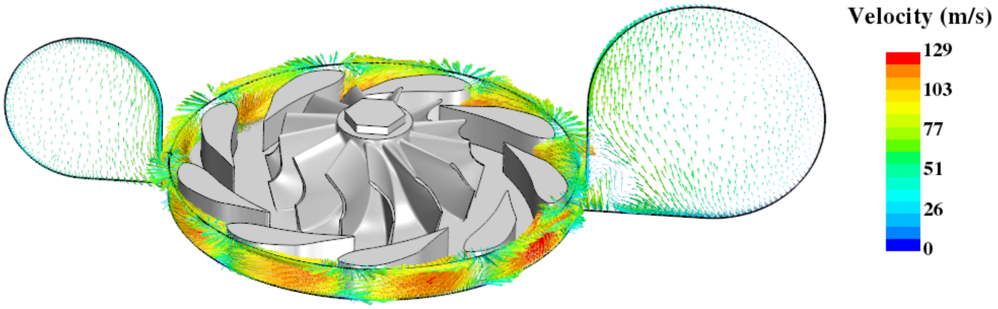

Figure 7.9: Flow velocity at different volute sections for near design operating condition

7.5.2 Effect of Volute Tongue Radius

The tongue radius has a significant impact on the volute performance. The one-dimensional volute design procedures discussed above show the volute cross-sectional area increases with the reduction in the tongue radius. Figure 7.10 shows the change in overall isentropic efficiency and volute pressure loss coefficient with the tongue radius. The isentropic efficiency increased while the pressure loss coefficient declined with the tongue radius.

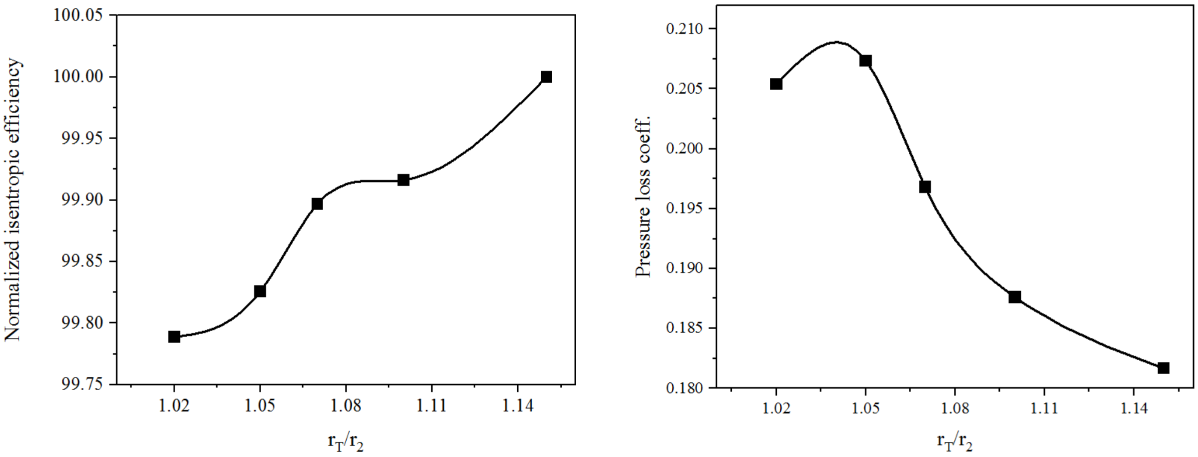

(a)

(b)

Figure 7.10: Effect of volute tongue radius on the single-entry turbine isentropic efficiency (7.10a) and volute pressure loss coefficient (7.10b) at near design point operation

The velocity vectors plotted in Figure 7.11 show that the flow exiting from the volute to the nozzle is further developed and uniform at increased tongue radius values. The flow velocity magnitude also decreased as the centroid radius of the volute sections increased. The packaging size limitation should be considered when deciding the final design tongue radius value.

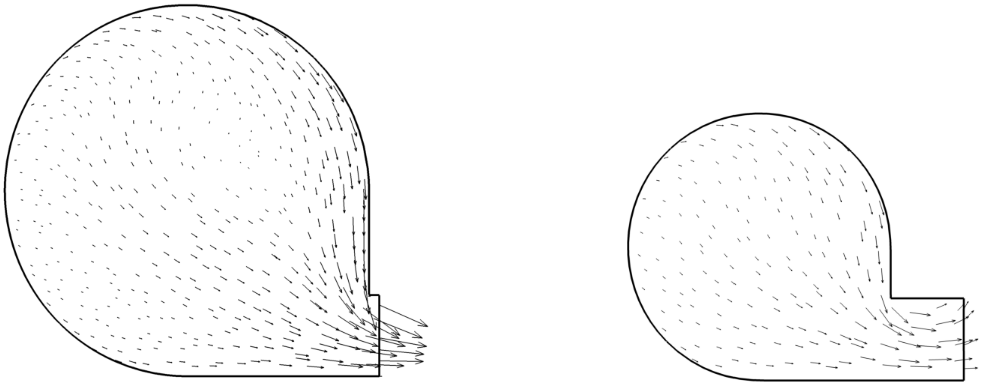

(a) Velocity vector at r_T/r_2 = 1.02

(b) Velocity vector at r_T/r_2 = 1.15

Figure 7.11: Volute flow velocity vector at 180° circumferential angle from the throat at near design point operation

7.5.3 The effect of Different Shapes of the Volute

Four ellipse aspect ratio values, ranging from 0.75 to 1.5, are used to study the effect of the volute cross-sectional shape on the performance of the single-entry turbine. The throat to nozzle inlet radius ratio of 1.15 and throat angle of 15° is used for all four cases. Figure 7.12 shows the four cross-section shapes with different aspect ratio values.

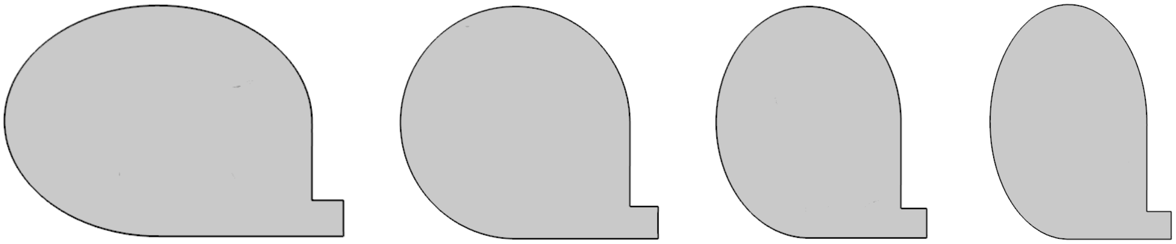

(a) AR = 0.75 (b) AR = 1.0 (c) AR = 1.25 (d) AR = 1.5

Figure 7.12: Four volute cross-sections with different ellipse aspect ratio values

The isentropic efficiency and the pressure loss coefficient variation for the four volute shapes is plotted in Figure 7.13. As shown in the figure, the isentropic efficiency value decreased with the volute aspect ratio increase. Contrarily, the volute pressure loss coefficient increased with the volute aspect ratio.

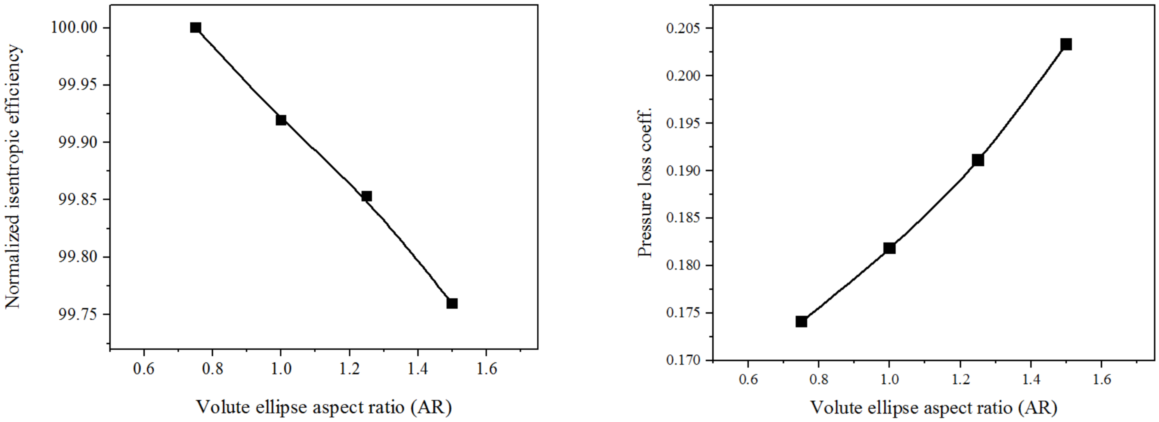

(a) (b)

Figure 7.13: Volute ellipse aspect ratio effect on the isentropic efficiency (7.13a) and pressure loss coefficient (7.13b)

The flow exiting the volute leaves tangentially, forcing the flow to turn 90° on the shroud side.

The abrupt turning of the flow creates a flow separation at the corner, causing a nonuniform flow to the nozzle inlet. Consequently, the volute exit flow will have its maximum value near the nozzle hub side while its value decreases near the nozzle shroud surface, as shown by the velocity vector plot in Figure 7.11. An enlarged volute aspect ratio increased the flow velocity before it turned 90°, slightly expanding the separated flow region in the volute to nozzle gap. The flow streamlines are plotted in Figure 7.14 and Figure 7.15 for volute crosssections with an ellipse aspect ratio of 0.75 and 1.50.

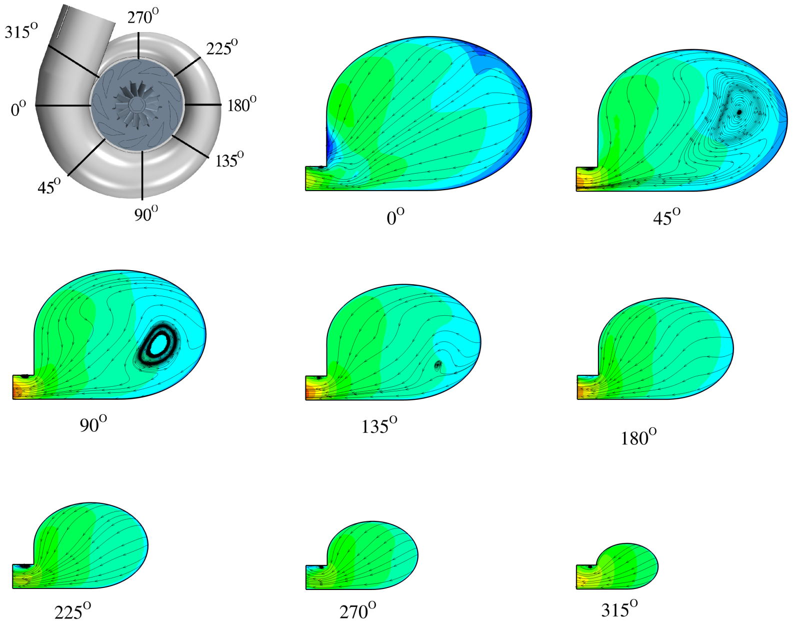

Figure 7.14: Velocity contour and streamline plots for asymmetrical, semi-elliptical scroll cross-sectional shape with AR = 0.75

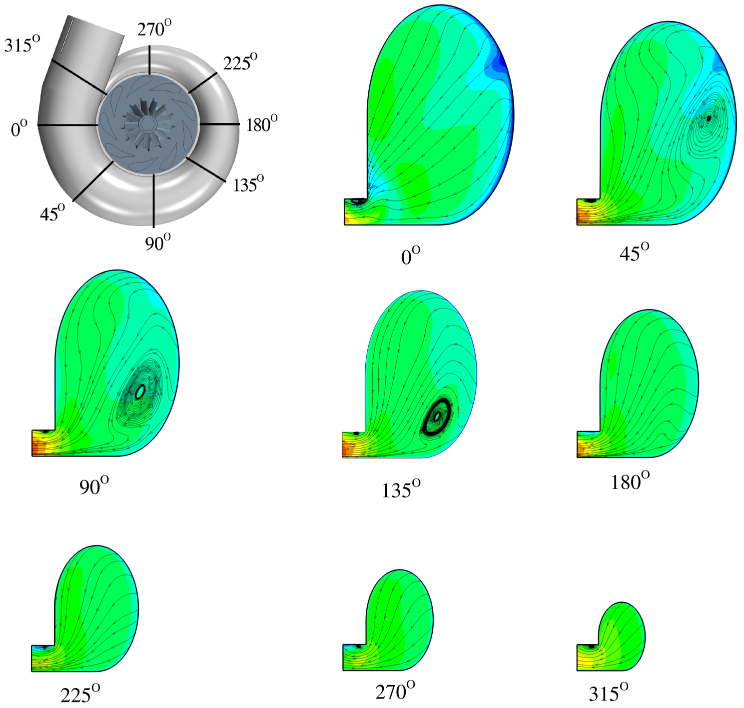

Figure 7.15: Velocity contour and streamline plots for asymmetrical, semi-elliptical scroll cross-sectional shape with AR = 1.5

Streamline plots in Figure 7.14 and 7.15 display weaker vortices at an azimuth angle of 45°, 90°, and 135° from the volute throat. This first group of secondary flows appears at the flow region further away from the volute exit, which has a lower velocity magnitude. The second group of the secondary flows shows up at the corner of the volute crosssections after the flow turns 90°, inducing a corner vortex as displayed on each crosssection. In contrast to reference [114] the secondary flows did not disappear as the volute aspect ratio changes. Secondary flow occurs in a scroll due to nonuniformity in the inlet flow and the interplay between pressure and centrifugal forces within boundary layer regions of the scroll wall [128].

As described above, the asymmetric nature of the volute cross-sectional shape resulted in nonuniform flow at the volute outlet. A symmetrical volute with a trapezoidal cross-sectional shape is developed to emphasize the flow development at the volute exit. The symmetric scroll with trapezoidal cross-section has three geometric parameters: the trapezoid cross-section height (h), the trapezoid side angle (θ), and the trapezoid corner radius values, as shown in Figure 7.16a.

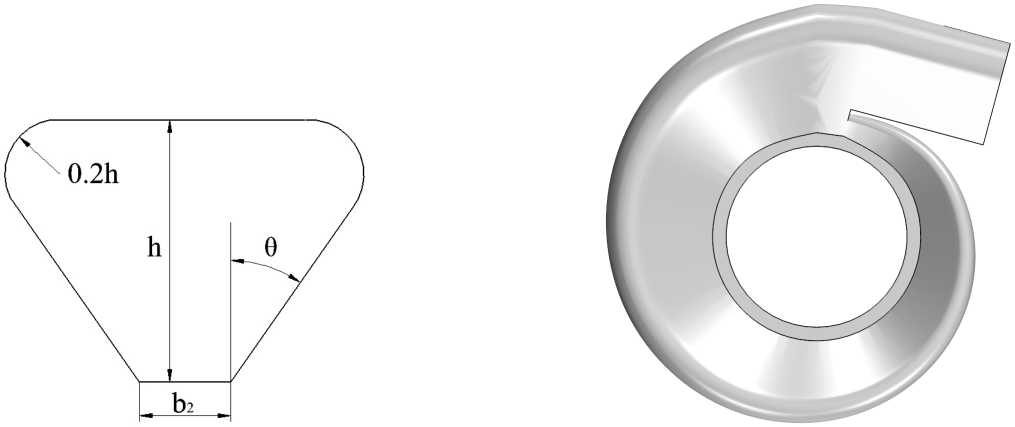

(a) Section details of the trapezoidal volute (b) 3D CAD model of the trapezoidal volute

Figure 7.16: The symmetric volute with trapezoidal cross-sectional shape

The trapezoid height is calculated using mass and angular momentum conservation equations following a similar design approach to the semi-elliptical volute. The corner radius is set at 20 % of the cross-section height, and the trapezoid angle is fixed at 35°. The velocity contour and streamline plots for the symmetrical volute are shown in Figure 7.17.

The symmetric volute velocity profile shows a uniform distribution at the volute outlet, with the flow velocity magnitude increasing with a decrease in radius. The symmetric volute performance is also slightly better than all the asymmetric semi-elliptic scroll shapes discussed above. The symmetric volute isentropic efficiency increased slightly and the pressure loss coefficient dropped significantly compared to the semi-elliptical scroll with a 0.75 aspect ratio.

In Figure 7.17, secondary flows in the symmetric volute appear at volute 45°, 90°, and 135° azimuth angles, similar to the semi-elliptic volutes. The vortices in the symmetrical volute also disappear with an increase in the volute azimuth angle. The noticeable difference between the streamline plots for symmetric volute in Figure 17 with the streamline plots for asymmetric volutes in Figure 7.14 and Figure 7.15 is the disappearance of the corner vortices, assisting the uniform flow distribution at the volute exit. The trapezoidal symmetric volute exhibits additional weaker secondary flows near the volute corners. The influence of these vortices is minimal as they occur in the flow region, where the velocity magnitude is relatively lower. The symmetric velocity distribution at the exit of the volute has a more considerable influence on the performance of the volute than weaker secondary vortices.

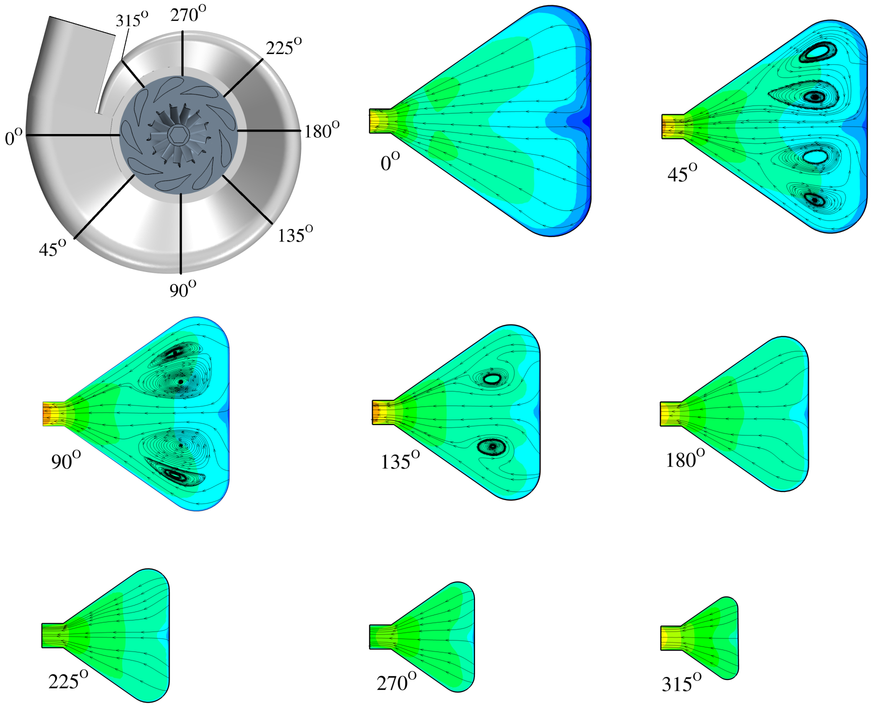

Figure 7.17: Velocity contour and streamline plots for the symmetrical volute

The optimization works discussed so far only consider the near the design point turbine operating point. Two off-design points that have lower and higher mass flow rate values than the design point are analyzed to get a complete picture of the volute design and optimization process. Table 7.2 lists the two off design operating points. The off-design turbine performance is evaluated for two semi-elliptical cross-section volute shapes with AR = 0.75 and AR = 1.5 value and one volute with a trapezoidal cross-section.

Table 7.2: Volute off-design operating points

Variable	**Off-Design point1**	**Off-Design point2**
Mass flow parameter (MFP)	0.01254 ($kg/s \cdot \sqrt{K}/kPa$)	0.03237 ($kg/s \cdot \sqrt{K}/kPa$)
Pressure ratio (PR)	1.421 (-)	2.124 (-)
Reduced rotational speed (N_{red})	1942.09 ($rpm/\sqrt{K}$)	3481.45 ($rpm/\sqrt{K}$)

In Figure 7.18, the isentropic turbine efficiency and pressure loss coefficient values of the three volutes at one on-design and two off-design operating points are displayed. The values are normalized by values at the design point. The symmetrical volute with trapezoidal cross-sectional shape delivered a better isentropic turbine efficiency value at all three operating points. The symmetric volute also reduces pressure loss coefficient values followed by the semi-elliptic volute with an AR = 0.75.

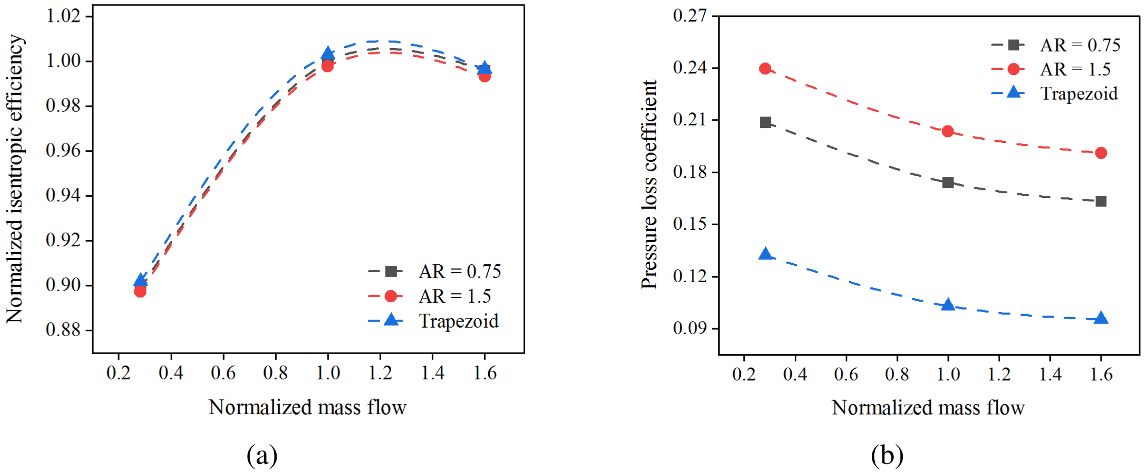

Figure 7.18: Normalized isentropic efficiency (7.18a) and volute pressure loss coefficient (7.18b) values for trapezoidal and semi-elliptic cross-sectional shapes with AR = 0.75 and AR = 1.5

At this point, it has to be mentioned that the symmetric volute with trapezoidal cross-sectional shape, despite the aerodynamics performance-related advantages, its overall size increased noticeably compared to the semi-elliptical volute shapes. The enlarged volute size might pose a problem in the downsizing of the turbocharger and the engine.

7.6 Twin-scroll Volute Geometry Definition

The scroll shape of the twin volute is designed from a combination of a triangle and an ellipse as shown in Figure 7.19. The aspect ratio of the ellipse is considered as one of the volute geometry design parameters. The scrolls' other geometry parameters include the scroll angle, the volute throat to exit radius ratio, the divider tip radius, the divider tip center from the throat radius, and the divider wall angle. Figure B.2 shows the throat geometry details used for the full scroll geometry generation.

With all scroll geometry variables known, the next step is to estimate the volute throat area

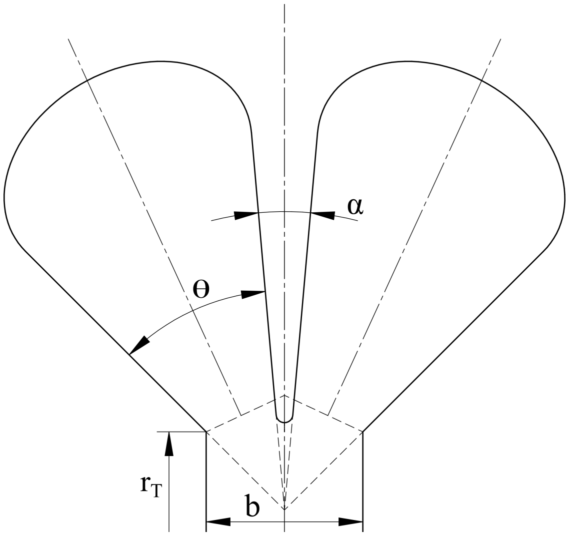

Figure 7.19: Twin-scroll volute shape

and centriod radius values. The procedure to define the scroll geometry is shown in Figure 7.20. At start of volute geometry generation, the throat area and centroid radius values are unknown. Both values are estimated iteratively employing the free vortex constant defined in Eq.(7.1), and conservation of mass equation defined in Eq.(7.5). Figure 7.3 shows the iterative procedure used to estimate the throat area and centroid radius values.

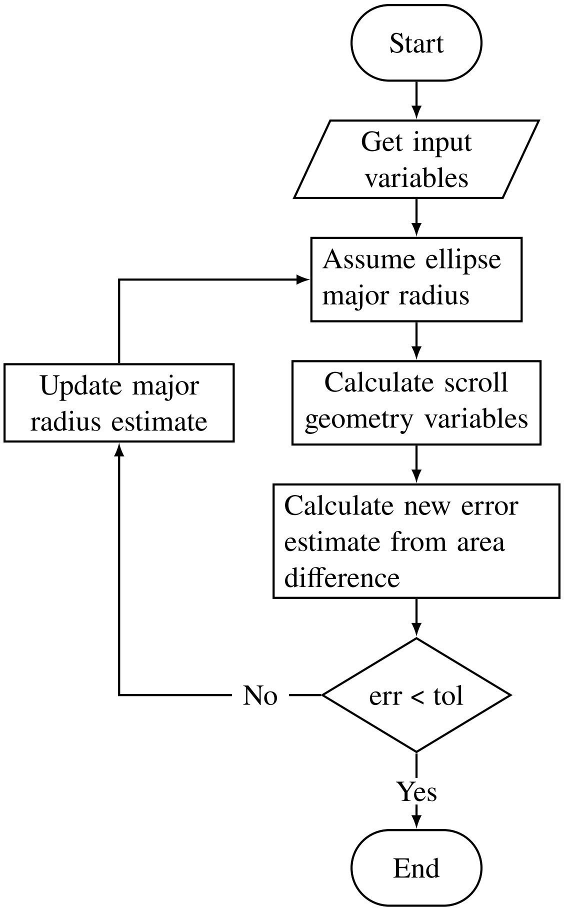

Figure 7.20: Procedure to estimate the scroll geometry variables

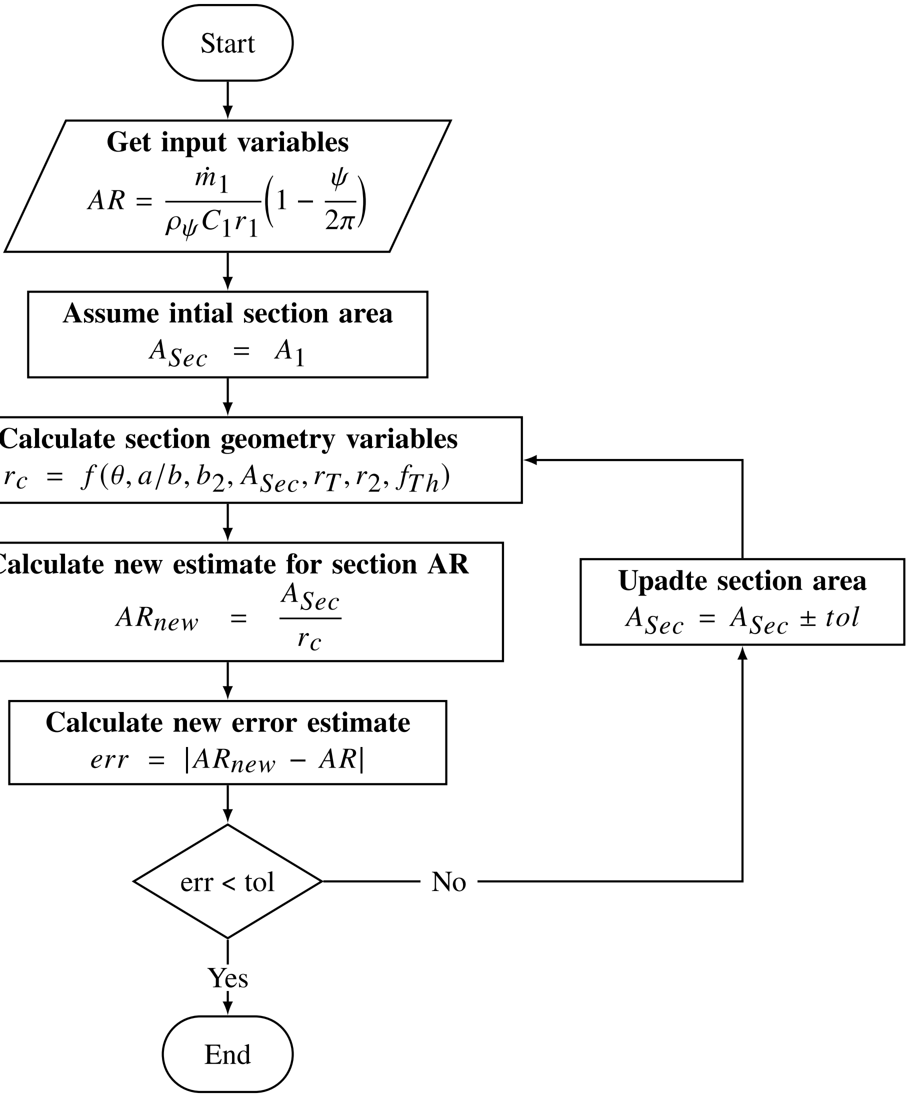

Figure 7.21: Procedure to estimate the volute throat geometry and flow variables

7.7 Volute Geometry Optimization

7.7.1 Effect of Volute Angle

The effect of volute angle on the performance of the volute, and eventually on the turbine efficiency, is studied by considering three volute angles. The overall turbine efficiency and volute pressure loss values are evaluated at each volute angle for three engine load cases with turbine mass flow rates ranging from low-high. Figure 7.22 shows the change in volute pressure loss of the twin-scroll volute when the volute angle varies from 30° to 40°.

Since the twin-scroll volute has two entries, the pressure loss coefficient defined by Eq.(7.18) is modified in Eq.(7.19) considering the mass flow from each inlet. In the modified equation, the mass flow average of the two inlet pressure values replaces the single total inlet pressure value in Eq.(7.18).

$$C_{PL} = \frac{\dot{m}_{inlet1} \times P_{0inlet1} + \dot{m}_{inlet2} \times P_{0inlet2} - (\dot{m}_{inlet1} + \dot{m}_{inlet2}) \times P_{02}}{(\dot{m}_{inlet1} + \dot{m}_{inlet2}) \times (P_{02} - P_2)} \tag{7.19}$$

The coefficient quantifies the decrease in the total pressure of the flow between the volute inlet and the outlet due to wall friction effects. In an ideal volute, the drop in the total pressure is assumed to be negligible ($P_{01} = P_{02}$). The loss coefficient commonly ranges between 0.1 and 0.3 [129]. For all three turbine mass flow rates considered, the volute pressure loss increased with the volute angle. On the contrary, the overall turbine efficiency isn't significantly affected by the volute angle change.

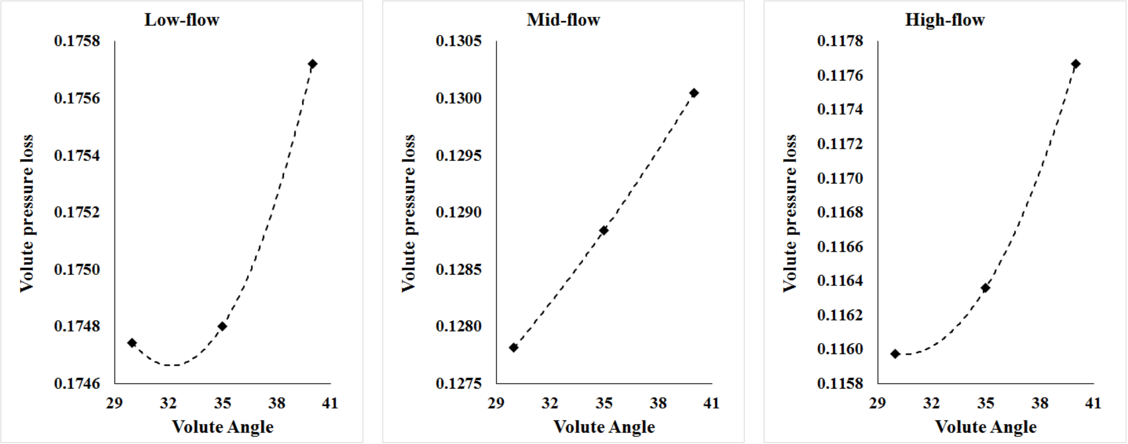

(a) Low-flow (b) Mid-flow (c) High-flow

Figure 7.22: Volute pressure loss for three turbine mass flows from low to high

All the CFD results in Figure 7.22 are computed at a throat to nozzle inlet radius ratio of 1.05 and dividing wall tip radius to throat radius ratio of 1.05. All radii values are measured for the turbine rotational axis.

7.7.2 Effect of Volute Tongue Angle

The volute tongue is responsible for generating non-uniform flow around the circumferential outlet of the volute, altering the flow angle of the flow admitted to nozzle blades. Various researchers studied the effect of tongue geometry on a vaneless radial turbine performance [113, 127]. Suhrmann et al. [113] followed a numerical CFD approach to analyze the effect of the volute tongue, suggesting a smaller togue radius with small tongue analyses delivers a maximum efficiency while a larger tongue increases the turbine's robustness. Hussain et al. [127] used an experimental investigation to find the optimum tongue angle for vaneless to be approximately 23°. This optimized tongue angle is suggested by considering the radial vortex development and while keeping a higher tangential velocity in the radial direction.

Five volute tongue angles in the range of 10°to 30°are used to optimize the twin-scroll geometry at the design point.

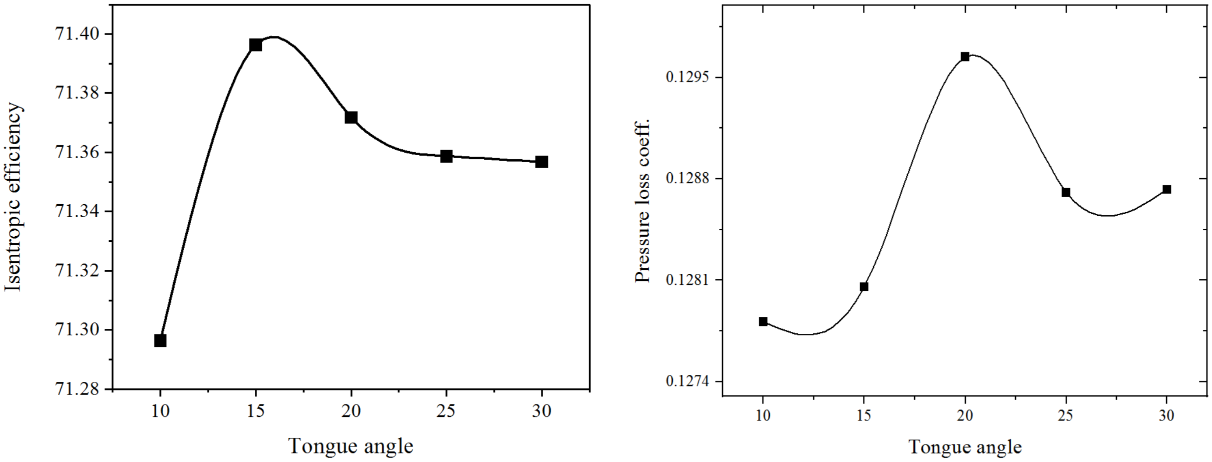

(a) Volute tongue angle vs Isentropic efficiency (b) Volute tongue angle vs Pressure loss coeff.

Figure 7.23: Effect of volute tongue angle on the turbine isentropic efficiency and volute pressure loss coefficient near design point

The effect of the tongue angle on the overall turbine efficiency is minimal, with only a 0.1% difference noticed between maximum and minimum values. The highest volute pressure loss coefficient varied by 0.002 from the lowest value in the entire volute tongue angle range as shown in Figure 7.23. The presence of the nozzle blades reduced the effect of the tongue. In addition, the flow nonuniformness due to the tongue geometry is more noticeable at uneven flows and operating points further away from the design point.

7.7.3 Effect of Dividing Wall Tip Height

The tip factor defines the dividing wall tip position relative to the tongue radius ($f_{tip} = r_{tip}/r_T$) as shown in Figure 7.24. When the tip is further away from the tongue (a larger f_{tip} value), a cross-flow from one scroll to the another occurs, altering the volute pressure and mass distribution of the downstream volute flow. In contrast, the volute loss increases at smaller f_{tip} values (the dividing wall tip is close to the tongue). Thus the dividing wall tip height should be optimized considering the turbine efficiency and volute pressure loss factors.

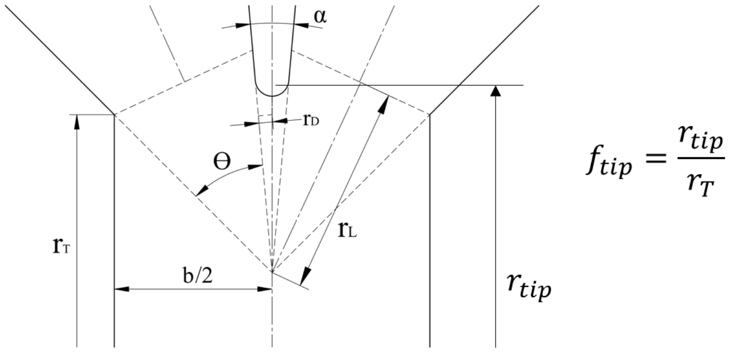

Figure 7.24: Dividing wall tip height factor

The effect of the dividing wall valley height is studied for three flow cases, as shown in Figure 7.25 and Figure 7.26. The first case (case 1) represents a low mass flow rate turbine operating point, while the second case (case 2) is for a mid-mass flow rate operation near the turbine design point. The last case (case 3) is for high mass flow turbine operation. As shown in Figure 7.25, the effect of the dividing wall height on the overall turbine efficiency is not conclusive as no trendline was established for the three cases. On the other hand, the volute pressure loss coefficient decreased with f_{tip}, as shown in Figure 7.26.

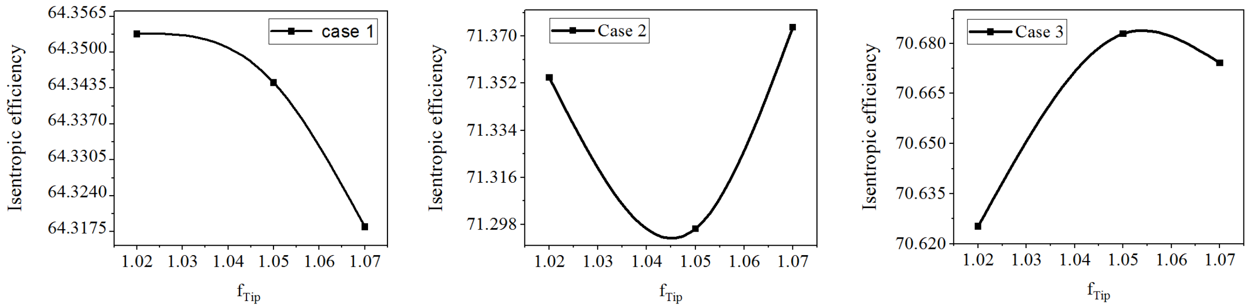

Figure 7.25: Dividing wall tip height factor

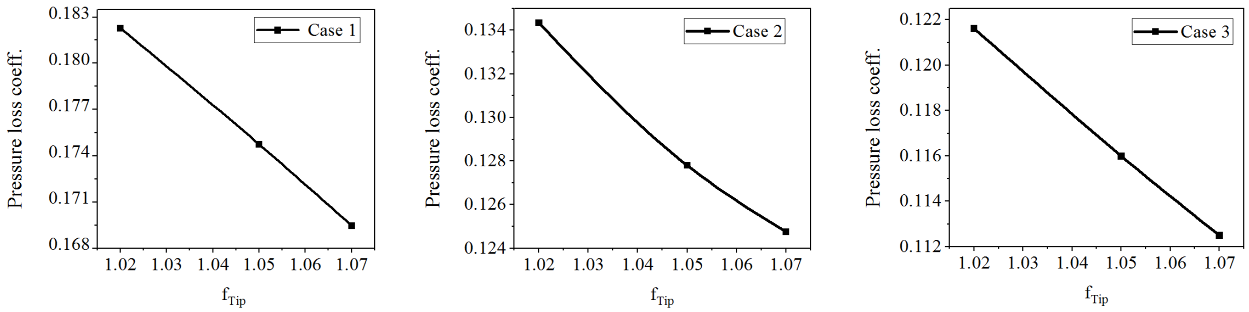

Figure 7.26: Dividing wall tip height factor

7.8 The Symmetric Twin-scroll Turbine Uneven Flow Performance Analysis

The effect of uneven flow across the twin scroll inlets is analyzed by admitting more flow to the hub or shroud side scroll at near design point (case2, in Figures 7.25 and 7.26) turbine operation. Three uneven flows at 70%, 90%, and 100% of the total flow are admitted to each scroll inlet, while the other scroll has the remaining portion of the flow.

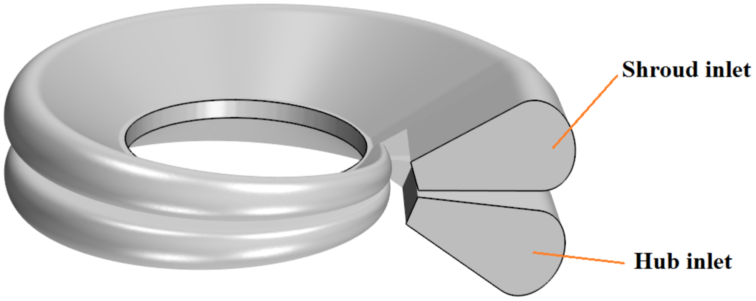

Figure 7.27: Hub and shroud inlets

Admitting more flow to the shroud side resulted in a higher efficiency value than the hub scroll biased flow and the dual-entry turbine, as shown in Figure 7.28. The pressure loss increased with

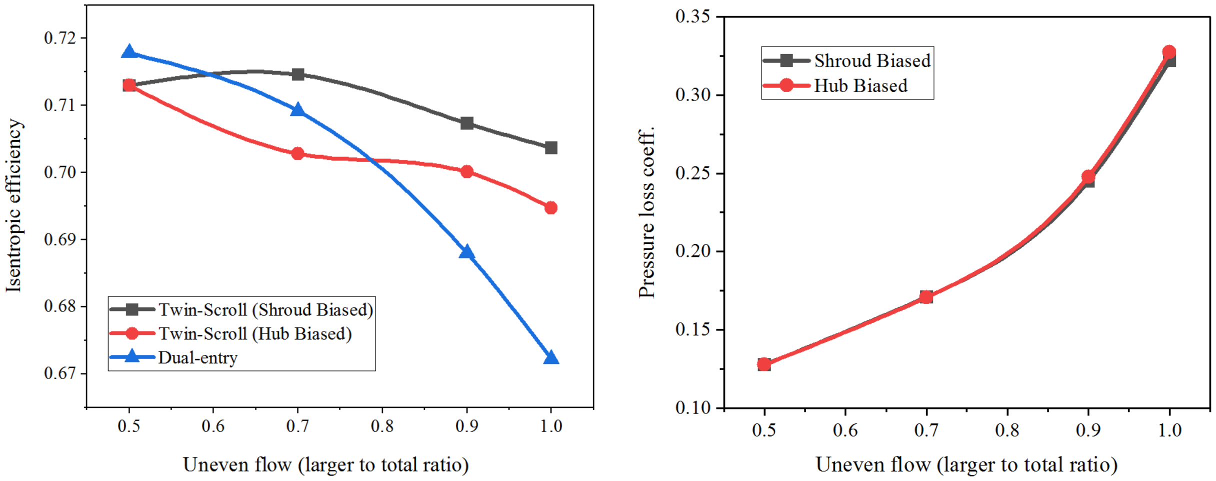

(a) Uneven flow vs Isentropic efficiency

(b) Uneven flow vs Pressure loss coeff.

Figure 7.28: Symmetrical twin-scroll uneven flow admission effect on isentropic efficiency and pressure loss at near design point turbine operation

the uneven flow for both admission cases with similar effects. Since the dual-entry volute has two tongues, an increased uneven flow across the volute inlets resulted in enlarged losses than the symmetric twin-scroll in the volute and nozzle regions.

7.9 Asymmetric Twin-scroll Turbine Under Steady Flow Conditions

The asymmetric twin-scroll geometry is set by considering the asymmetric factor. The asymmetric factor is defined as the ratio of the larger to small throat scroll area. The flow inside the larger scroll (also known as the Lambda scroll) is expected to have a higher mass flow rate and pressure values, while the flow inside the small scroll (also known as the EGR scroll) will have a lower mass flow rate and pressure values. The optimum asymmetric factor is determined by considering how the isentropic turbine efficiency and volute pressure loss coefficient varies with the factor. Five asymmetric factors are used for each Lambda scroll position (either the hub or the shroud side). The hub and shroud lambda scrolls are shown in Figure 7.29.

The isentropic efficiency increased for the hub lambda scroll than the shroud. The isentropic efficiency value is maximized at the asymmetric factor of 1.41 for the hub lambda scroll, as shown in Figure 7.30. The shroud lambda scroll resulted in a consistent increase in the pressure loss

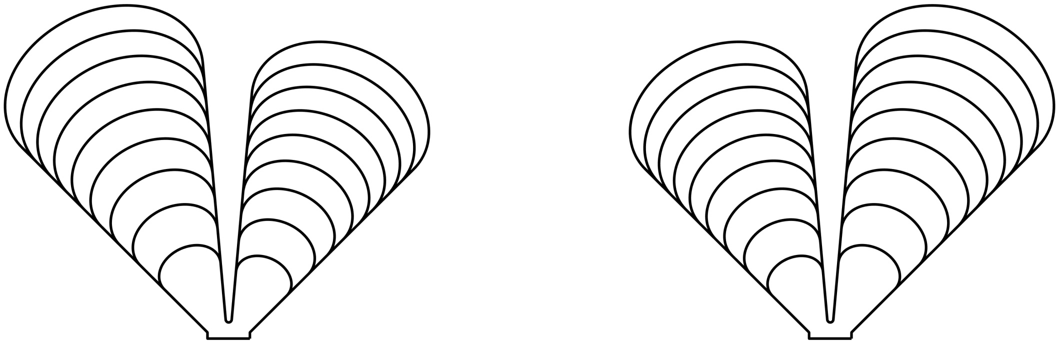

(a) Hub lambda scroll (b) Shroud lambda scroll

Figure 7.29: Asymmetric twin-scroll hub and shroud lambda scrolls

coefficient with an increase in the asymmetric factor. In contrast, the pressure loss coefficient for the hub lambda scroll has the smallest value at an asymmetric factor of approximately 1.2, as shown in Figure 7.30.

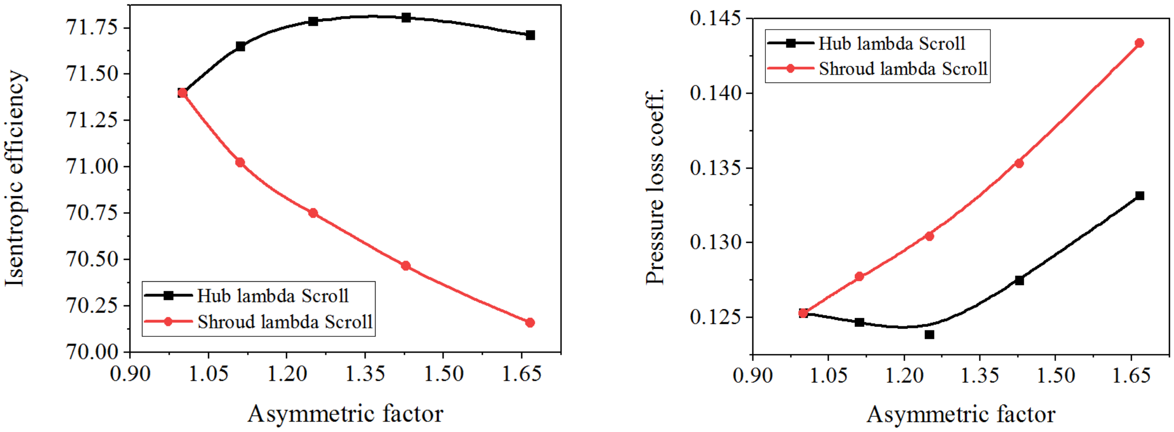

(a) Asymmetric factor vs Isentropic efficiency (b) Asymmetric factor vs Pressure loss coeff.

Figure 7.30: Asymmetric factor effect on the isentropic efficiency and pressure loss coeff.

7.10 Asymmetric Twin-scroll Turbine Uneven Flow Performance Analysis

The asymmetric twin-scroll turbine uneven flow performance is analyzed at a volute angle of 30 °and an asymmetric factor of 1.41. One even case with equal mass flow rate across the two twin-scrolls inlets and three uneven flows with more mass flow rate to the lambda scroll (for both hub and shroud sides) are considered.

The hub lambda twin-scroll turbine outperformed the shroud lambda twin-scroll and the dual-entry turbine in all three uneven flow cases. The dual-entry uneven flow deteriorated even more at increased uneven flows due to its additional tongue. In partial admission cases ($m_{Lambda}/m_{Total} = 1$), the efficiency of the hub lambda scroll is more than the dual-entry by about 3%. As discussed in section 6.4.3, the volute is the main source of losses in partial admissions flow cases in the dual-entry turbine. The pressure loss coefficient of the dual-entry volute increased sharply with an increase in uneven flow as shown in Figure 7.31b.

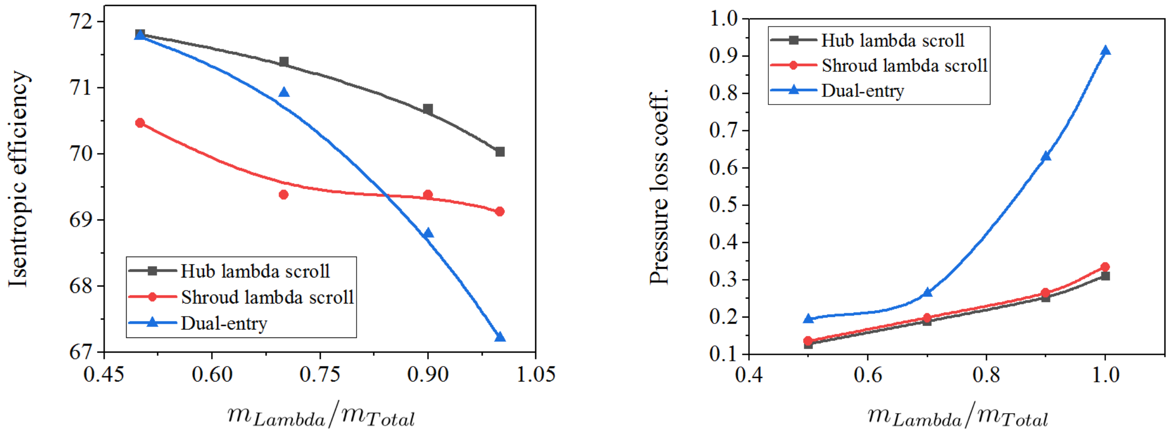

(a) Isentropic efficiency vs scroll mass flow ratio (b) Pressure loss coeff. vs scroll mass flow ratio

Figure 7.31: Uneven flow analysis for asymmetric twin-scroll turbine

CHAPTER 8

CONCLUSIONS

In chapter 4, a turbocharger compressor performance is predicted using a new set of one-dimensional loss models and numerical CFD simulations. Eckart B's compressor experimental data validated the proposed loss model combination, resulting in a satisfactory agreement.

The compressor performance predicted from the 1-D compressor loss model combinations is checked with the numerical results, producing satisfactory agreement at most compressor operating points. However, the compressor loss models have inconsistency in analyzing the compressor performance depending on the compressor size, and rotational speed is observed. The models seem to work well for larger compressors with relatively low rotational speeds, compared to turbocharger compressors with smaller sizes and higher rotational speeds. The observed insufficiency in the loss models suggests a need for an improved loss model that can capture the different compressor losses accurately.

The 1-D compressor models also fail to consider the casing treatment effects on the compressor's mass flow, pressure ratio, and isentropic efficiency values. Geometric characteristics of the casing treatment affect compressor performance metrics uniquely, depending on its shape, angle, and interaction location with the compressor shroud. A better compressor model should include surge and choke channel flows, along with their associated pressure and efficiency losses.

The unique design features of the active casing treatment provide extensive advantages in extending the surge to the choke margin. In the original design of the choke slot closed compressor configuration, an extended surge margin was achieved at the cost of isentropic efficiency. The drop in isentropic efficiency value increased with an increase in the compressor speed. Choke slot thickness optimization results show that decreasing choke slot thickness improves the isentropic efficiency of the compressor for operating points close to the surge limit. On the other hand, the choke margin decreased slightly when the compressor ran close to the choke limit with the decrease in choke slot thickness.

Optimizing the choke slot and surge slot geometries with modern optimization tools would provide a more comprehensive picture of the flow in the casing treatment. Moreover, the surge limit of each design combination is better understood and predicted using a transient simulation. The rotating stall that precedes the deep surge can be captured accurately by a transient simulation.

In chapter 5, the acoustics performance of the turbocharger compressor for different casing treatment configurations is predicted using steady and transient state simulations. The steady-state results marked the sound sources in the compressor components using the Curle and Proudman acoustics analogies. Steady-state aeroacoustics simulation results can be used to compare different design options on the noise level they produce. Since the sound generating pressure fluctuations have very small amplitudes, a robust CFD setup that uses DES turbulence modeling is employed at two compressor operating points. Point probes and circumferential line average probes are used to predict the blade passing frequency and broadband noise levels at the inlet and exit compressor pipes. The first compressor operating point selected is close to the surge limit at a higher rotational speed with the choke closed compressor configuration. In contrast, the second considers the choke slot open configuration near the maximum efficiency point of the compressor.

The pressure spectra analysis of the inlet and exit pipes predicted the blade passing frequency accurately and its harmonics for both types of probes accurately for both configurations. Both broadband and blade passing frequency noise levels increased with the increase of the compressor speed. The exit duct noise levels are found to be higher than the inlet pipe by about 20 dB. Both broadband and blade passing frequency noises decreased as the probe points moved away from the compressor wheel.

Aeroacoustics simulations demand expensive computer and time resources. With the current computer resource available at a university level, any optimization work that depends on a detailed transient aeroacoustic simulation should be followed at the last stage of the optimization work.

In Chapter 6, a VTG turbine's performance with dual volute is assessed numerically at various flow ratios between the two volute inlets: one even and three uneven volute inlet flows. The analysis is completed for three test conditions: low flow well below peak efficiency, medium flow near peak efficiency, and high flow well above peak efficiency. Experimental data at nine test data points verified the numerical CFD setup at full load admission with the turbine running at 70% of the rated turbine speed. The CFD results presented a reasonable agreement with the experimental data, producing a 4.2% discrepancy for efficiency estimation and a 0.36 % discrepancy for the pressure ratio estimation.

The effect of uneven turbine inlet admission is studied by computing the local entropy production rate per volume using Kock and Herwig model. The local entropy sources are identified by decomposing the CFD domain into a total of eleven sub-regions. A fine mesh with approximately 50 million elements and an average entropy ratio of 0.72 is used to estimate the local entropy production rate per volume for each test case. The entropy analysis is found to be highly dependent on mesh quality and, more importantly, on the near-wall mesh growth rate and first boundary layer thickness values.

In all the three flow conditions considered for the study, the impeller regions contribute the most to the overall turbine losses. The local entropy production rate near the tip regions is the primary source of the impeller losses in all flow cases considered for the study. Even though uneven flow through the turbine inlets increased the entropy production rate for all three engine loads, it considerably affected the volute region performance. The effect of uneven flow on the volute performance is perceived more at higher mass flow rates. The volute loss percentage to overall turbine performance for high flow conditions grew from approximately 4% to 26% as the flow distribution changed from 50%-50% to 0%-100%.

Overall, the mass imbalance across the two inlets significantly deteriorates the turbine performance with high EGR rate conditions. The study's steady-state analysis would help identify the loss sources in turbocharger assembly at even and uneven turbine inlet mass flows for further part design modifications.

Chapter 7 discusses the effect of different geometric parameters on the aerodynamic performance of a single-scroll and twin-scroll turbocharger turbine. Three important geometry parameters, namely the tongue angle, tongue clearance, and scroll shape, are considered for the study. Two performance parameters, the isentropic efficiency and the pressure loss coefficient values, quantified the influence of each geometric parameter examined.

The numerical result of the single-scroll turbine shows that a lower volute tongue angle lowers the pressure loss in the volute. On the other hand, an increased tongue clearance decreases the pressure loss inside the volute and thus enhances the turbine's isentropic performance.

The velocity profile at the volute exit was analyzed to understand the effect of the volute shape on overall turbine performance. The asymmetric scroll with a semi-elliptical cross-sectional shape resulted in a nonuniform flow due to separation after the flow turned 90°. The volute performance is significantly improved with a trapezoidal cross-section design, as the flow exiting the volute is evenly distributed between the hub and shroud gap.

The optimization study results show that smaller volute angles provide minimized volute pressure loss coefficients for the twin-scroll geometry design. In contrast, an increased tip height factor decreases the value of the volute pressure loss coefficients. The dual entry turbine performance is also compared against symmetric twin-scroll turbine for three mass flow rates. Both scrolls performed equivalently at even flow (equal admission), while at uneven flow cases, the twin-scroll, with a higher mass flow rate on the shroud side, outperformed the dual-entry scroll. The presence of the second volute tongue diminishes the dual-entry performance, as explained in chapter 7.

The asymmetric twin-scroll provides improved performance for higher EGR flows with the bigger scroll (the lambda scroll) positioned on the hub side. The optimum asymmetric factor is estimated by comparing the isentropic efficiency and pressure loss coefficient values at the near design point operation of the compressor. Comparing the pressure loss coefficient of the hub lambda scroll vs. the shroud lambda scroll reveals that the shroud lambda scroll has higher losses.

APPENDICES

APPENDIX A

COMPRESSOR NOISE ESTIMATED BY VOLUME AND SURFACE INTEGRALS OF THE ACOUSTIC POWERS

Table A.1: Volume integral of the Proudman's acoustic power for choke slot closed configuration near maximum efficiency point at 120k rpm compressor speed

Compressor parts	Proudman's acoustic power (W)	Parts's contribution (%)
Choke channel	1.99E-04	2.64%
Exit pipe	8.00E-08	0.00%
Impeller	5.79E-03	76.90%
Inlet	1.13E-06	0.02%
Inlet pipe	1.60E-09	0.00%
Surge channel	2.16E-06	0.03%
Volute	1.54E-03	20.41%
Total	7.53E-03	100.00%

Table A.2: Volume integral of the Proudman's acoustic power for choke slot closed configuration near surge point at 120k rpm compressor speed

Compressor parts	Proudman's acoustic power (W)	Part's contribution (%)
Choke channel	2.88E-04	11.85%
Exit pipe	7.67E-07	0.03%
Impeller	1.58E-03	65.08%
Inlet	4.59E-07	0.02%
Inlet pipe	2.39E-10	0.00%
Surge channel	6.31E-05	2.60%
Volute	4.96E-04	20.42%
Total	2.43E-03	100.00%

Table A.3: Volume integral of the Proudman's acoustic power for choke slot open configuration near maximum efficiency point at 120k rpm compressor speed

Compressor parts	Proudman's acoustic power (W)	Part's contribution (%)
Exit pipe	1.07E-07	0.00%
Impeller	2.04E-02	90.32%
Inlet	1.90E-04	0.84%
Inlet pipe	1.54E-09	0.00%
Volute	2.00E-03	8.84%
Total	2.26E-02	100.00%

Table A.4: Volume integral of the Proudman's acoustic power for choke slot open configuration near surge point at 120k rpm compressor speed

Compressor parts	Proudman's acoustic power (W)	Part's contribution (%)
Exit pipe	3.81E-07	0.00%
Impeller	1.97E-02	73.65%
Inlet	6.07E-03	22.71%
Inlet pipe	9.55E-08	0.00%
Volute	9.74E-04	3.64%
Total	2.68E-02	100.00%

Table A.5: Surface integral of the Curle's acoustic power for choke slot closed configuration near maximum efficiency point at 120k rpm compressor speed

Compressor wall surfaces	Curle's acoustic power (W)	Surface's contribution (%)
Choke	1.53E-02	0.86%
Exit pipe	1.07E-03	0.06%
Impeller shroud	3.11E-01	17.39%
Impeller blades	2.94E-01	16.44%
Impeller hub	3.42E-01	19.12%
Inlet	1.40E-03	0.08%
Inlet pipe	1.88E-05	0.00%
Surge channel	1.54E-04	0.01%
Diffuser	6.99E-01	39.08%
Volute	1.25E-01	6.97%
Total	1.79	100.00%

Table A.6: Surface integral of the Curle's acoustic power for choke slot closed configuration near surge point at 120k rpm compressor speed

Compressor wall surfaces	Curle's acoustic power (W)	Surface's contribution (%)
Choke	4.49E-02	3.64%
Exit pipe	5.23E-04	0.04%
Impeller shroud	1.64E-01	13.31%
Impeller blades	1.44E-01	11.67%
Impeller hub	2.02E-01	16.40%
Inlet	6.21E-04	0.05%
Inlet pipe	5.37E-06	0.00%
Surge channel	1.34E-02	1.09%
Diffuser	5.74E-01	46.57%
Volute	8.91E-02	7.23%
Total	1.23	100.00%

Table A.7: Surface integral of the Curle's acoustic power for choke slot open configuration near near maximum efficiency point at 120k rpm compressor speed

Compressor wall surfaces	Curle's acoustic power (W)	Surface's contribution (%)
Exit pipe	1.38E-03	0.08%
Impeller shroud	2.12E-01	11.97%
Impeller blades	3.05E-01	17.23%
Impeller hub	3.28E-01	18.50%
Inlet	1.35E-02	0.76%
Inlet pipe	1.71E-05	0.00%
Diffuser	7.29E-01	41.13%
Volute	1.83E-01	10.33%
Total	1.77	100.00%

Table A.8: Surface integral of the Curle's acoustic power for choke slot open configuration near near surge point at 120k rpm compressor speed

Compressor wall surfaces	Curle's acoustic power (W)	Surface's contribution (%)
Exit pipe	3.17E-04	0.02%
Impeller shroud	3.24E-01	21.18%
Impeller blades	2.13E-01	13.89%
Impeller hub	2.13E-01	13.91%
Inlet	7.64E-02	4.99%
Inlet pipe	5.78E-06	0.00%
Diffuser	6.05E-01	39.51%
Volute	9.96E-02	6.50%
Total	1.53	100.00%

APPENDIX B

TWIN-SCROLL GEOMETRY DEFINITION DETAILS

The twin-scroll geometry is defined by a combination of basic shapes that include ellipses, triangles, and circular curves as shown in Figure (B.1) and Figure (B.2). The detailed shape definition of the volute depends on different design parameters such as the throat radius (r_T), the volute angle (θ), the volute outlet width (b), and the dividing tip radius at the throat radius (r_D).

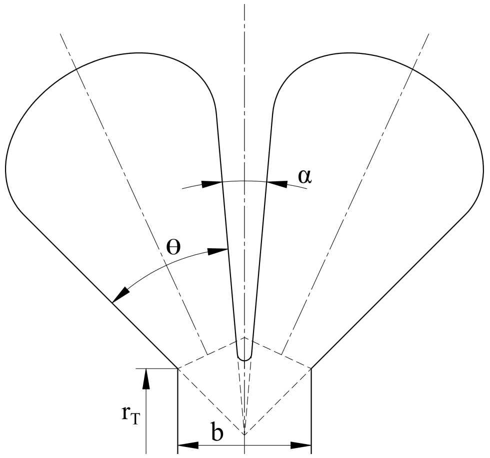

Figure B.1: Twin-scroll volute shape

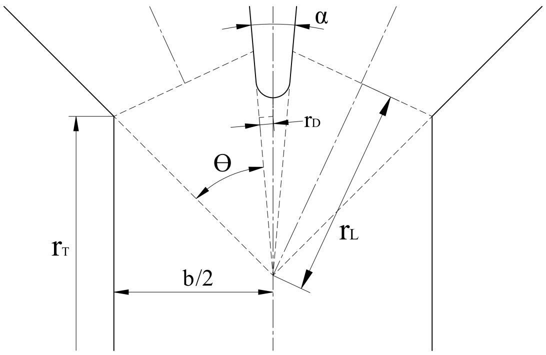

Figure B.2: Volute throat geometry detail

With r_D, b, and θ values known, the dividing wall angle α value is estimated iteratively using Eq.(B.1).

$$\tan\left(\theta + \frac{\alpha}{2}\right) = \frac{b \cdot \sin\left(\frac{\alpha}{2}\right)}{2 \cdot r_D} \tag{B.1}$$

Each scroll area is calculated by dividing the area into an elliptical and a five-sided polygon area, as shown in Figure B.3. Eq.(B.2) calculates the elliptic curve endpoints.

$$(u, v) = \left(\frac{-a^2 m}{\sqrt{a^2 m^2 + b^2}}, \frac{b^2}{\sqrt{a^2 m^2 + b^2}}\right) \tag{B.2}$$

The scroll bounding lines are tangent to each end of the ellipse curve. The slope of the lines is computed from scroll angle, θ, by Eq. (B.3).

$$m = \tan\left(\frac{\pi}{2} - \frac{\theta}{2}\right) \tag{B.3}$$

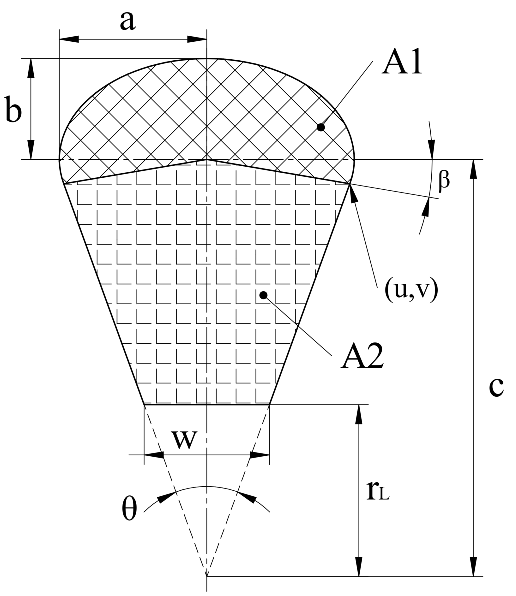

Figure B.3: Scroll geometry detail

The elliptical curve end points are located at angle β from the horizontal x-axis as defined in Figure B.3. Angle β can be calculated from (u, v) points using Eq. (B.4).

$$\beta = \tan^{-1}\left(\frac{v}{u}\right) \tag{B.4}$$

The method described by Eberly [130] estimates the ellipse part of the volute cross-sectional area. The ellipse radius at angle ϕ is given in Eq.(B.5). The ellipse major and minor radii values are a and b in the x and y axes, respectively.

$$r^2 = \frac{a^2b^2}{b^2\cos^2\phi + a^2\sin^2\phi} \tag{B.5}$$

The ellipse sector area between two angle ϕ_1 and ϕ_0 in Fig. B.4 is calculated by Eq.(B.6).

$$A(\phi_0, \phi_1) = \int_{\phi_0}^{\phi_1} \frac{1}{2} r^2 d\phi = \int_{\phi_0}^{\phi_1} \frac{a^2b^2/2}{b^2\cos^2\phi + a^2\sin^2\phi} d\phi \tag{B.6}$$

An anti derivative of the integrand in Eq.(B.6) is given by Eq.(B.7)

$$F(\phi) = \frac{ab}{2}\left[\phi - \tan^{-1}\left(\frac{(b-a)\sin 2\phi}{(b+a) + (b-a)\cos 2\phi}\right)\right] \tag{B.7}$$

The inverse tangent $\tan^{-1}(\phi)$ in Eq. (B.7) ranges between $(-\pi/2, \pi/2)$. The ellipse sector area is given by Eq.(B.8)

$$A(\phi_0,\ \phi_1) = F(\phi_1) - F(\phi_0) \tag{B.8}$$

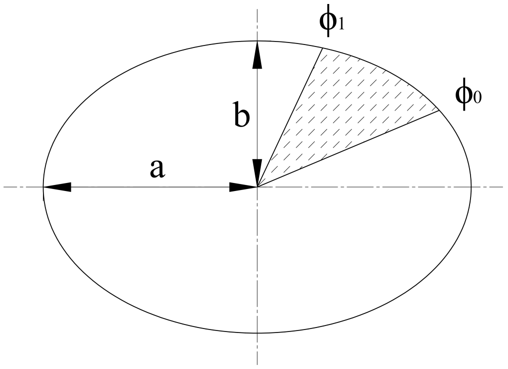

Figure B.4: Ellipse sector area

The remaining two dimensions needed to fully define the scroll geometry are the hr_L height and W width values as defined in Figure B.3. Their values can be calculated by Eq.(B.9) and Eq.(B.10)

$$r_L = \frac{r_D \cdot \cos\left(\theta/2\right)}{\sin\left(\alpha/2\right) \cdot \cos\left(\theta + \alpha/2\right)} \tag{B.9}$$

$$W = \frac{2r_L}{\cos\left(\theta/2\right)} \tag{B.10}$$

The five-sided polygon area is calculated by a method developed by Bourake [131]. For a closed polygon with N vertices, the area is given by Eq.(B.11).

$$A = \frac{1}{2}\sum_{i=0}^{N-1}\left(x_i \times y_{i+1} - x_{i+1} \times y_i\right) \tag{B.11}$$

The polygon centroid x and y values are also calculated from the vertices, as given by Eq.(B.12).

$$\begin{aligned} C_x &= \frac{1}{6A}\sum_{i=0}^{N-1}\left(x_i + x_{i+1}\right)\left(x_i \times y_{i+1} - x_{i+1} \times y_i\right) \\ C_y &= \frac{1}{6A}\sum_{i=0}^{N-1}\left(y_i + y_{i+1}\right)\left(x_i \times y_{i+1} - x_{i+1} \times y_i\right) \end{aligned} \tag{B.12}$$

BIBLIOGRAPHY

BIBLIOGRAPHY

[1] P. Leduc, B. Dubar, A. Ranini, and G. Monnier, "Downsizing of gasoline engine: an efficient way to reduce co2 emissions," *Oil & gas science and technology*, vol. 58, no. 1, pp. 115–127, 2003.

[2] A. Maiboom, X. Tauzia, and J.-F. Hétet, "Experimental study of various effects of exhaust gas recirculation (egr) on combustion and emissions of an automotive direct injection diesel engine," *Energy*, vol. 33, no. 1, pp. 22–34, 2008.

[3] H. Nguyen-Schäfer, *Rotordynamics of automotive turbochargers*. Springer, 2015.

[4] C. D. Rakopoulos and E. G. Giakoumis, *Diesel engine transient operation: principles of operation and simulation analysis*. Springer Science & Business Media, 2009.

[5] A. Engeda, "Advances in understanding the flow in a centrifugal compressor impeller and improved design," *Thermal Engineering in Power Systems*, vol. 22, p. 349, 2008.

[6] D. Japikse, N. Baines *et al.*, *Introduction to turbomachinery*, 1994, no. BOOK.

[7] H. Ronald, "Centrifugal compressors: A strategy for aerodynamic design and analysis," *American Society of Mechanical Engineers Press*, 2000.

[8] H. W. Oh, E. S. Yoon, and M. Chung, "An optimum set of loss models for performance prediction of centrifugal compressors," *Proceedings of the Institution of Mechanical Engineers, Part A: Journal of Power and Energy*, vol. 211, no. 4, pp. 331–338, 1997.

[9] M. Schobeiri, *Turbomachinery flow physics and dynamic performance*. Springer, 2005.

[10] F. Fisher, "Application of map width enhancement devices to turbocharger compressor stages," *SAE transactions*, pp. 1303–1310, 1988.

[11] N. A. Cumpsty, *Compressor aerodynamics*. Longman Scientific & Technical, 1989.

[12] N. Watson and M. Janota, *Turbocharging the internal combustion engine*. Macmillan International Higher Education, 1982.

[13] H. Mohtar, P. Chesse, A. Yammine, and J. Hetet, "Variable inlet guide vanes in a turbocharger centrifugal compressor: local and global study," SAE Technical Paper, Tech. Rep., 2008.

[14] H. Uchida, A. Kashimoto, and Y. Iwakiri, "Development of wide flow range compressor with variable inlet guide vane," *R&D Review of Toyota Crdl*, vol. 41, no. 3, pp. 9–14, 2006.

[15] N. Fraser, T. Fleischer, J. Thornton, and J. Rueckauf, "Development of a fully variable compressor map enhancer for automotive application," SAE Technical Paper, Tech. Rep., 2007.

[16] H. Harada, “Study of a surge-free centrifugal compressor with automatically variable inlet and diffuser vanes,” in *ASME 1996 International Gas Turbine and Aeroengine Congress and Exhibition*. American Society of Mechanical Engineers, 1996, pp. V001T01A050–V001T01A050.

[17] P. Jiang and A. Whitfield, “Investigation of vaned diffusers as a variable geometry device for application to turbocharger compressors,” *Proceedings of the Institution of Mechanical Engineers, Part D: Journal of Automobile Engineering*, vol. 206, no. 3, pp. 209–220, 1992.

[18] P. Eynon, A. Whitfield, M. Firth, A. Parkes, and R. Saxton, “A study of the flow characteristics in the inducer bleed slot of a centrifugal compressor,” in *ASME 1996 International Gas Turbine and Aeroengine Congress and Exhibition*. American Society of Mechanical Engineers, 1996, pp. V001T01A080–V001T01A080.

[19] H. Sun, L. Hu, J. Zhang, D. Hanna, E. Krivitzky, L. Larosiliere, M. Lai, and C. Yang, “Switchable dual-port casing treatment scheme for an enhanced turbocharger compressor operating range,” *Proceedings of the Institution of Mechanical Engineers, Part D: Journal of Automobile Engineering*, vol. 228, no. 3, pp. 235–244, 2014.

[20] H. Sun, D. Hanna, P. Niessen, B. Fulton, L. Hu, E. Curtis, and J. Yi, “Experimental evaluation of advanced turbocharger performance on a light duty diesel engine,” *SAE International Journal of Engines*, vol. 6, no. 2, pp. 788–796, 2013.

[21] R. Dehner, A. Selamet, M. Steiger, H. Sun, D. Hanna, and L. Hu, “Acoustic measurements from an automotive centrifugal compressor with a switchable dual-port casing treatment for extended operating range,” in *ASME Turbo Expo 2016: Turbomachinery Technical Conference and Exposition*. American Society of Mechanical Engineers, 2016, pp. V008T23A012–V008T23A012.

[22] D. Evans and A. Ward, “Minimising turbocharger whoosh noise for diesel powertrains,” SAE Technical Paper, Tech. Rep., 2005.

[23] C. Teng and S. Homco, “Investigation of compressor whoosh noise in automotive turbochargers,” *SAE International Journal of Passenger Cars-Mechanical Systems*, vol. 2, no. 2009-01-2053, pp. 1345–1351, 2009.

[24] T. Raitor and W. Neise, “Sound generation in centrifugal compressors,” *Journal of Sound and Vibration*, vol. 314, no. 3-5, pp. 738–756, 2008.

[25] A. Romagnoli, C. D. Copeland, R. Martinez-Botas, M. Seiler, S. Rajoo, and A. Costall, “Comparison between the steady performance of double-entry and twin-entry turbocharger turbines,” *Journal of Turbomachinery*, vol. 135, no. 1, p. 011042, 2013.

[26] T. Palenschat, M. Mueller, S. Rajoo, M. S. Chiong, P. Newton, R. Martinez-Botas, and F. X. Tan, “Steady-state experimental and meanline study of an asymmetric twin-scroll turbine at full and unequal and partial admission conditions,” SAE Technical Paper, Tech. Rep., 2018.

[27] D. Zhu and X. Zheng, “Potential for energy and emissions of asymmetric twin-scroll turbocharged diesel engines combining inverse brayton cycle system,” *Energy*, vol. 179, pp. 581–592, 2019.

[28] S. CD-adapco, “Star ccm+ user guide version 12.04,” *CD-Adapco: New York, NY, USA*, 2017.

[29] S. W. Rienstra and A. Hirschberg, “An introduction to acoustics,” *Eindhoven University of Technology*, vol. 18, p. 19, 2003.

[30] D. G. Crighton, A. P. Dowling, J. Ffowcs-Williams, M. Heckl, F. Leppington, and J. F. Bartram, “Modern methods in analytical acoustics lecture notes,” 1992.

[31] M. Åbom, *An introduction to flow acoustics*. Skolan för teknikvetenskap, Kungliga Tekniska högskolan, 2006.

[32] M. Carley, “Turbulence and noise,” *Chapter 3: Characterizing turbulence*, 2011.

[33] N. Curle, “The influence of solid boundaries upon aerodynamic sound,” *Proceedings of the Royal Society of London. Series A. Mathematical and Physical Sciences*, vol. 231, no. 1187, pp. 505–514, 1955.

[34] M. E. Goldstein, “Aeroacoustics,” *New York, McGraw-Hill International Book Co., 1976. 305 p.*, 1976.

[35] I. Proudman, “The generation of noise by isotropic turbulence,” *Proceedings of the Royal Society of London. Series A. Mathematical and Physical Sciences*, vol. 214, no. 1116, pp. 119–132, 1952.

[36] J. E. Ffowcs Williams and D. L. Hawkings, “Sound generation by turbulence and surfaces in arbitrary motion,” *Philosophical Transactions of the Royal Society of London. Series A, Mathematical and Physical Sciences*, vol. 264, no. 1151, pp. 321–342, 1969.

[37] H. Rämmal and M. Åbom, “Acoustics of turbochargers,” SAE Technical Paper, Tech. Rep., 2007.

[38] A. McAlpine and M. Fisher, “On the prediction of “buzz-saw” noise in aero-engine inlet ducts,” *Journal of Sound and Vibration*, vol. 248, no. 1, pp. 123–149, 2001.

[39] F. Inc., “User’s guide for fluent 6.1,” 2006.

[40] F. R. Menter, “Best practice: scale-resolving simulations in ansys cfd,” *ANSYS Germany GmbH*, vol. 1, 2012.

[41] H. K. Versteeg and W. Malalasekera, *An introduction to computational fluid dynamics: the finite volume method*. Pearson education, 2007.

[42] F. Menter and M. Kuntz, "Adaptation of eddy-viscosity turbulence models to unsteady separated flow behind vehicles," in *The aerodynamics of heavy vehicles: trucks, buses, and trains*. Springer, 2004, pp. 339–352.

[43] A. Travin, M. Shur, M. Strelets, P. Spalart, R. Friederich, and W. Rodi, "Advances in les of complex flows," 2002.

[44] M. L. Shur, P. R. Spalart, M. K. Strelets, and A. K. Travin, "A hybrid rans-les approach with delayed-des and wall-modelled les capabilities," *International Journal of Heat and Fluid Flow*, vol. 29, no. 6, pp. 1638–1649, 2008.

[45] F. Wiesner, "A review of slip factors for centrifugal impellers," 1967.

[46] R. H. Aungier, "Mean streamline aerodynamic performance analysis of centrifugal compressors," 1995.

[47] X. Qiu, D. Japikse, J. Zhao, and M. R. Anderson, "Analysis and validation of a unified slip factor model for impellers at design and off-design conditions," 2011.

[48] M. R. Galvas, *Fortran program for predicting off-design performance of centrifugal compressors*. National Aeronautics and Space Administration Washington, DC, USA, 1973, vol. 7487.

[49] O. Conrad, K. Raif, and M. Wessels, "The calculation of performance maps for centrifugal compressors with vane-island diffusers," *Performance prediction of centrifugal pumps and compressors*, pp. 135–147, 1979.

[50] J. Coppage and F. Dallenbach, "Study of supersonic radial compressors for refrigeration and pressurization systems," Garrett Corp Los Angeles Ca AiResearch MFG DIV, Tech. Rep., 1956.

[51] W. Jansen, "A method for calculating the flow in a centrifugal impeller when entropy gradient are present," *Inst. Mech. Eng. Internal Aerodynamics*, 1970.

[52] S. E. Haaland, "Simple and explicit formulas for the friction factor in turbulent pipe flow," 1983.

[53] J. Johnston and R. Dean Jr, "Losses in vaneless diffusers of centrifugal compressors and pumps: analysis, experiment, and design," 1966.

[54] H. Oh, E. Yoon, and M. Chung, "Systematic two-zone modelling for performance prediction of centrifugal compressors," *Proceedings of the Institution of Mechanical Engineers, Part A: Journal of Power and Energy*, vol. 216, no. 1, pp. 75–87, 2002.

[55] D. Japikse, "Assessment of single-and two-zone modeling of centrifugal compressors, studies in component performance: Part 3," in *Turbo Expo: Power for Land, Sea, and Air*, vol. 79382. American Society of Mechanical Engineers, 1985, p. V001T03A023.

[56] J. W. Daily and R. E. Nece, "Chamber dimension effects on induced flow and frictional resistance of enclosed rotating disks," 1960.

[57] J. D. Stanitz, "One-dimensional compressible flow in vaneless diffusers of radial-and mixed-flow centrifugal compressors, including effects of friction, heat transfer and area change," 1952.

[58] C. Weber and M. Koronowski, "Meanline performance prediction of volutes in centrifugal compressors," in *Turbo Expo: Power for Land, Sea, and Air*, vol. 79283. American Society of Mechanical Engineers, 1986, p. V001T01A091.

[59] G. Farin, *Curves and surfaces for computer-aided geometric design: a practical guide*. Elsevier, 2014.

[60] V. Rovenski, *Modeling of Curves and Surfaces with MATLAB*. Springer, 2010.

[61] R. Halır and J. Flusser, "Numerically stable direct least squares fitting of ellipses," in *Proc. 6th International Conference in Central Europe on Computer Graphics and Visualization. WSCG*, vol. 98. Citeseer, 1998, pp. 125–132.

[62] P. L. Miller IV, J. H. Oliver, D. P. Miller, and D. L. Tweedt, *BladeCAD: An interactive geometric design tool for turbomachinery blades*. American Society of Mechanical Engineers, 1996, vol. 78729.

[63] M. M. Messele and A. Engeda, "Numerical aerodynamics and acoustics performance study of turbocharger compressor equipped with active casing treatment," in *AIAA Scitech 2020 Forum*, 2020, p. 1250.

[64] J.-P. Jensen, A. Kristensen, S. C. Sorenson, N. Houbak, and E. Hendricks, "Mean value modeling of a small turbocharged diesel engine," SAE Technical Paper, Tech. Rep., 1991.

[65] J. E. Hadef, G. Colin, Y. Chamaillard, and V. Talon, "Physical-based algorithms for interpolation and extrapolation of turbocharger data maps," *SAE International Journal of Engines*, vol. 5, no. 2, pp. 363–378, 2012.

[66] F. K. Moore and E. M. Greitzer, "A theory of post-stall transients in axial compression systems: Part i—development of equations," *Journal of engineering for gas turbines and power*, vol. 108, no. 1, pp. 68–76, 1986.

[67] G. Theotokatos and N. Kyrtatos, "Diesel engine transient operation with turbocharger compressor surging," SAE Technical Paper, Tech. Rep., 2001.

[68] H. Chen and V.-M. Lei, "Casing treatment and inlet swirl of centrifugal compressors," *Journal of Turbomachinery*, vol. 135, no. 4, 2013.

[69] R. Hunziker, H.-P. Dickmann, and R. Emmrich, "Numerical and experimental investigation of a centrifugal compressor with an inducer casing bleed system," *Proceedings of the Institution of Mechanical Engineers, Part A: Journal of Power and Energy*, vol. 215, no. 6, pp. 783–791, 2001.

[70] R. Tanna, J. Yin, B. Sirakov, and V. Barbarie, “Development of ported shroud compressor housing with reduced compressor blade pass source acoustic level,” in *IMechE Ninth International Conference on Turbochargers and Turbocharging, London, May*, 2010, pp. 19–20.

[71] F. Mendonça, O. Baris, and G. Capon, “Simulation of radial compressor aeroacoustics using cfd,” in *ASME Turbo Expo 2012: Turbine Technical Conference and Exposition*. American Society of Mechanical Engineers, 2012, pp. 1823–1832.

[72] R. Navarro, “A numerical approach for predicting flow-induced acoustics at near-stall conditions in an automotive turbocharger compressor,” Ph.D. dissertation, PhD thesis, Universitat Politecnica de Valencia, 2014.

[73] A. Broatch, J. Galindo, R. Navarro, and J. García-Tíscar, “Methodology for experimental validation of a cfd model for predicting noise generation in centrifugal compressors,” *International Journal of Heat and Fluid Flow*, vol. 50, pp. 134–144, 2014.

[74] R. Allen, F. Mendonça, and D. Kirkham, “Rans and des turbulence model predictions of noise on the m219 cavity at m= 0.85,” *International Journal of Aeroacoustics*, vol. 4, no. 1-2, pp. 135–151, 2005.

[75] C. Mockett, *A Comprehensive Study of Detached Eddy Simulation*. Univerlagtuberlin, 2009.

[76] C. Wagner, T. Hüttl, and P. Sagaut, *Large-eddy simulation for acoustics*. Cambridge University Press, 2007, vol. 20.

[77] F. Mendonca, A. Read, F. Imada, and V. Girardi, “Efficient cfd simulation process for aeroacoustic driven design,” SAE Technical Paper, Tech. Rep., 2010.

[78] S. Marburg, “Discretization requirements: How many elements per wavelength are necessary?” in *Computational Acoustics of Noise Propagation in Fluids-Finite and Boundary Element Methods*. Springer, 2008, pp. 309–332.

[79] S. Glegg and W. Devenport, *Aeroacoustics of low Mach number flows: fundamentals, analysis, and measurement*. Academic Press, 2017.

[80] Ansys-Fluent, “Ansys fluent 18.2 user’s guide,” *Canonsburg, PA*, 2017.

[81] J. G. Hawley, F. Wallace, A. Cox, R. Horrocks, and G. Bird, “Reduction of steady state nox levels from an automotive diesel engine using optimised vgt/egr schedules,” *SAE transactions*, pp. 1172–1184, 1999.

[82] M. J. Van Nieuwstadt, I. V. Kolmanovsky, and P. E. Moraal, “Coordinated egr-vgt control for diesel engines: an experimental comparison,” *SAE transactions*, pp. 238–249, 2000.

[83] M. Zheng, G. T. Reader, and J. G. Hawley, “Diesel engine exhaust gas recirculation—-a review on advanced and novel concepts,” *Energy conversion and management*, vol. 45, no. 6, pp. 883–900, 2004.

[84] D. Lückmann, T. Uhlmann, H. Kindl, and S. Pischinger, “Separation in double entry turbine housings at boosted gasoline engines,” *MTZ worldwide*, vol. 74, no. 10, pp. 4–9, 2013.

[85] D. Lückmann, M. Stadermann, R. Aymanns, and S. Pischinger, “Investigation of cross flow in double entry turbocharger turbines,” in *Turbo Expo: Power for Land, Sea, and Air*, vol. 49866. American Society of Mechanical Engineers, 2016, p. V008T23A024.

[86] C. D. Copeland, P. J. Newton, R. Martinez-Botas, and M. Seiler, “The effect of unequal admission on the performance and loss generation in a double-entry turbocharger turbine,” *Journal of Turbomachinery*, vol. 134, no. 2, 2012.

[87] C. D. Copeland, R. Martinez-Botas, and M. Seiler, “Unsteady performance of a double entry turbocharger turbine with a comparison to steady flow conditions,” *Journal of turbomachinery*, vol. 134, no. 2, 2012.

[88] P. Newton, C. Copeland, R. Martinez-Botas, and M. Seiler, “An audit of aerodynamic loss in a double entry turbine under full and partial admission,” *International Journal of Heat and Fluid Flow*, vol. 33, no. 1, pp. 70–80, 2012.

[89] P. Newton, R. Martinez-Botas, and M. Seiler, “A three-dimensional computational study of pulsating flow inside a double entry turbine,” *Journal of Turbomachinery*, vol. 137, no. 3, 2015.

[90] T. Palenschat, P. Newton, R. F. Martinez-Botas, M. Müller, and J. Leweux, “3-d computational loss analysis of an asymmetric volute twin-scroll turbocharger,” in *ASME Turbo Expo 2017: Turbomachinery Technical Conference and Exposition*. American Society of Mechanical Engineers Digital Collection, 2017.

[91] C. Iandoli and E. Sciubba, “3-d numerical calculation of the local entropy generation rates in a radial compressor stage,” *International journal of thermodynamics*, vol. 8, no. 2, pp. 83–94, 2005.

[92] P. Siemens, “Simcenter star-ccm+ user guide v15.04.005,” *Siemens PLM*, 2020.

[93] C. Arcoumanis, *Internal combustion engines*. Elsevier, 2012.

[94] J. D. Denton, *Loss mechanisms in turbomachines*. American Society of Mechanical Engineers, 1993, vol. 78897.

[95] E. M. Greitzer, C. S. Tan, and M. B. Graf, *Internal flow: concepts and applications*. Cambridge University Press, 2007, vol. 3.

[96] C. K. Batchelor and G. Batchelor, *An introduction to fluid dynamics*. Cambridge university press, 2000.

[97] J. Moore and J. G. Moore, “Entropy production rates from viscous flow calculations: Part i—a turbulent boundary layer flow,” in *Turbo Expo: Power for Land, Sea, and Air*, vol. 79511. American Society of Mechanical Engineers, 1983, p. V001T01A032.

[98] A. A. Sonin, “Equation of motion for viscous fluids,” 2001.

[99] F. Kock and H. Herwig, “Local entropy production in turbulent shear flows: a high-reynolds number model with wall functions,” *International journal of heat and mass transfer*, vol. 47, no. 10-11, pp. 2205–2215, 2004.

[100] F. U. Guide, “Fluent 6.3. 26,” 2005.

[101] C. Srinivasan and D. V. Papavassiliou, “Prediction of the turbulent prandtl number in wall flows with lagrangian simulations,” *Industrial & engineering chemistry research*, vol. 50, no. 15, pp. 8881–8891, 2011.

[102] W. M. Kays, “Turbulent prandtl number. where are we?” *ATJHT*, vol. 116, no. 2, pp. 284–295, 1994.

[103] ——, *Convective heat and mass transfer*. Tata McGraw-Hill Education, 2011.

[104] M. Abel, R. F. Martinez-Botas, M. Wöhr, M. Müller, and J. Leweux, “3d computational loss analysis of a compressor for heavy duty truck engine turbochargers,” in *ASME Turbo Expo 2019: Turbomachinery Technical Conference and Exposition*. American Society of Mechanical Engineers Digital Collection, 2019.

[105] J. Bindon, “The measurement and formation of tip clearance loss,” 1989.

[106] F. Bhinder, “Paper 21: investigation of flow in the nozzle-less spiral casing of a radial inward-flow gas turbine,” in *Proceedings of the Institution of Mechanical Engineers, Conference Proceedings*, vol. 184, no. 7. SAGE Publications Sage UK: London, England, 1969, pp. 66–71.

[107] W. Tabakoff, B. Vittal, and B. Wood, “Three-dimensional flow measurements in a turbine scroll,” 1984.

[108] M. Malak, A. Hamed, and W. Tabakoff, “Three-dimensional flow field measurements in a radial inflow turbine scroll using ldv,” 1986.

[109] S. MacGregor, A. Whitfield, and A. M. Noor, “Design and performance of vaneless volutes for radial inflow turbines: part 3: experimental investigation of the internal flow structure,” *Proceedings of the Institution of Mechanical Engineers, Part A: Journal of Power and Energy*, vol. 208, no. 4, pp. 295–302, 1994.

[110] S. P. Lee, M. Jupp, and A. Nickson, “The influence of secondary flow structures in a turbocharger turbine housing in steady state and pulsating flow conditions,” in *2016 7th international conference on mechanical and aerospace engineering (ICMAE)*. IEEE, 2016, pp. 154–159.

[111] M. Yang, R. Martinez-Botas, S. Rajoo, T. Yokoyama, and S. Ibaraki, “An investigation of volute cross-sectional shape on turbocharger turbine under pulsating conditions in internal combustion engine,” *Energy Conversion and Management*, vol. 105, pp. 167–177, 2015.

[112] A. Simpson, S. Spence, and J. Watterson, “A comparison of the flow structures and losses within vaned and vaneless stators for radial turbines,” *Journal of turbomachinery*, vol. 131, no. 3, 2009.

[113] J. F. Suhrmann, D. Peitsch, M. Gugau, and T. Heuer, “On the effect of volute tongue design on radial turbine performance,” in *Turbo Expo: Power for Land, Sea, and Air*, vol. 44748. American Society of Mechanical Engineers, 2012, pp. 891–901.

[114] S. P. Lee, S. M. Barrans, M. L. Jupp, and A. K. Nickson, “The impact of volute aspect ratio on the performance of a mixed flow turbine,” *Aerospace*, vol. 4, no. 4, p. 56, 2017.

[115] S. P. Lee, M. L. Jupp, A. K. Nickson, and J. M. Allport, “Analysis of a tilted turbine housing volute design under pulsating inlet conditions,” in *Turbo Expo: Power for Land, Sea, and Air*, vol. 50800. American Society of Mechanical Engineers, 2017, p. V02CT44A016.

[116] M. A. Meghnine, M. K. Hamidou, and M. Hamel, “Influence of the volute cross-sectional shape on mixed inflow turbine performances,” *Advances in Mechanical Engineering*, vol. 9, no. 7, p. 1687814017708174, 2017.

[117] C. Pfleiderer, *Strömungsmaschinen*. Springer-Verlag, 2013.

[118] A. J. Stepanoff, “Centrifugal and axial flow pumps,” J. Wiley, Tech. Rep., 1948.

[119] A. H. Church, *Centrifugal pumps and blowers*. JOUN WILEY & SONS, INC. NEW YORK LONDON, 1972.

[120] W. C. Osborne, “Fans,” 1966.

[121] R. K. Turton, *Principles of turbomachinery*. Springer Science & Business Media, 2012.

[122] A. Whitfield and A. M. Noor, “Design and performance of vaneless volutes for radial inflow turbines: Part 1: Non-dimensional conceptual design considerations,” *Proceedings of the Institution of Mechanical Engineers, Part A: Journal of Power and Energy*, vol. 208, no. 3, pp. 199–211, 1994.

[123] R. H. Aungier, “Turbine aerodynamics,” *American Society of Mechanical Engineers Press, New York*, 2006.

[124] M. Messele and A. Engeda, “Status review for the prediction methods of the radial force caused by a centrifugal pump or volute during off-design-point operation,” in *Fluids Engineering Division Summer Meeting*, vol. 51579. American Society of Mechanical Engineers, 2018, p. V003T12A003.

[125] J. W. Pereira, *Grid generation of volutes using Visual BASIC*. Michigan State University, 1998.

[126] J. Galindo, S. Hoyas, P. Fajardo, and R. Navarro, “Set-up analysis and optimization of cfd simulations for radial turbines,” *Engineering Applications of Computational Fluid Mechanics*, vol. 7, no. 4, pp. 441–460, 2013.

[127] M. Hussain and F. Bhinder, “Experimental study of the performance of a nozzle-less volute casing for turbocharger turbines,” SAE Technical Paper, Tech. Rep., 1984.

[128] J. Sokhey, W. Tabakoff, and W. Hosny, “Flow behavior in inlet guide vanes of radial turbines,” 1975.

[129] A. Romagnoli and R. Martinez-Botas, “Performance prediction of a nozzled and nozzleless mixed-flow turbine in steady conditions,” *International Journal of Mechanical Sciences*, vol. 53, no. 8, pp. 557–574, 2011.

[130] D. Eberly, “The area of intersecting ellipses,” 2010.

[131] P. Bourke, “Calculating the area and centroid of a polygon,” *Swinburne Univ. of Technology*, vol. 7, 1988.